

AD-A125 873

RESEARCH TO DEVELOP AND EVALUATE ADVANCED EDDY CURRENT
SENSORS FOR DETECT. (U) BATTELLE PACIFIC NORTHWEST LABS
RICHLAND WASH J N PRINCE ET AL DEC 82

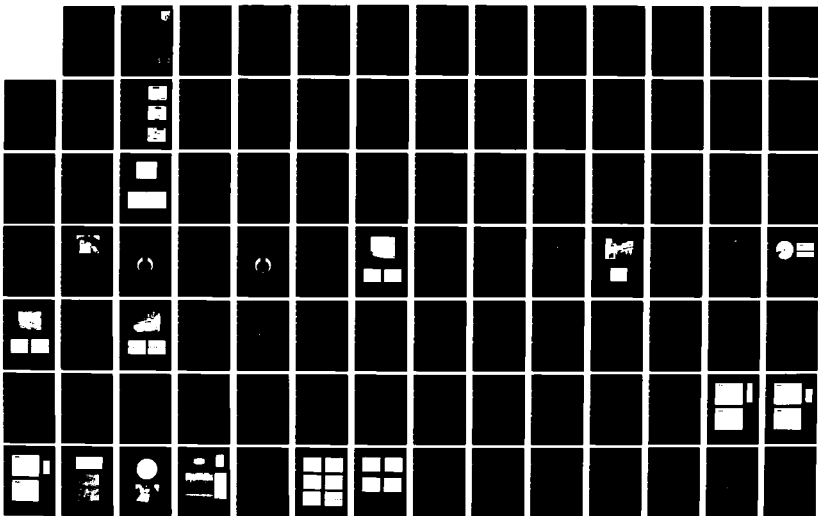
1/2

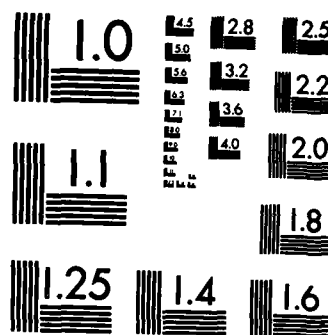
UNCLASSIFIED

AFMRL-TR-82-4155 F33615-80-C-5172

F/G 21/5

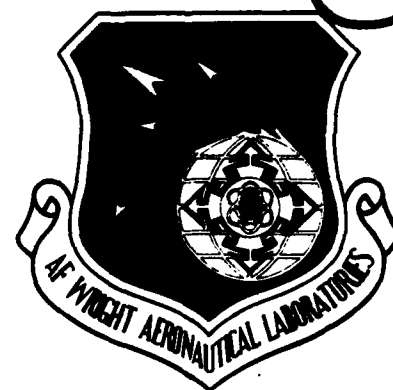
NL





AD A 125873

AFWAL-TR-82-4155



Research to Develop and Evaluate Advanced Eddy Current Sensors for Detecting Small Flaws in Metallic Aerospace Components

Battelle, Pacific Northwest Laboratories
P.O. Box 999
Richland, Washington 99352

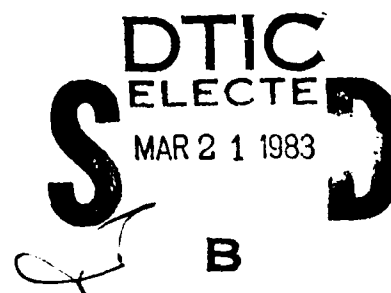
December 1982

Final Report for Period September 1980 - July 1982

APPROVED FOR PUBLIC RELEASE; DISTRIBUTION UNLIMITED

DTIC FILE COPY

Materials Laboratory
Air Force Wright Aeronautical Laboratories
Air Force Systems Command
Wright-Patterson Air Force Base, Ohio 45433



88 03 21 062

NOTICE

When Government drawings, specifications, or other data are used for any purpose other than in connection with a definitely related Government procurement operation, the United States Government thereby incurs no responsibility nor any obligation whatsoever; and the fact that the government may have formulated, furnished, or in any way supplied the said drawings, specifications, or other data, is not to be regarded by implication or otherwise as in any manner licensing the holder or any other person or corporation, or conveying any rights or permission to manufacture, use, or sell any patented invention that may in any way be related thereto.

This report has been reviewed by the Office of Public Affairs (ASD/PA) and is releasable to the National Technical Information Service (NTIS). At NTIS, it will be available to the general public, including foreign nations.

This technical report has been reviewed and is approved for publication.



DALE E. CHIMENTI
Nondestructive Evaluation Branch
Metals and Ceramics Division

FOR THE COMMANDER



DONALD M. FORNEY, JR., Chief
Nondestructive Evaluation Branch
Metals and Ceramics Division

"If your address has changed, if you wish to be removed from our mailing list, or if the addressee is no longer employed by your organization please notify AFWAL/MLLP, W-PAFB, OH 45433 to help us maintain a current mailing list".

Copies of this report should not be returned unless return is required by security considerations, contractual obligations, or notice on a specific document.

Unclassified

SECURITY CLASSIFICATION OF THIS PAGE (When Data Entered)

REPORT DOCUMENTATION PAGE		READ INSTRUCTIONS BEFORE COMPLETING FORM
1. REPORT NUMBER AFWAL-TR-82-4155	2. GOVT ACCESSION NO. AD-A125 873	3. RECIPIENT'S CATALOG NUMBER
4. TITLE (and Subtitle) RESEARCH TO DEVELOP AND EVALUATE ADVANCED EDDY CURRENT SENSORS FOR DETECTING SMALL FLAWS IN METALLIC AEROSPACE COMPONENTS		5. TYPE OF REPORT & PERIOD COVERED Final Technical Report 9/20/80 - 7/31/82
7. AUTHOR(s) James M. Prince and Bert A. Auld		6. PERFORMING ORG. REPORT NUMBER
9. PERFORMING ORGANIZATION NAME AND ADDRESS Battelle, Pacific Northwest Laboratories P.O. Box 999 Richland, WA 99352		8. CONTRACT OR GRANT NUMBER(s) F33615-80-C-5172
11. CONTROLLING OFFICE NAME AND ADDRESS Materials Laboratory (AFWAL/MLLP) Air Force Wright Aeronautical Laboratories (AFSC) Wright-Patterson AFB, OH 45433		10. PROGRAM ELEMENT, PROJECT, TASK AREA & WORK UNIT NUMBERS 2418/05 62102
14. MONITORING AGENCY NAME & ADDRESS (if different from Controlling Office)		12. REPORT DATE December 1982
		13. NUMBER OF PAGES 96
		15. SECURITY CLASS. (of this report) UNCLASSIFIED
		15a. DECLASSIFICATION/DOWNGRADING SCHEDULE
16. DISTRIBUTION STATEMENT (of this Report) Approved for public release; distribution unlimited.		
17. DISTRIBUTION STATEMENT (of the abstract entered in Block 20, if different from Report)		
18. SUPPLEMENTARY NOTES		
19. KEY WORDS (Continue on reverse side if necessary and identify by block number) Nondestructive Testing Eddy Current Testing Microwave Eddy Current Probes Ferromagnetic Resonance Probes		
20. ABSTRACT (Continue on reverse side if necessary and identify by block number) - The purpose of this program was to develop a reproducible, highly sensitive novel eddy current probe applying the technique of ferromagnetic resonance (FMR). The method developed must be suited to inspect test objects where access may be limited, for example bolt holes of turbine engine disks. This program studied the FMR probe in both its passive and active modes. An active probe was developed and tested that demonstrated that the FMR technique is a practical approach for inspection of metallic aerospace components.		

DD FORM 1 JAN 73 1473

EDITION OF 1 NOV 65 IS OBSOLETE
S/N 0102-LF-014-6601

UNCLASSIFIED

SECURITY CLASSIFICATION OF THIS PAGE (When Data Entered)

UNCLASSIFIED

SECURITY CLASSIFICATION OF THIS PAGE (When Data Entered)

Abstract (cont'd)

The program consisted of three tasks. In Task I the theoretical analysis and modelling was performed by Stanford University under subcontract with Battelle. This analysis and modelling served as a guide in probe design concepts for Battelle's experimental evaluation, which was performed in Task II. Finally, a demonstration, comprising Task III, was performed for Air Force Materials Laboratory personnel at Battelle's facility in which five FMR probes of the same design were tested. The results of the demonstration confirmed the FMR probe design's reproducibility and repeatable high sensitivity for detecting flaws located in a titanium bolt-hole specimen.

UNCLASSIFIED

SECURITY CLASSIFICATION OF THIS PAGE (When Data Entered)

FOREWORD

This final technical report covers work performed under Contract F33615-80-C-5172 from 2 September 1980 to 31 July 1982. The work was administered under the technical direction of Mr. Dale Chimenti, Materials Laboratory, Air Force Wright Aeronautical Laboratories, Wright-Patterson Air Force Base, Ohio 45433.

The contractor was the Nondestructive Testing Section of Battelle Pacific Northwest Laboratories, Richland, Washington 99352. The principal investigator was Mr. James Prince. Other investigators were T. J. Davis and P. L. Tomeraasen. The theoretical analysis was performed at Stanford by Prof. B. A. Auld and his associates Mr. Majid Riaziat and Mr. Frank Muennemann.



Accession For	
NTIS GRA&I	<input checked="checked" type="checkbox"/>
DTIC TAB	<input type="checkbox"/>
Unannounced	<input type="checkbox"/>
Justification	
By	
Distribution/	
Availability Codes	
Dist	Avail and/or Special
A	

TABLE OF CONTENTS

	<u>Page</u>
1.0 INTRODUCTION	1
2.0 THEORETICAL ANALYSIS	3
2.1 Introduction to the FMR Probe	3
2.2 Spatial Frequency Analysis of First and Second Order Liftoff Signals	9
2.3 Flaw Interactions	13
2.4 Oscillator Probes	15
3.0 EXPERIMENTAL EVALUATION	17
3.1 Introduction	17
3.2 Passive Probe Evaluation	19
3.2.1 Reflection Coefficient Signal Processor	19
3.2.2 Two-Frequency Microwave Experiments	22
3.2.3 Liftoff Suppression Using 200 kHz Liftoff Detection	25
3.3 Active Probe Evaluation	30
3.3.1 Active Probe Signal Processor	30
3.3.2 Mechanical Test Apparatus	30
3.3.3 Probe Permanent Magnet/Pole Piece Configuration	33
3.3.4 2 GHz Active Probe Test	36
3.3.5 900 MHz Active Probe Development and Test	36
3.3.6 Demonstration Probe	44
3.3.7 Dual-Differential Probe	46
3.3.8 Q and F Data from Active Probe	48
4.0 SUMMARY AND CONCLUSIONS	51
4.1 Theoretical	51
4.2 Experimental	53
REFERENCES	56
Appendix A - First and Second Order Liftoff Effects	58
Appendix B - Liftoff Calculations for the FMR Probe	61
Appendix C - The Effect of a Conducting Plane on the Uniform Precession Mode of a Spherical Resonator	66
Appendix D - Magnified EDM Notches and Tight Cracks	70
Appendix E - Demonstration Probe Data	77
Appendix F - Electronic Schematics of Processors Used in the Experimental Evaluation	80
Appendix G - Demonstration Probe Fabrication	84

LIST OF FIGURES

	<u>Page</u>
1. Microwave Ferromagnetic Resonance Probe for Eddy Current Flaw Detection	4
2. Details of Two-Sphere Probe Geometries	6
3. Data Taken with Two-Sphere Probe in Multimode Operation	7
4. Formulation of Liftoff in Terms of a Surface Impedance Change	11
5. Microwave Reflection Coefficient Signal Processor	20
6. Typical Reflection Coefficient Plot	21
7. Reflected Voltage Versus Drive Frequency Plots	21
8. Microwave Narrow Band Two-Frequency Test Configuration	23
9. Microwave Wide Band Two-Frequency Test Configuration	24
10. Passive Probe in Two-Coil Liftoff Suppression Configuration	26
11. Liftoff Suppression Obtained with Two-Coil Method	27
12. Two-Coil Probe Arrangement	28
13. Liftoff Suppression Obtained with Shared Coil Method	29
14. Conceptual Design of Passive Bolt Hole Probe	31
15. Active Probe Signal Processor	32
16. Mechanical Test Apparatus	34
17. Titanium Test Piece and Notch Dimensions	34
18. Permanent Magnet (PM)/Pole Piece Arrangement for Bolt Hole Probe	35
19. 2 GHz Active Probe with Data Taken on Titanium Test Piece	37
20. Variable Strength dc Magnetic Field Source	39
21. Initial 900 MHz Active Probe Circuit Diagram	40
22. Initial 900 MHz Active Probe with Data Taken on Titanium Test Piece	41

LIST OF FIGURES

(cont'd)

	<u>Page</u>
23. Initial 900 MHz Active Probe Liftoff Characteristics	42
24. Improved Active Probe Design for Easier Laboratory Evaluation	43
25. Initial Bolt Hole Probe with Bolt Hole Specimen (USAF 1) and Data	44
26. Demonstration Probe with Typical Titanium Disk and Bolt Hole Responses	45
27. Dual-Differential Probe with Titanium Disk Data	47
28. Active Probe with AGC	49
B-1 The rf Field is Perpendicular to the Plane of the Excitation Coil	65
C-1 Formulation of Liftoff in Terms of a Surface Impedance Change	67
D-1 EDM Notches in Titanium Disk (100X)	71
D-2 Tight Fatigue Crack in Aluminum (250X)	74
D-3 Titanium Bolt Hole Specimen (USAF 1)	75
E-1 Demonstration Probe Data on Titanium Disk and Bolt Hole Specimens	78
F-1 Microwave Reflection Coefficient Signal Processor Schematic	81
F-2 Two-Coil Liftoff Compensation Schematic	82
F-3 Microwave Active Probe Signal Processor Schematic	83
G-1 Demonstration Probe Circuit	85
G-2 Demonstration Probe Load Reflection Coefficient	87
G-3 Demonstration Probe Layout	88
G-4 YIG Sphere Orientation Arrangement	90

1.0 INTRODUCTION

This report describes the work performed by Battelle-Northwest and Stanford University, under contract F33615-80-C-5172 with Air Force Wright Aeronautical Laboratories. A reproducible, highly sensitive microwave eddy-current probe was developed to provide the Air Force an advanced nondestructive evaluation (NDE) technique for use in their Retirement-for-Cause (RFC) program. The USAF RFC maintenance philosophy has as its goal the life extension of gas turbine engine components beyond their predetermined "safe life" limit. An NDE technique capable of providing high reliability detection of surface cracks approximately 0.25 mm (0.010 inch) in length in regions where access is limited, such as a bolt hole, would allow the turbine engine components to be screened and returned to service. Conventional surface flaw detection techniques in current practice lack both the sensitivity and detection reliability to provide this screening.

The techniques studied in this research are based on the microwave* ferromagnetic resonance (FMR) eddy current probe that had been under development by Prof. B. A. Auld and his associates at Stanford University for several years prior to this study. Prof. Auld's previous work had demonstrated this technique's ability to detect extremely small surface cracks, as well as the probe's simplicity and small size, which would allow access to restricted geometries. Therefore, with basic feasibility established, the objective of this project was to advance and implement the FMR probe in a way that would provide not only a high degree of sensitivity to extremely small surface cracks, but discrimination against spurious signal sources, and a practical and reproducible probe design for possible use in the RFC program.

In order to gain full advantage of Prof. Auld's expertise with FMR probes, a subcontract was established with Stanford under which Prof. Auld and his associates provided the project with theoretical analysis and guidance for the experimental evaluation which was performed at Battelle.

*The term microwave defines a range of frequencies from approximately 750 MHz to 20,000 MHz.

Two techniques for implementing the FMR probe were studied and evaluated. The first technique utilized the FMR probe as a passive device with data collected by observing the reflection coefficient of the probe driven from a 50 ohm microwave system. In the second technique, the probe operated as the resonator in a microwave oscillator, forming an active probe, and yielding data on the frequency of oscillation of the probe circuit. Both techniques required the fabrication of signal processors which were designed to evaluate the theoretical analysis as it applied to optimizing the signal to noise ratio of each technique, where the signal is considered to be caused by flaws and noise by liftoff fluctuations.

Section 2.0 of this report discusses the theoretical analysis performed at Stanford, and Section 3.0 discusses the experimental evaluation performed at Battelle. Section 4.0 summarizes the work performed in this study and provides our conclusions. Additional detailed discussions and data are presented in the Appendices.

2.0 THEORETICAL ANALYSIS

2.1 Introduction to the FMR probe.

When a ferromagnetic crystal is placed in an external dc magnetic field, it exhibits a precessional resonance of its magnetization at a frequency proportional to the strength of the dc magnetic field, $\omega_0 = \gamma H_{dc}$. The proportionality constant γ , depends on the ferromagnetic material. For Yttrium Iron Garnet (YIG) in its pure form $\gamma \approx 2.8$ MHz/Oe. A ferromagnetic resonant probe is made up of a small YIG sphere (diameter on the order of 0.5 mm.) placed in the dc field of a permanent magnet and driven at resonance by a single loop of wire which sets up an rf magnetic field perpendicular to the dc field (Fig.1). The magnetization of the sphere precesses uniformly about the dc field direction and creates an electromagnetic field that interacts with flaws at the surface of a neighboring test sample. Due to the finite size of the YIG resonator, other resonance modes besides the uniform precession mode may be excited according to the geometry of the resonator and the symmetries of the driving field¹. It is more difficult to couple into these higher order modes, and they are more complicated to analyze. In our analysis of the YIG probe, we will treat only the uniform precession mode. It has been verified experimentally^{2,3}, however, that in order to achieve good discrimination between the liftoff and flaw signals, it is sometimes necessary to operate with the proper combination of higher order modes present. This effect is not yet well understood and will require further study to determine its role in optimum probe design. The frequency of operation of the probe can normally range from about 500 to 2000 MHz. Even at 2000 MHz, the electromagnetic wavelength in air is about 15 cm., which is much larger than the probe size and the liftoff distance and, therefore, the field calculations in air may be done in the quasistatic regime. The field distribution outside a single, uniformly magnetized sphere is known to be identical to that of a magnetic dipole of the same strength located at the center of the sphere, suggesting that the YIG sphere in the uniform precession mode may be represented by a rotating magnetic dipole, with a liftoff distance equal to the radius of the sphere. This is the basis of the detailed analysis of the one-sphere probe presented in this report.

As noted above, liftoff discrimination has sometimes been found to improve when the

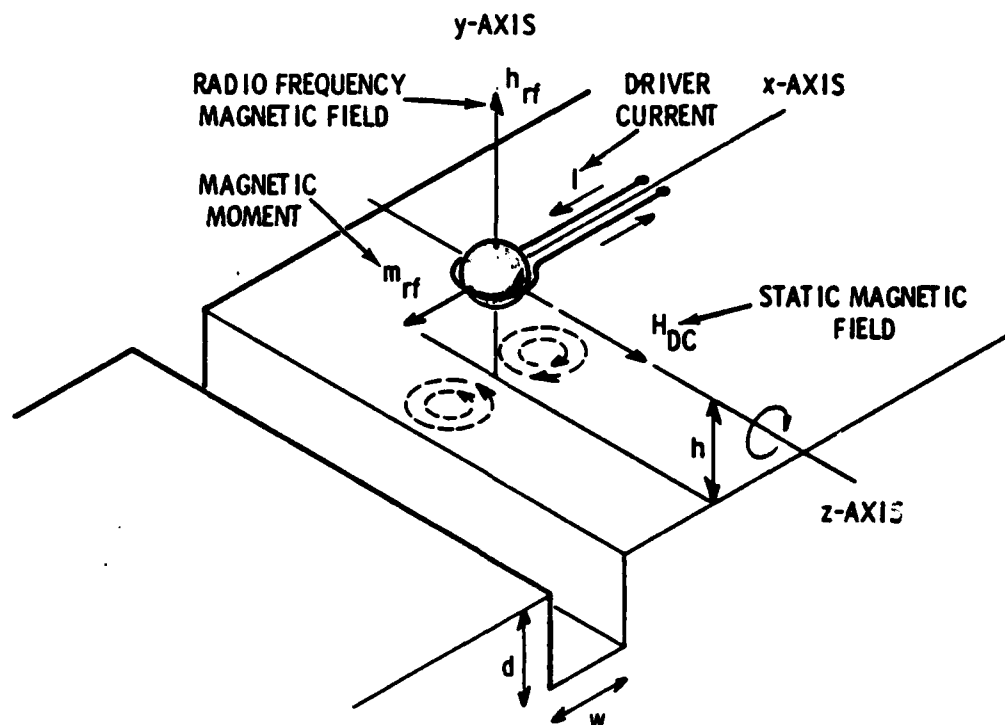


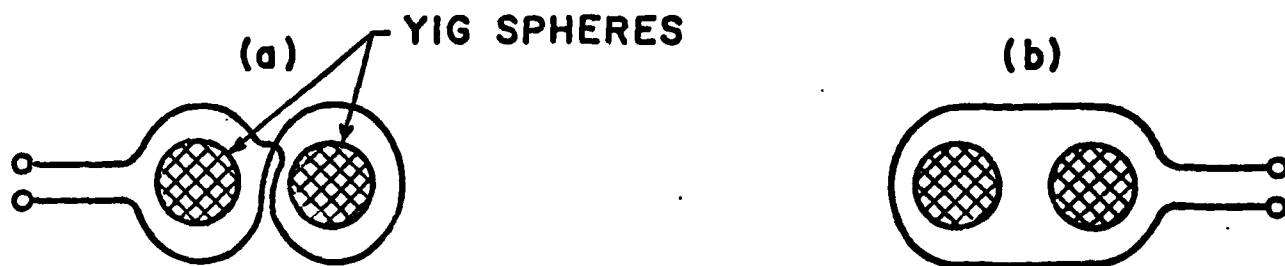
Figure 1. Microwave Ferromagnetic Resonance Probe for Eddy Current Flaw Detection.

probe is excited simultaneously in the uniform precession mode and one of the higher order modes. One of the new concepts introduced in the present program is the use of two-sphere probes. Probes of this type have two uniform precession resonances, one in each sphere (Fig. 2). Two-mode operation of these probes can therefore be achieved by using only the uniform precession mode. This has the following advantages: (1) the uniform precession mode is easier to couple into, and interacts more strongly with a flaw, (2) the two modes (even and odd) of a symmetrically magnetized pair of spheres (Fig. 2) are easier to analyse than the higher order magnetostatic modes and can have a clearcut differential action, and (3) it is easier to visualize and control the effect on the probe response of tilting the magnetic bias field H_{dc} .

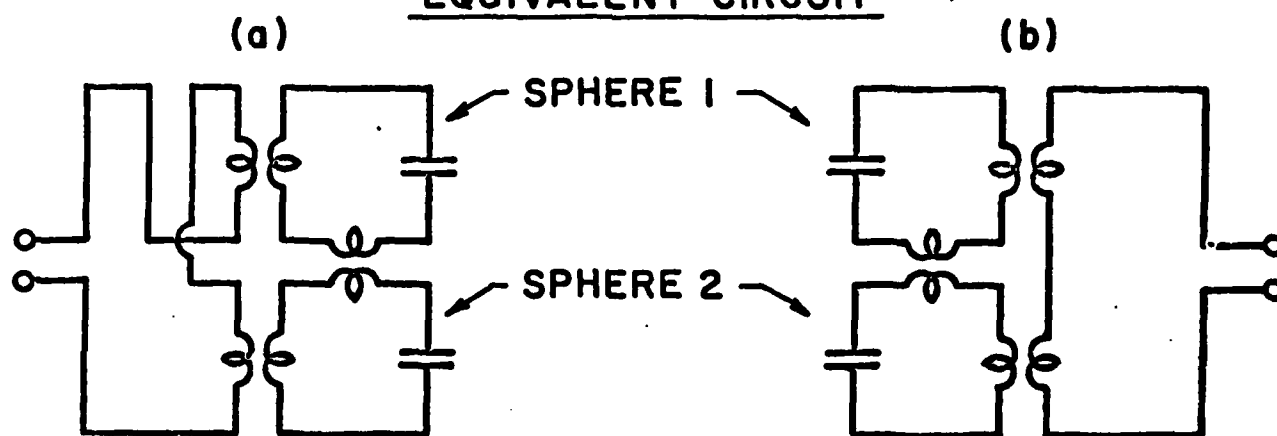
Figure 2 illustrates two possible methods of coupling to the two YIG spheres. In (a) and (b) the two spheres are driven in the odd and even excitations respectively. The rf field produced by the coupling loops is normal to H_{dc} and drives the rf magnetization, denoted by solid arrows at the bottom of the figure, in a clockwise rotational motion about H_{dc} . In the figure the rf magnetization and one half of the resulting magnetic field distribution (dashed lines) are shown at one point in the cycle. To visualize the variation of the rf magnetic field throughout the cycle, one can picture the solid magnetization vectors as rotating individually about H_{dc} , and from that construct the form of the rf magnetic field. It can be seen from the equivalent circuits that the coupling systems illustrated in the figure each couple to only one of the two modes of the two-sphere system. However, as the probe passes over the flaw, the spatial symmetry causing this mode selection is disturbed, and the input terminals become coupled to the two modes. This is the type of behavior exhibited by the single-sphere probes², but in a much more explicit and controllable manner. It is easy to see from the rf magnetic field patterns shown in Fig.2, that each mode will interact very differently with the flaw, this being a multiparameter mechanism that permits discrimination between liftoff and flaw signals.

Figure 2 illustrates the use of a two-sphere probe in multimode operation, where the two spheres are close enough together to couple to each other through their dipole fields and are excited in one of their two modes at a single terminal. Figure 3 shows data taken in this way. Another type of two-sphere probe operation has each of the two spheres individually excited by its own coupling loop, with the spheres sufficiently separated to minimize mutual coupling. Connection of this type of probe in a bridge circuit provides differential operation, as illustrated by experiments performed by Battelle under the present study.

PHYSICAL CONFIGURATION



EQUIVALENT CIRCUIT



NORMAL MODES OF A PAIR OF COUPLED SPHERES

ODD MODE

| Z-AXIS

$\uparrow H_{DC}$



EVEN MODE

| Z-AXIS

$\uparrow H_{DC}$

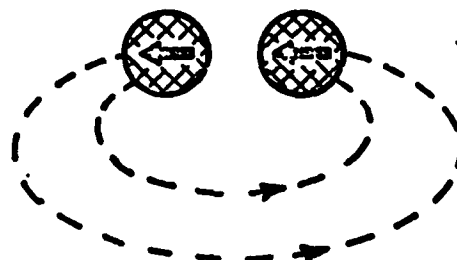


Figure 2. Details of Two-Sphere Probe Geometries.

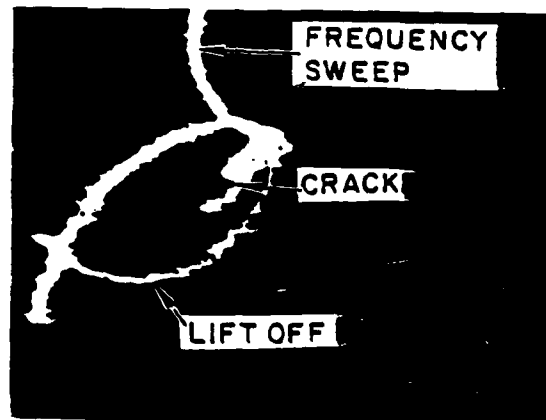
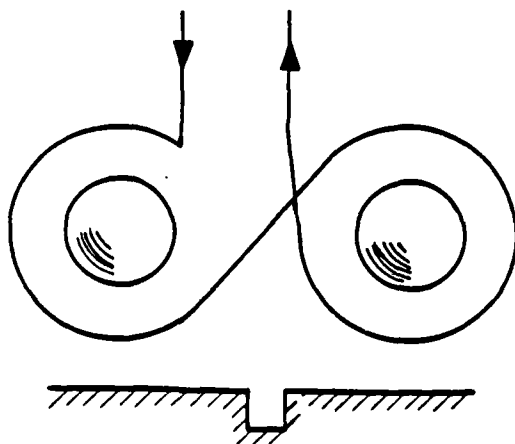
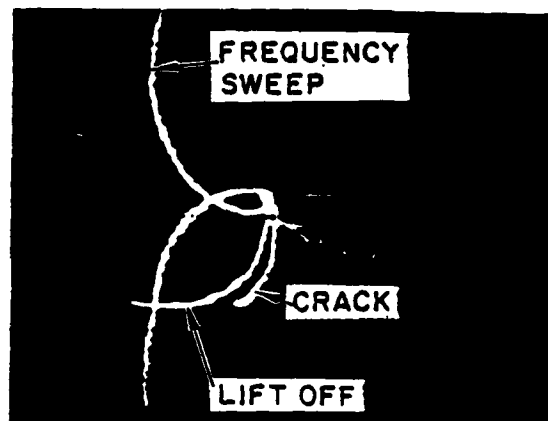
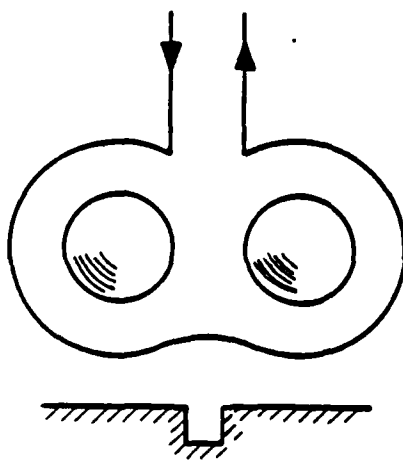
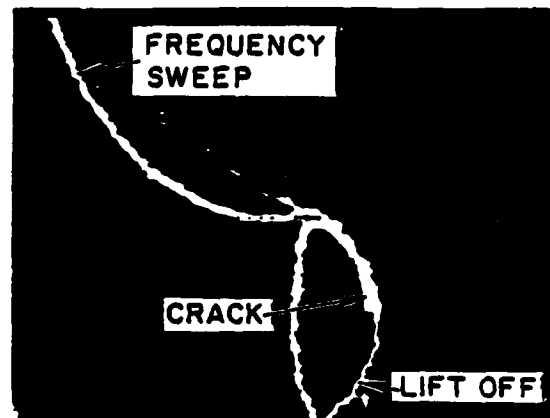
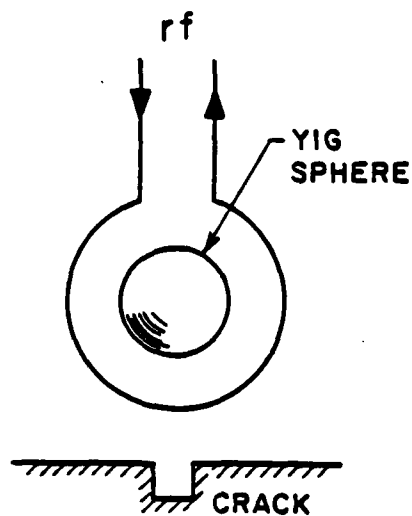


Figure 3. Data Taken with Two-Sphere Probe in Multimode Operation.

Although the analysis presented in the following sections specifically address the one-sphere problem, it can be extended in a direct manner to any of the two-sphere probe geometries described. It is to be anticipated, however, that some of the two-sphere liftoff integrals may have to be performed numerically rather than analytically.

2.2 Spatial Frequency Analysis of First and Second Order Liftoff Signals

We have already shown that through the use of Lorentz reciprocity theorem the change in the impedance of an electromagnetic probe, due to the presence of a flaw, can be expressed in terms of the following integral evaluated over any closed surface containing the flaw²,

$$\Delta Z = \frac{1}{I^2} \oint (\mathbf{E} \times \mathbf{H}' - \mathbf{E}' \times \mathbf{H}) \cdot d\mathbf{s}, \quad (1)$$

where the primed characters denote perturbed fields in the presence of the flaw, with the dc bias field reversed. In the common case, where the probe is scanning a flat metallic surface defined by $z = -z_0$, the surface of integration may conveniently be taken to coincide with the initial surface of the metal (i.e. before the liftoff variation), and be closed at infinity. In this case, $d\mathbf{s} = dx dy \hat{z}$, and the ΔZ formula will simplify to,

$$\Delta Z = -\frac{1}{I^2} \int_{-\infty}^{+\infty} \int_{-\infty}^{+\infty} (E_x' H_y - E_y' H_x - E_x H_y' + E_y H_x'). \quad (2)$$

Next, we take the Fourier transform of the fields,

$$\begin{aligned} \mathbf{E}(x, y) &= \frac{1}{2\pi} \int_{-\infty}^{+\infty} \int_{-\infty}^{+\infty} \mathbf{e}(k_x, k_y) e^{i(\mathbf{r} \cdot \mathbf{k})} dk_x dk_y, \\ \mathbf{H}(x, y) &= \frac{1}{2\pi} \int_{-\infty}^{+\infty} \int_{-\infty}^{+\infty} \mathbf{h}(k_x, k_y) e^{i(\mathbf{r} \cdot \mathbf{k})} dk_x dk_y. \end{aligned} \quad (3)$$

Upon substitution of Eq.(3) into Eq.(2), the ΔZ formula is transformed into the Fourier domain,

$$\Delta Z = -\frac{1}{I^2} \int_{-\infty}^{+\infty} \int_{-\infty}^{+\infty} \delta Z_s^\perp(k) \mathbf{h}(k) \cdot \mathbf{h}'^*(-k) dk_x dk_y. \quad (4)$$

Each Fourier element $\mathbf{h}(k)$ represents a propagating or evanescent plane wave incident on the surface plus a component reflected from the surface (i.e., $\mathbf{h}(k) = \mathbf{h}_i(k)[1 - \Gamma(k)]$, where $\Gamma(k)$ is the reflection coefficient), $\delta Z_s^\perp(k)$ is the change in surface impedance of that component at the surface of integration.

In deriving Eq.(4) we have made two assumptions. First, each plane-wave component has either odd or even symmetry with respect to k , and the flaw does not affect this

symmetry. The second assumption is that all plane wave components are polarized with the electric field perpendicular to the plane of incidence. In deriving the magnetic field distributions for most practical probes, including the FMR probe, we find that both of these conditions are indeed satisfied.

In the case of probe fields with cylindrical symmetry, the Fourier integrals in Eq.(3) reduce to zero order Hankel transforms,

$$\begin{aligned} E(r) &= \int_0^{\infty} e(k) J_0(kr) k dk, \\ H(r) &= \int_0^{\infty} h(k) J_0(kr) k dk, \end{aligned} \quad (5)$$

resulting in the following one dimensional ΔZ integral,

$$\Delta Z = \frac{2\pi}{I^2} \int_0^{\infty} \delta Z_{\perp}^{\perp}(k) h(k) \cdot h'^*(k) dk. \quad (6)$$

Equations (4) and (6) are, of course, identical and may be used interchangeably. Note, also, that the electromagnetic field spectra appearing in Equations (4) and (6), are two-dimensional vectors and do not contain components perpendicular to the metallic surface.

In using the ΔZ formulas, we first assume an initial condition for which we calculate $h(k)$ and $Z_{\perp}^{\perp}(k)$. Then we allow for the conditions to change. We calculate the new magnetic field spectrum, and surface impedance, $h'(k)$ and $Z_{\perp}^{\perp'}(k)$. Substituting these values into the ΔZ formula, we then obtain the amount by which the impedance of the probe will change in going from the initial to the final condition. The condition change may contain any variations in properties and positions of materials. The probe, which is the source of the electromagnetic fields, however, has to stay fixed with respect to the surface of integration. In order to calculate liftoff effects, we define the initial condition with the metallic surface coinciding with the surface of integration. The final condition is when an extra layer of air of thickness l is introduced between the surface of integration and the surface of the metal (Fig.4). Appendix A shows the details of liftoff calculations for probe over an imperfectly conducting medium. The results are presented in terms of a Taylor expansion in powers of l ,

$$\Delta Z_{lo} = \left[\frac{\partial}{\partial l} \Delta Z_{lo} \right] l + \left[\frac{\partial^2}{\partial l^2} \Delta Z_{lo} \right] l^2 + \dots$$

A schematic diagram showing a circular probe positioned above a horizontal metal surface. The metal surface is represented by a solid line with diagonal hatching below it, labeled "metal". A dashed line is drawn parallel to the metal surface, with a vertical double-headed arrow between them labeled z_0 . The probe is a circle with a center point, labeled "probe". A vertical arrow points from the dashed line to the center of the probe, labeled $z_s^\perp(k, l)$. On the left, a bracket indicates the vertical distance from the metal surface to the dashed line.

11

The first term of course has the highest amplitude, and its phase angle is usually referred to as the liftoff direction. In practice, the component of the flaw signal ΔZ_f , in the liftoff direction falls below the liftoff noise level and can not be detected. Therefore it is best to look at the component of the signal $(\Delta Z_f)_p$, in the oscilloscope channel perpendicular to first order liftoff. If higher order liftoff terms were all in phase with the first order term, the problem of liftoff would be completely eliminated by using phase discrimination. Unfortunately that is not the case and second order liftoff does indeed have a component in the perpendicular channel. Therefore, a relevant and practical measure of the detectability of signal in the presence of liftoff is the signal-to-liftoff-noise ratio in the perpendicular scope channel,

$$\frac{S}{N} = \frac{(\Delta Z_f) \sin \beta}{(\Delta Z_{lo})_p}, \quad (7)$$

where, β is the phase angle between signal and first order liftoff. As shown in Appendix A, the liftoff noise for a one-dimensional probe, up to second order in l , is given by

$$\Delta Z_{lo} = i\omega\mu_0 \left[\frac{l}{z_0} \left(1 - \frac{1-i}{2} \frac{\delta}{z_0} \right) - \frac{l^2}{2z_0^2} \left(1 - 5 \frac{1-i}{2} \frac{\delta}{z_0} \right) \right], \quad (8)$$

where δ is the skin depth of the conducting plane. We can factor out the first order liftoff term $(\Delta Z_{lo})^1$ in order to separate the component of liftoff in the perpendicular channel. The result is,

$$\Delta Z_{lo} = \frac{l}{z_0} (\Delta Z_{lo})^1 \left[\left(\frac{z_0}{l} - 2 \right) + (1-i) \frac{\delta}{z_0} \right]. \quad (9)$$

From Eq.(9) we find the amplitude of the liftoff in the perpendicular channel to be a factor $l\delta/z_0^2$ times the first order liftoff. At this point two important points are worth mentioning: (1) Even though the first order liftoff term is proportional to ω , the perpendicular portion of liftoff $(\Delta Z_{lo})_p$, is proportional to $\sqrt{\omega}$. This, as will be discussed later, will lead to a constant signal-to-noise-ratio at high frequencies, independent of ω , (2) The $i\omega\mu_0$ factor appears in Eq.(8) only when absolute impedances are considered. If we choose to normalize ΔZ_{lo} to the impedance of the probe the $i\omega\mu_0$ dependence disappears. In this form, our results are in agreement with liftoff calculations by Dodd and Deeds⁴.

In this section we demonstrated the expansion of ΔZ_{lo} in powers of l , and showed that second order liftoff has a component in phase quadrature with first order liftoff which is the limiting factor in flaw detection. For the sake of simplicity, we chose to treat as the example, a one dimensional probe. The same type of expansion in powers of l can also be done for the FMR probe, whose first order liftoff term has been derived in Appendix B. We do not have an analytical expression for the second order liftoff term of the FMR probe, but we expect it to have the same type of relative behavior.

2.3 Flaw Interactions

The change in the impedance of a probe due to some local variation in the material properties in its vicinity, is expressible in terms of a closed surface integral involving the electromagnetic fields before and after the introduction of the flaw, Eq. (1). We have derived analytical expressions for the unperturbed magnetic field generated by an FMR probe, Eq.(B-16). If we can also calculate the perturbed field in the presence of any particular type of flaw, then we can predict the signal obtained from it, and design probes to optimize that signal. In this section we will discuss some particular flaw types for which the ΔZ has been evaluated.

One of the simple geometries for which the perturbed fields have been calculated (with restrictions on the shape of the interrogating field), is a surface flaw in the form of a rectangular slot. Denoting the length and the width of the cavity by L and W , with the x direction along L and the y direction along W , it has been shown in Ref. (5) that for a uniform interrogating field the impedance change due to the presence of the cavity is related to the unperturbed magnetic field components, H_x and H_y , through,

$$\Delta Z_f = \frac{i\omega\mu_0}{I^2} \frac{2LW}{\pi^3} [L|H_x|^2 + W|H_y|^2], \quad (10)$$

For the FMR probe, taking the inverse Fourier transform of Eq. (B-16), evaluated at the origin ($r = 0$), gives the magnetic field components H_x and H_y , directly under the probe,

$$H_i(r = 0) = -\frac{m_x \hat{x} + m_y \hat{y}}{4\pi z_0^3} [2 + 3(i - 1) \frac{\delta}{z_0}]. \quad (11)$$

Combining Eq. (10) and Eq. (11) results in,

$$\Delta Z_f = i\omega\mu_0 \frac{72LW}{\pi^3 I^2} (1 - 3 \frac{\delta}{z_0}) [L|M_x|^2 + W|M_y|^2], \quad (12)$$

M_x and M_y are the magnetization densities parallel to the two surface dimensions of the flaw, and are derivable from Eq. (C-9). Equation (12) specifies the optimum orientation of the probe with respect to the flaw. Since in general $W \ll L$, the orientation of the probe has to be such that the maximum horizontal magnetization of the probe lies parallel to the length of the crack.

The magnetization densities appearing in Eq. (12) are proportional to the rf magnetic field applied to the YIG sphere (Eq.(C-9)). This magnetic field is generated by a single

loop of wire at the center of which the sphere is located. The magnetic field at the center of the loop is, $H = I/2r_l$, r_l being the radius of the loop. Tight winding of the loop is necessary for getting good coupling between the loop and the resonator, but the thickness of the material of the loop is comparable to the size of the sphere. A reasonable number for the coupling loop radius is, $r_l \approx 1.5R_{sp}$. Therefore the magnetization density M_x may be written as, $M_x = K(I/6R_{sp})$ where $K = M_s \sin \theta / \Delta H$. The resulting form of the impedance change is,

$$\Delta Z_f = \frac{72K^2}{\pi^3 R_{sp}^2} \left(1 - 3\frac{\delta}{R_{sp}}\right) L^2 W. \quad (13)$$

Eq. (13) demonstrates the fact that ΔZ_f , or the sensitivity of the probe to the flaw increases as the probe becomes smaller. It is worth noting that in Eq. (B-19), ΔZ_{lo} does not behave in this manner, and indeed for good conductors, the liftoff signal is approximately independent of the probe size. We can conclude from this that reducing the size of the probe results in an overall improvement in the performance of the probe.

Another more realistic flaw type for which we have analytical expressions giving ΔZ_f , is the part circular closed crack or the closed part-penny crack. Ref. (6) gives the impedance change expression in terms of the surface magnetic field along the crack in the high frequency limit,

$$\Delta Z_f = \frac{c}{I^2 \sigma} |H_x|^2 [(1+i)F \frac{c}{\delta}], \quad (14)$$

where c is the radius of the circle, $2c$ being the surface length of the flaw, and F is a function of the crack shape. Again, we substitute for H_x from Eq. (11), and write the magnetization in terms of the current, obtaining,

$$\Delta Z_f = \frac{2c}{\sigma} \left(\frac{K}{9R_{sp}}\right)^2 [(1+i)F] \left(2\frac{c}{\delta} + 3\frac{c}{R_{sp}}\right). \quad (15)$$

Here again, we see clearly the enhancement we get in the amplitude of the signal by reducing the size of the sphere. It is also important to notice the frequency dependence of Eq. (15). The dependence on ω comes only from the factor c/δ , where δ is the skin depth defined as, $\delta = \sqrt{2/\omega\mu\sigma}$. Since c/δ is much greater than c/R_{sp} , we can say that ΔZ_f is proportional to $\sqrt{\omega}$. We saw in Eq. (9) that liftoff noise in the perpendicular channel is also proportional to $\sqrt{\omega}$, and therefore, signal-to-liftoff-noise ratio is independent of ω at high frequencies.

2.4 Oscillator Probes

Our theoretical analysis of the response of an eddy current probe to both flaw and liftoff proceeds by characterizing the response in terms of a change in the complex impedance ΔZ of the probe. If the FMR probe is driven at a fixed frequency as a passive probe, the impedance change of the probe is indeed what will be measured in practice. The ΔZ formulation is suitable for the analysis of the probe in this type of operation. A practical complexity involved in the passive operation of the FMR probe is the problem of maintaining the probe at the resonant frequency which changes with liftoff (as shown in Appendix C). One way of achieving this is by using an independent measure of liftoff and adjusting the frequency accordingly. This method has been used by Battelle as a liftoff suppression method. Another technique yielding the same result with greater simplicity, is operating the probe as a self-running oscillator. In this configuration we refer to the probe as an active probe. In an eddy current probe of this type, the probe circuit serves as a resonant tank circuit controlling a bipolar transistor or FET oscillator. The two measurable signal parameters (i.e. changes in the frequency $\Delta\omega$ and the strength ΔA of the oscillation) correspond to the ΔX and ΔR in the usual passive probe through the relation,

$$Z = R + iX = Q\omega_0^2 L \frac{\omega_0 - 2iQ(\omega - \omega_0)}{\omega_0^2 + 4Q^2(\omega - \omega_0)^2}, \quad (16)$$

where ω_0 and Q are the resonant frequency and the quality factor of the resonator, and L is the coupling loop inductance.

A wide choice of circuit types is available⁷ but commercial YIG oscillators always use a feedback inductor in the base for transistor circuits⁸ (or in the gate for FET circuits⁹). This creates a negative resistance R_n between the emitter and the base (or between the source and the gate), and the YIG resonator is connected across these terminals. In a well designed oscillator the effects of the coupling loop, stray impedances and transistor parameters on the frequency of oscillation are small, and the oscillation frequency is controlled by the YIG resonance. On the other hand, changes in the emitter bias current I_e , which do not significantly shift the frequency, produce large changes in the negative resistance⁸. This variation provides a mechanism for amplitude stabilization by automatic gain control⁷ and also for the readout of ΔA .

It was shown in section 2.2, that the imaginary part of the impedance change for liftoff is much larger than its real part, so that ΔZ_{lo} has a phase angle of approximately 90

degrees. The flaw signal on the other hand, is predicted theoretically to have a phase angle of approximately 45 degrees, and the component of ΔZ_f in phase quadrature with liftoff is almost entirely real. Equation (16) shows that the frequency change of the oscillator corresponds to the imaginary part of the impedance change, and the component of the flaw signal in phase quadrature with liftoff corresponds primarily to a change in the oscillator drive rather than the oscillator frequency.

In Eq. (B-19) $\Delta\omega$ in the denominator is proportional to the inverse of the resonator Q , and as was seen in section 2.3, a similar factor appears in the impedance change for a flaw. Therefore, in general,

$$\Delta Z = (K_{Re} + iK_{Im})Q^2, \quad (17)$$

where, K_{Re} and K_{Im} are functions of the dimensions and the material parameters of the probe, test piece and flaw. From Eq. (16) above it can be shown that the shift in the resonance frequency of the probe is proportional to the imaginary part of ΔZ and is given by,

$$\frac{\Delta\omega}{\omega_0} = -\frac{K_{Im}r_L}{\pi\mu_0 V(4\gamma\pi M_s)}, \quad (18)$$

i.e., it is independent of the resonator Q . A high Q is, however, necessary for good frequency stability. In Eq. (18), V is the volume of the YIG sphere, and r_L is the coupling loop radius.

The condition for stable operation of an oscillator with automatic gain control is $R + R_n = 0$. If AGC is realized by controlling the emitter bias current I_e , the relation between the real part of ΔZ_f and the change ΔI_e in bias current is therefore,

$$\Delta I_e = -\frac{(\Delta Z_f)_{Re}}{\partial R_n / \partial I_e} = -\frac{(K_f)_{Re}Q^2}{\partial R_n / \partial I_e}. \quad (19)$$

Optimization of liftoff discrimination requires a comparison of Eqs. (18) and (19) for both liftoff and flaw signals. The optimization conditions which are discussed briefly in the conclusion, may require the choice of a circuit configuration differing from that of a conventional YIG oscillator. The negative resistance argument can be applied to any type of feedback oscillator, and the choice rests on the realization of an optimal dependence of R_n on some electrical control parameter of the active element (i.e., the bias current I_e in the above example).

3.0 EXPERIMENTAL EVALUATION

3.1 Introduction

The basic FMR probe, shown in Figure 1, consists of a spherical ferromagnetic resonator (YIG) coupled to microwave circuitry with a single turn loop of wire and immersed in a dc magnetic field, which is oriented approximately parallel with the loop plane. As shown in Figure 2, electrically, the probe looks like a high-Q* tuned circuit, where the resonant frequency of the equivalent circuit is determined by the strength of the magnetic field (see Section 2.0 for more detail on FMR probe theory). When a resonating FMR probe is electromagnetically coupled to the surface of a metallic test sample by placing the probe in close proximity with the sample, altered characteristics in the samples surface and near surface are reflected in the probe as changes in its resonant frequencies as well as Q. Unfortunately changes in liftoff also vary the resonant frequency and Q.

The objective of the experimental work on this project is to develop practical and reproducible probe fabrication and electronic processing techniques that would generate and process probe resonant frequency and Q signals producing flaw and liftoff data in such a manner that they could be discriminated. The results of the project are to be demonstrated by taking flaw data from a bolt hole sample with five probes of the same design. Each probe should produce similar data from a slot located in the bolt hole. The Air Force Materials Laboratory supplied such a sample with a 0.25 mm (0.010 inch) long, 0.125 mm (0.005 inch) deep, and 0.125 mm (0.005 inch) wide slot machined in a titanium 6-4 bolt hole (see Appendix D).

The first techniques studied in this development were based on data derived from the FMR probes reflection coefficient when driven as a passive probe by a 50-ohm microwave system. Several two-frequency methods were evaluated. These multifrequency methods produced very limited results particularly when taking into

*Q is the quality factor of a tuned circuit.

account the complexity of their signal processing systems. Specifically, when FMR probes are operated in the passive mode it is necessary to either constantly sweep the drive excitation frequency about the probe resonance or hold it on or very near the resonance of the probe, which, in turn, is set by its environment (magnetic, temperature, liftoff, etc.). It should be made clear at this point that the FMR probe provides eddy current data only when being excited at or very near a resonance. This practical limitation led us to change our implementation of the FMR probe to the active mode where the probe is utilized as the resonator in a microwave transistor oscillator circuit. This arrangement has the advantage of always operating at the probe's resonant frequency, since the probe's resonance is what sets the frequency of the oscillations in the FMR probe-oscillator or active probe circuit. Data is produced by the active probe in the form of output frequency and Q of oscillation or frequency line width in terms of spectrum content in the output. Processing the frequency-based data is relatively simple with the variety of off-the-shelf microwave modules available today. However, extracting the Q information proved to be much more difficult. Our approach at detecting oscillator Q is not sensitive enough to provide Q information while simultaneously providing resonant frequency information. A cursory evaluation was performed on a dual-differential active probe, which, with proper probe matching and spacing, should provide excellent liftoff noise cancellation. Results here indicate that this concept has excellent potential, but will require further development in probe matching techniques and spacing before its full potential can be realized.

The technique used for our final demonstration active probe and signal processor generated data based solely on the resonant frequency from a single probe. The probe was set up in a test apparatus so that the flaws could be scanned by the probe. This arrangement produced flaw signals and liftoff noise simultaneously. These data were processed electronically such that the liftoff component was reduced in magnitude well below the magnitude of the smallest flaw response. Five active probes of our final design were compared to demonstrate this technique's reproducibility, in both fabrication and flaw response. Their data, which were taken on the Air Force furnished titanium bolt-hole sample, are shown in Appendix E.

3.2 Passive Probe Evaluation

3.2.1 Reflection Coefficient Signal Processor

The microwave reflection coefficient signal processor, shown in Figure 5, is the configuration utilized in this study to obtain reflection coefficient-based data on the passive probe. A schematic of this processor is shown in Appendix F. The voltage controlled oscillator provides the rf excitation (900 MHz to 1600 MHz) to the 50 ohm output. Frequency control is furnished by a laboratory function generator. The directional couplers tap off small portions (-20 dB) of the probe drive and reflection voltages for processing in the polar phase discriminator. The polar phase discriminator (or vector detector) produces two differential signal pairs, which are proportional to the rectangular coordinates of Γ , the reflection coefficient vector. In order to zero out, or null any dc offsets inherent to the electronics and establish a common starting point for the reflection coefficient versus frequency scans, the rectangular coordinates are processed through null balance circuits. This feature is enabled by pushbutton switch and consequently nulls each coordinate. One use of this feature would be to null the system working into a calibrated 50 ohm microwave load. At a given frequency this would put null at the center of a Smith chart. The gain and rotational controls set the reflection coefficient display scale and angular orientation respectively.

The reflection coefficient plot, shown in Figure 6, is a typical swept frequency response obtained with this signal processor driving a passive probe. The frequency is swept from 900 MHz (center of spiral) to 1600 MHz (outer end of spiral). The loop that occurs on the spiral just out from the center is a result of the passive probe resonating at the frequency at that point. Again, the probe's resonant frequency is a function of its magnetic environment. Therefore, by simply adjusting the strength of the magnetic field on the probe, the loop can be moved to any position along the spiral. The data shown in Figure 3 of the theoretical section were taken by Stanford with a similar processor. These data illustrate crack and liftoff responses of several passive probe configurations.

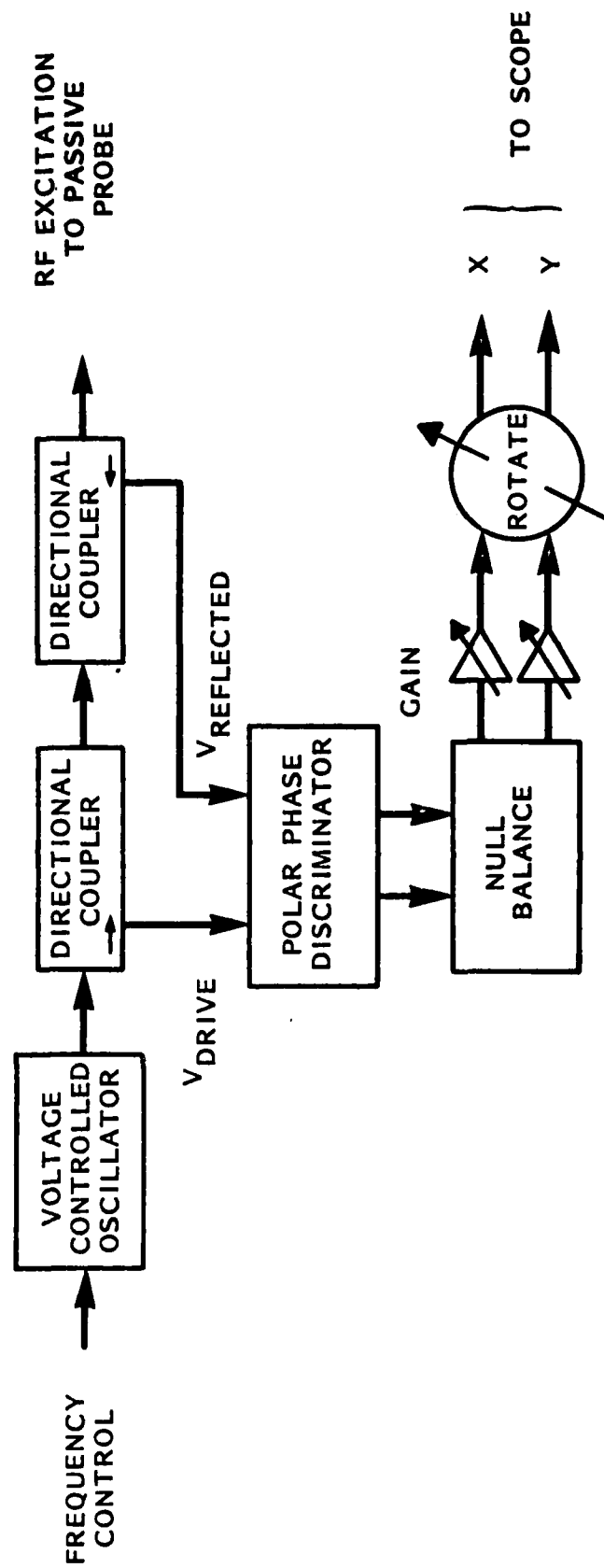


Figure 5. Microwave Reflection Coefficient Signal Processor.



Figure 6. Typical Reflection Coefficient Plot.

Another method of displaying reflection coefficient characteristics is illustrated in Figure 7. These data were plotted by driving the horizontal axis with the frequency control voltage and the vertical axis with the detected reflected voltage amplitude. These plots graphically illustrate the effect of liftoff on the resonant frequency and Q of the FMR probe.

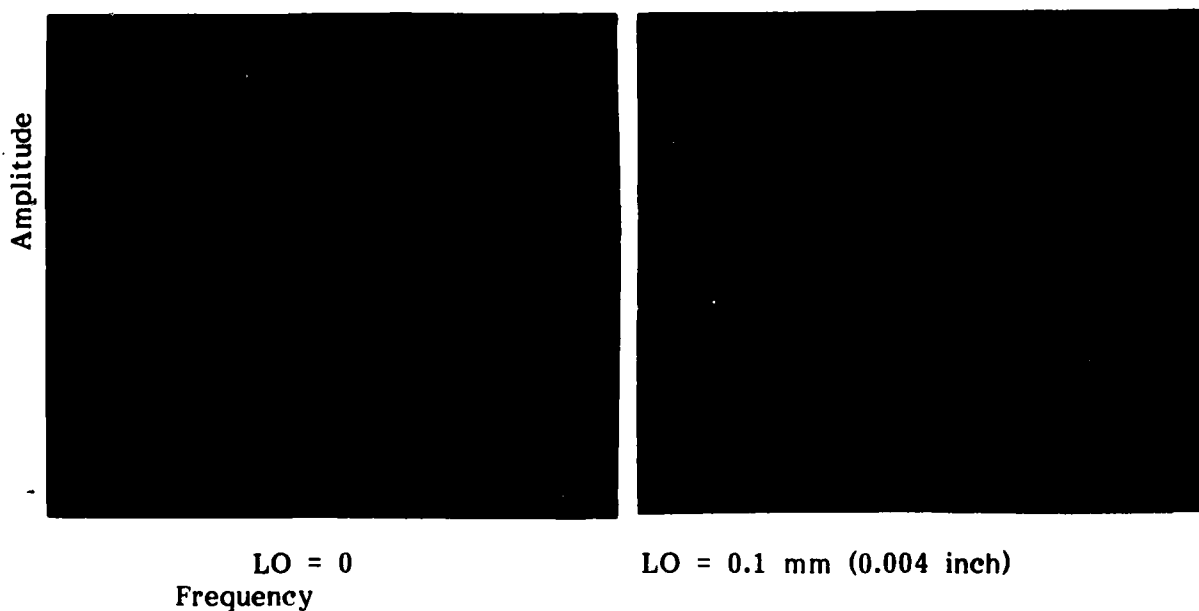


Figure 7. Reflected Voltage Versus Drive Frequency Plots.

3.2.2 Two-Frequency Microwave Experiments

The least successful methods of liftoff compensation we evaluated used two-frequency microwave tests patterned after conventional low frequency (less than 10 MHz) multifrequency tests. Two cases were evaluated: (1) the magnetic field was maintained at a constant value while the frequency of the microwave oscillator was switched for a narrow band test, and (2) both the magnetic field and the oscillator frequency were switched simultaneously for a wide band test. Switching frequencies of up to 300 Hz were used for both cases. The rectangular coordinates of the reflection coefficient from the probe were sampled during appropriate dwell times by four sample-hole circuits. The result was the direct equivalent of a simultaneous two-frequency test.

The microwave narrow band two-frequency test configuration is shown in Figure 8. For this test the two frequencies were positioned very near and on either side of the probe resonance as indicated. The detected outputs from each frequency were extremely dissimilar and could not be mixed to obtain any reduction of liftoff.⁽¹⁷⁾ Since liftoff results in a variation of the sphere resonance frequency, the resonance loop would roll right or left through one or the other of the test frequency locations as liftoff was varied. The two test frequency channels were thus affected in different manners and at differing ranges of liftoff, and were totally unsuitable for multiparameter linear mixing.

The microwave wideband two-frequency test configuration is shown in Figure 9. The frequency of the microwave oscillator was switched between the two probe resonances in synchronism with the magnetic field. A plot of the probe reflection coefficient is shown illustrating the two resonances superimposed on a frequency sweep. Our results showed that there was no independence of data between these two test frequencies (900 MHz and 1400 MHz). Both flaw and liftoff data respectively were similar at each frequency. Thus the attempts to suppress liftoff with multiparameter mixing resulted in a simultaneous suppression of flaw data. The conclusion is that a much wider separation in test frequencies would be required to obtain multiparameter suppression of liftoff.

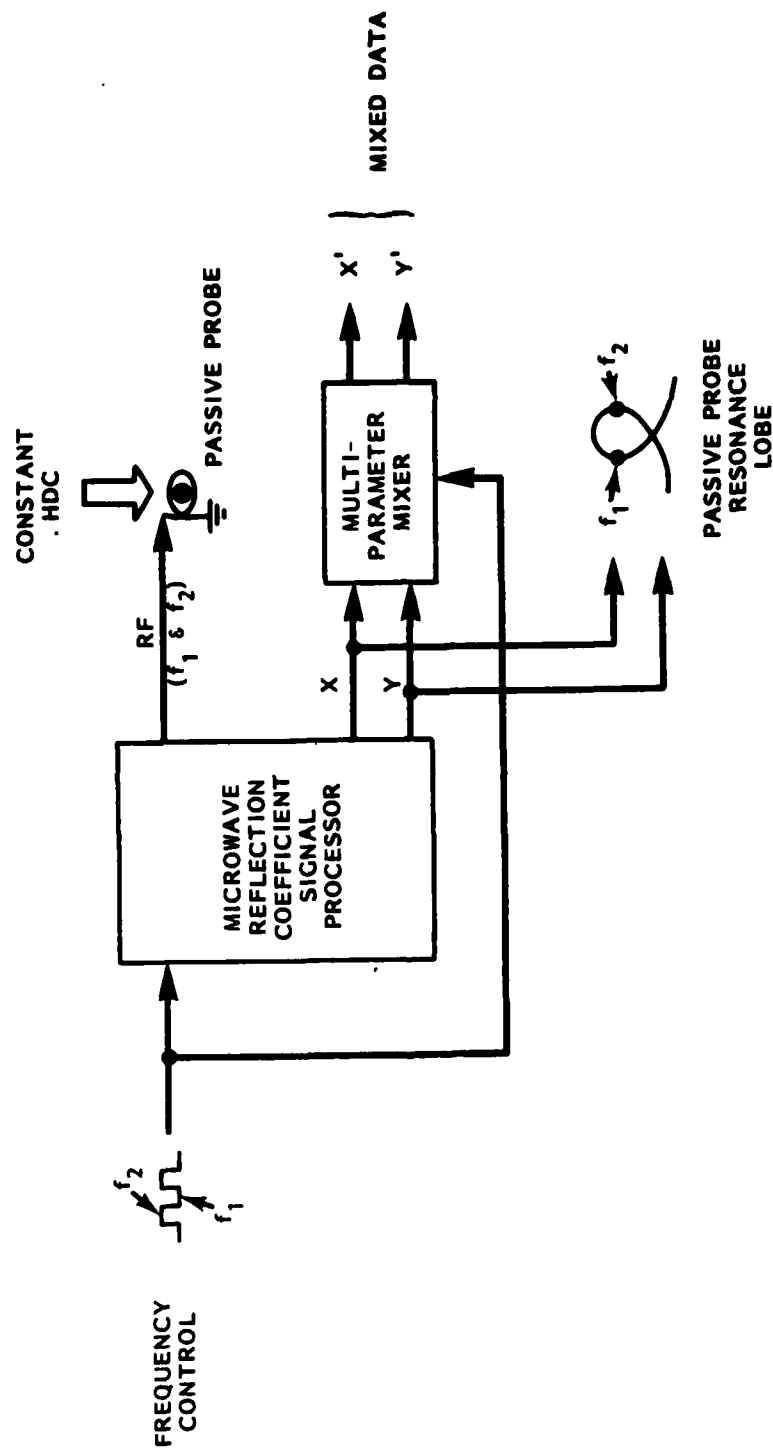


Figure 8. Microwave Narrow Band Two-Frequency Test Configuration.

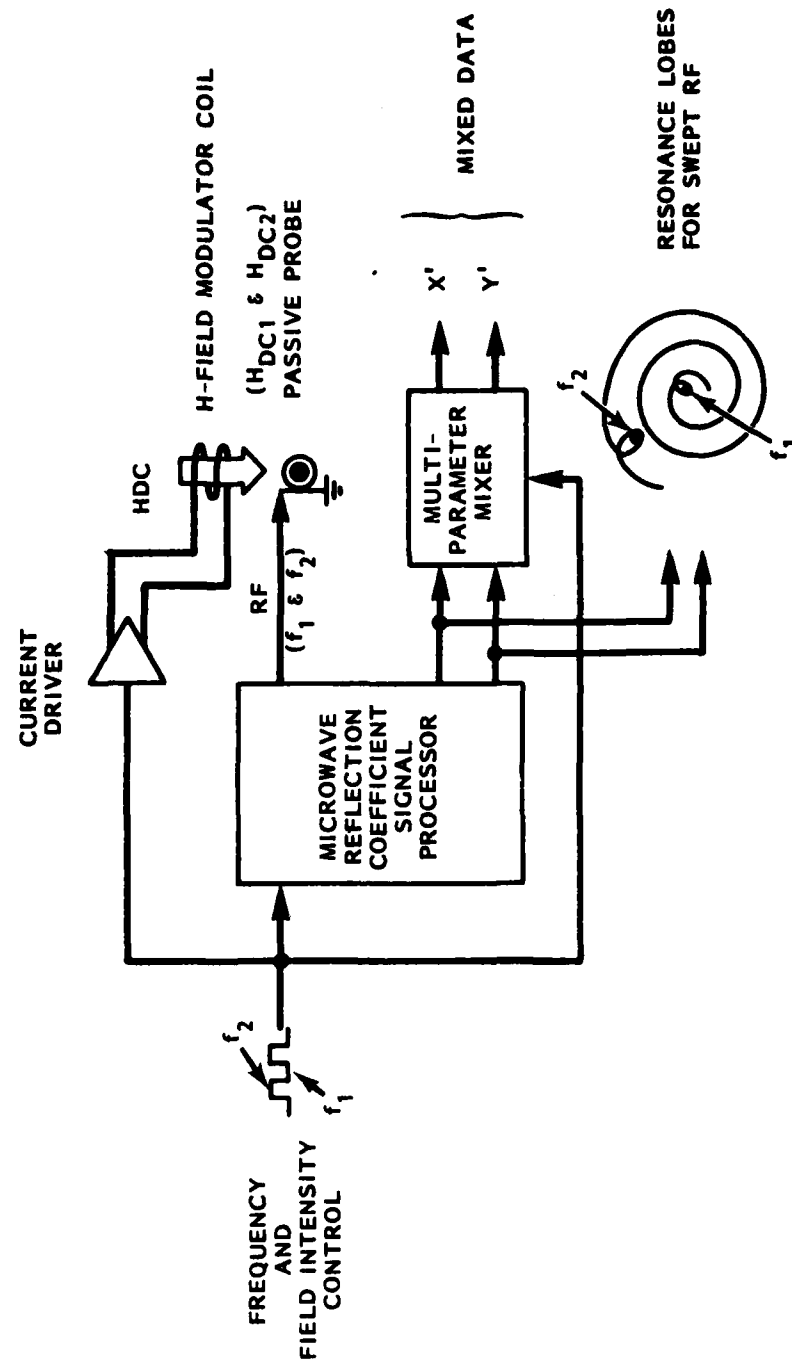


Figure 9. Microwave Wide Band Two-Frequency Test Configuration.

3.2.3 Liftoff Suppression Using 200 kHz Liftoff Detection

In this experiment a conventional 200-kHz, eddy current liftoff detection arrangement was integrated into the microwave reflection coefficient system operating at a fixed drive frequency. The resulting configuration, shown in Figure 10, is set up so that liftoff data detected with a liftoff sensing coil is fed to an electromagnet coil which modulates the dc magnetic field. The result is a regulation of the FMR probe's liftoff-dependent resonant frequency. The response of this suppression scheme is shown in Figure 11 where it is combined with the normal (unsuppressed) response. Approximately an eight-to-one reduction of liftoff-induced frequency shift over the FMR probe's usable range of liftoff is apparent in the suppressed data. Flaw sensitivity is unaffected by the technique, which therefore constitutes an eight-to-one signal to noise increase from the passive probe.

The coil arrangement used for this scheme is shown in Figure 12. A liftoff sensing coil is located close to the YIG sphere. It projects a somewhat larger search field than the sphere and thus may be located so that the sphere's microwave frequency field does not couple with it. A large electromagnet is then wound around and above the eddy current coil so that it will couple to the YIG sphere. A slotted copper shield is used to suppress coupling between the eddy current coil and the electromagnet.

A second method of implementing this liftoff suppression technique was evaluated which used a shared coil for both liftoff sensing and bias field modulation. A large electromagnet coil was ac coupled to the eddy current instrument and dc coupled to the current driver. The results of this work are shown in Figure 13. The degree of liftoff suppression obtained is inferior to that provided by the two-coil method. This result is attributed to cross-talk between the eddy current instrument and the current driver. It was found that the bias field from the electromagnet altered the ac incremental permeability of the dc field magnet by a small amount. This resulted in a change in the ac impedance of the low-frequency coil with a dc bias field since the ac field also encompassed the dc field magnet. The solution to this problem was to use a smaller eddy-current liftoff sensing coil so that its flux did not link with the dc magnet.

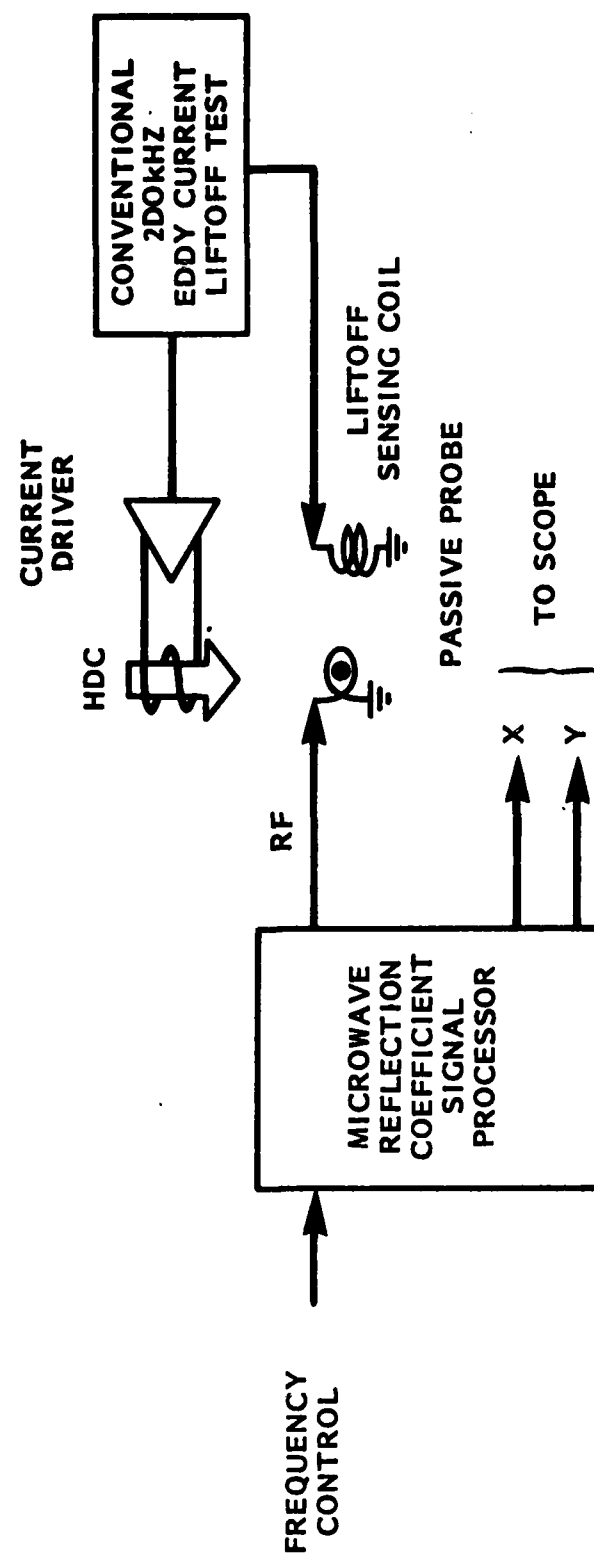


Figure 10. Passive Probe in Two-Coil Liffoff Suppression Configuration.

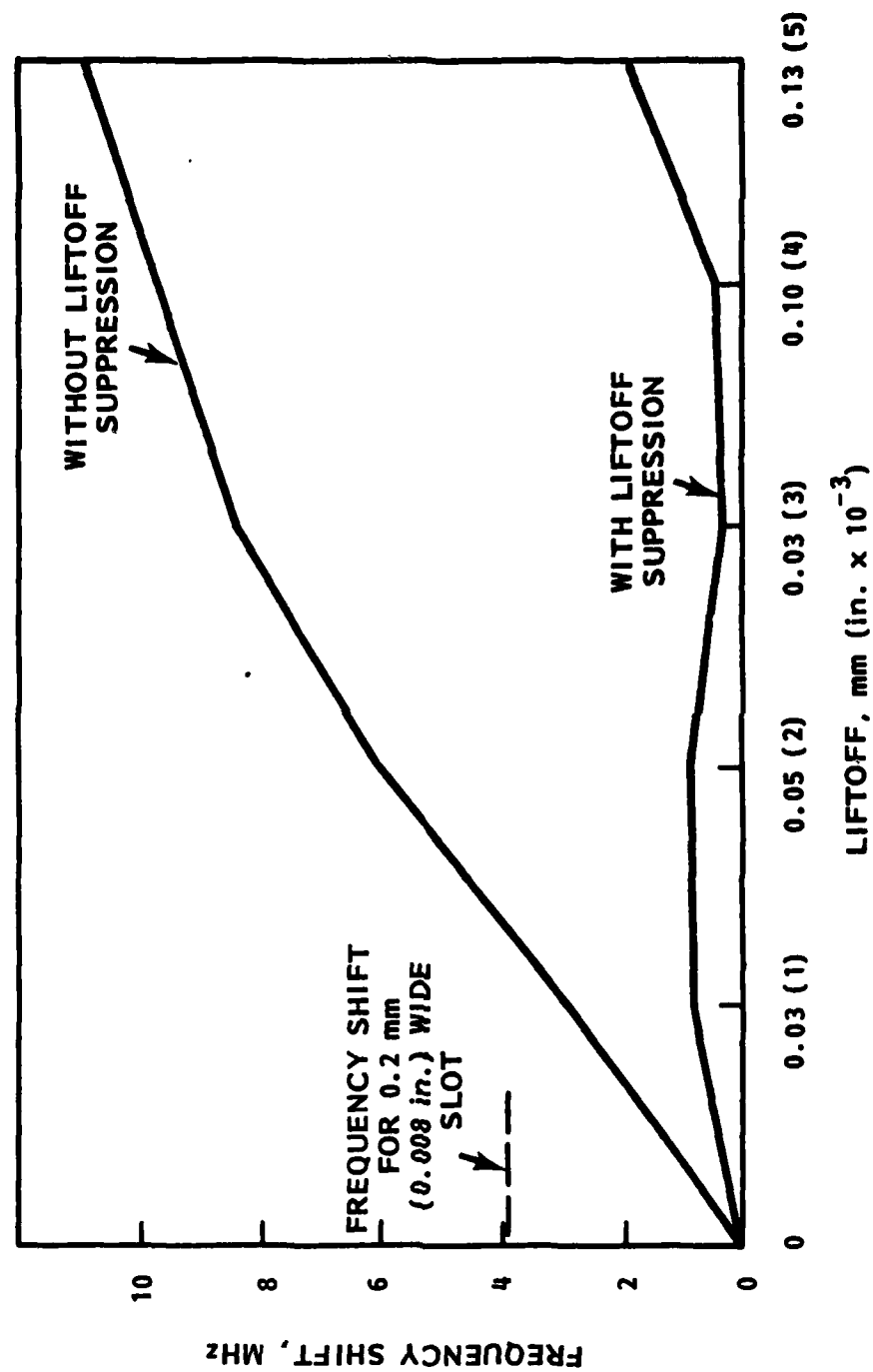


Figure 11. Liftoff Suppression Obtained with Two-Coil Method.

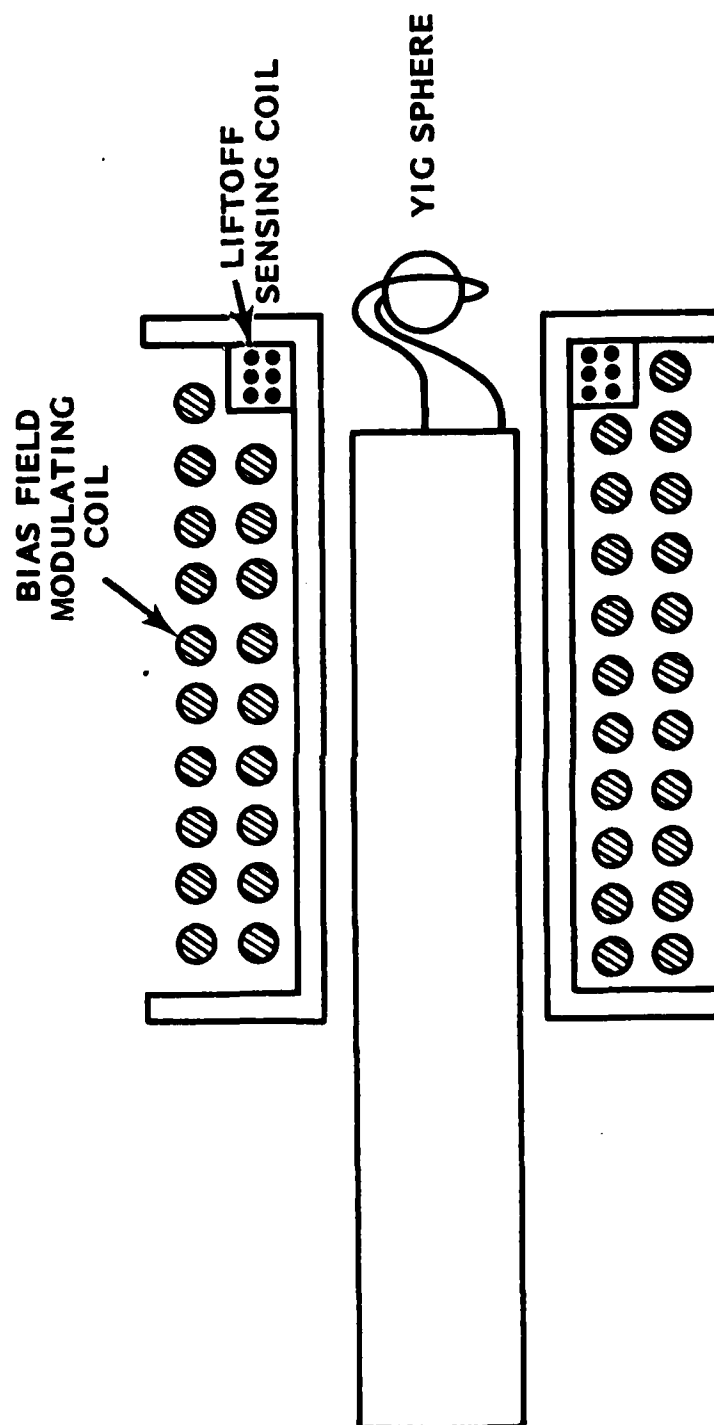


Figure 12. Two-Coil Probe Arrangement.

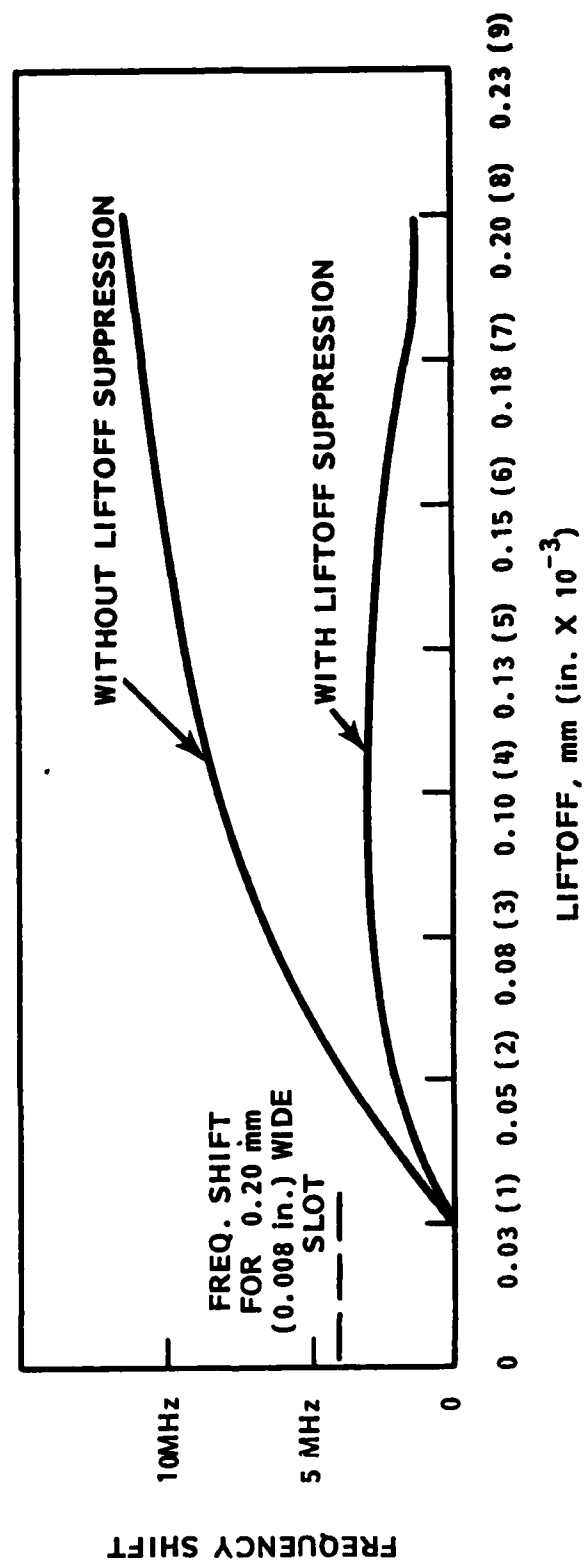


Figure 13. Lift-off Suppression Obtained with Shared Coil Method.

A conceptual design of a passive bolt hole probe is shown in Figure 14. A right angle bend is made in the rigid coaxial cable and the bias field is provided by a U-shaped magnet. The magnet is designed to bias the YIG sphere with a nearly uni-directional field which will be at right angles to the desired rf search field. We have determined that a bias field on the order of 200 to 400 gauss will be required to operate FMR probes at a frequency of 1000 MHz. The liftoff sensing coil fits conveniently in the magnet air gap. Bias modulating coils are wound around the legs or pole pieces of the magnet for correcting the resonant frequency against liftoff and/or tilt. A wear face can be installed on the front of the probe and held in intimate contact with the surface to be inspected by spring loading.

3.3 Active Probe Evaluation

3.3.1 Active Probe Signal Processor

Since the data from an active probe is carried primarily in the frequency of oscillation out of the device, it was necessary to design and breadboard a signal processor which would provide microwave frequency-to-voltage conversion. A block diagram of the signal processor is shown in Figure 15. The first step in the process is to down-convert the microwave frequency to a value that is easy to work with, yet large enough to cover the possible frequency excursions that might be produced in the active probe during sample inspection. To accomplish this, the active probe output is fed into the receiver port of a double-balanced mixer and a reference oscillator output is fed into the local port. The reference oscillator output is set to produce a difference frequency at the IF port of approximately 35 MHz. The 35-MHz IF signal is then fed into a frequency-to-voltage (F/V) converter which outputs a voltage level proportional to the frequency at its input. To help provide a clearer picture as to the potential sensitivity of the active probe, an active second-order highpass filter (HPF) was added to filter out slow varying components of liftoff noise. A schematic of this processor is shown in Appendix F.

3.3.2 Mechanical Test Apparatus

In order to enable evaluation of the active FMR probes in a simulated dynamic

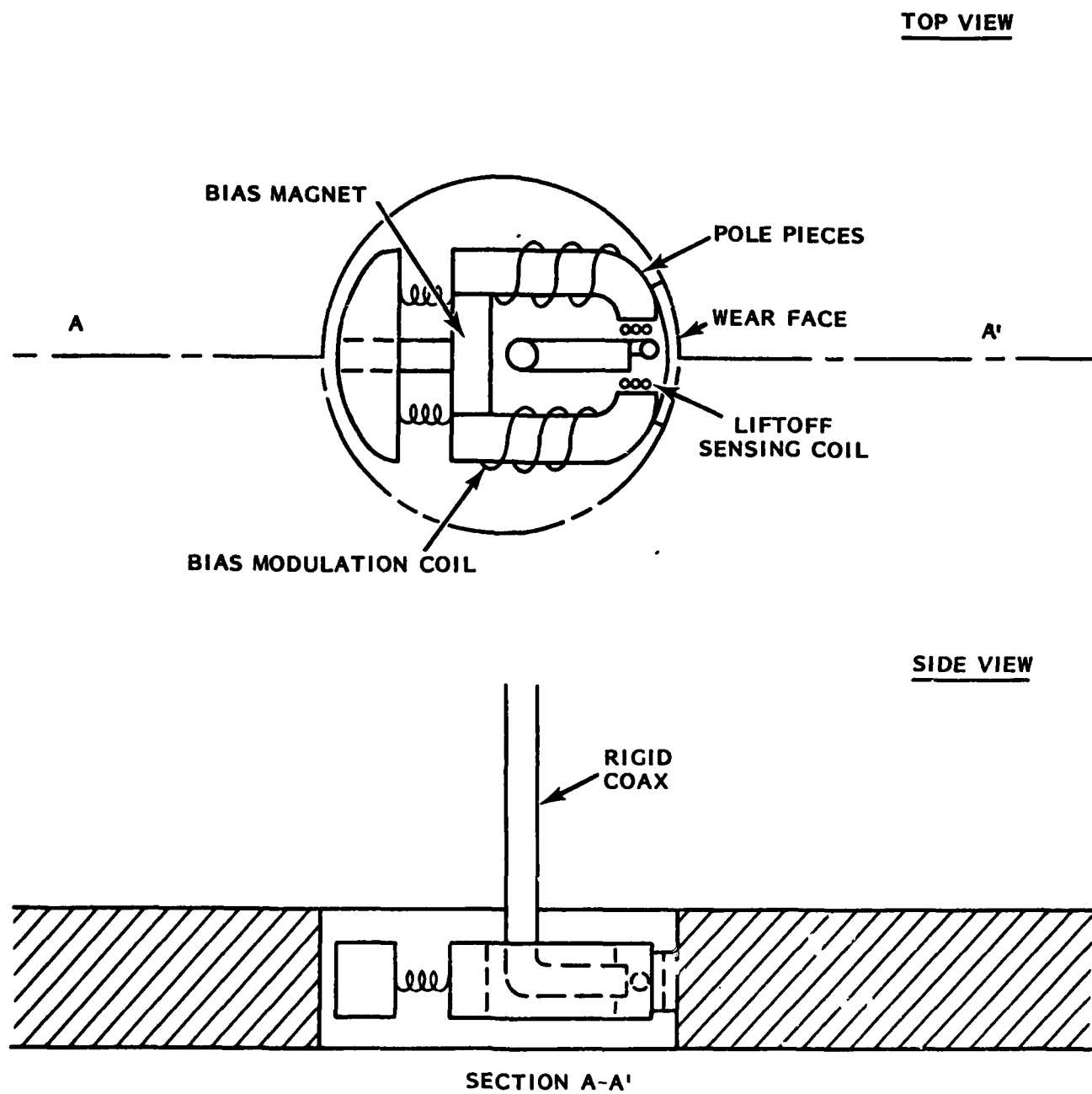


Figure 14. Conceptual Design of Passive Bolt Hole Probe.

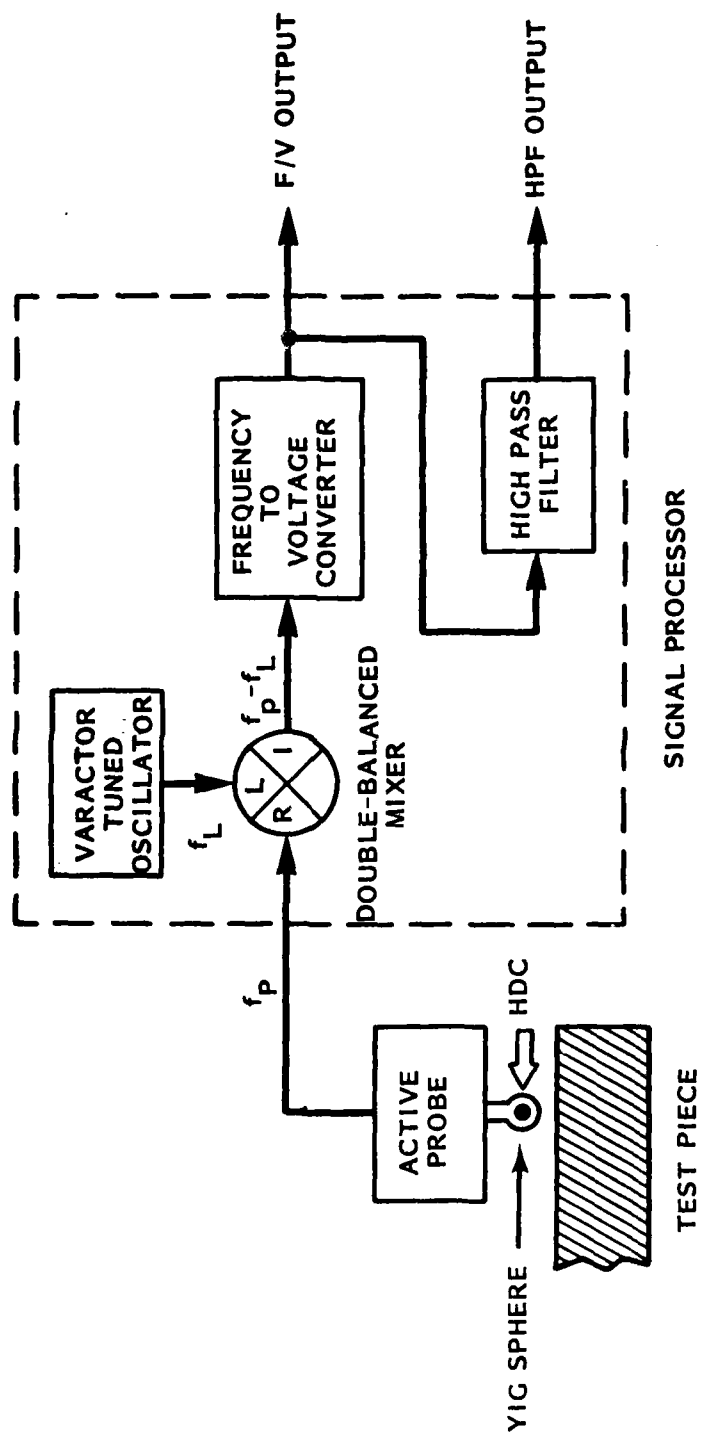


Figure 15. Active Probe Signal Processor.

inspection condition, it was necessary to construct the test apparatus shown in Figure 16. The apparatus consists of a 3-axis micropositioner for the probe, a variable speed rotating platform, and a test piece shown mounted on the platform. The test piece, detailed in Figure 17, is a titanium alloy disk with a variety of EDM notches in it. Photographs of these notches are shown in Appendix D, which indicate that several of the notches are far from ideal. However, notches 2 and 3, which have the minimum size goals for this project, came out fairly clean. To utilize the apparatus the active probe is positioned over the rotating disk with a fixed liftoff so there is no contact between the probe and the disk surface. The rotational speed is set to get the optimum results from the signal processor.

3.3.3 Probe Permanent Magnet/Pole Piece Configuration

Before proceeding, it should be noted that the characteristics of a YIG FMR resonator are such that the cleanest (minimum spurs and jitter) and strongest resonant conditions occur when the dc magnetic field surrounding the sphere is uniform. Also, for best flaw sensitivity when utilized as an eddy current probe, the field direction should be approximately parallel with the probe loop plane which in turn must be approximately parallel with the metallic surface to be tested.

Two approaches were evaluated for providing the dc magnetic field in the final demonstration probe. The prime objectives are to provide the proper field direction, strength and uniformity to obtain the desired performance and operating frequency from the probe. One approach is a single samarium cobalt (SmCo) cube-shaped permanent magnet (PM) positioned near the sphere/loop. This is the approach used on several active probes described in this report. This approach is simple and adequate when physically large PMs, in relation to the sphere, were used. The question arises as to the adequacy of this technique when the physical constraints of the probe require that the PM can no longer be positioned in the probe package such that conditions for magnetic precession occur uniformly throughout the sphere. Experiments on active probes were performed using 12.5 mm (0.5 inch), 6 mm (0.24 inch), and 2.7 mm (0.11 inch) cubes of SmCo 18, which for the larger cubes produced approximately 3000 gauss measured on either primary side. It is relatively easy to create adequate magnetic conditions for clean probe resonance with the two larger

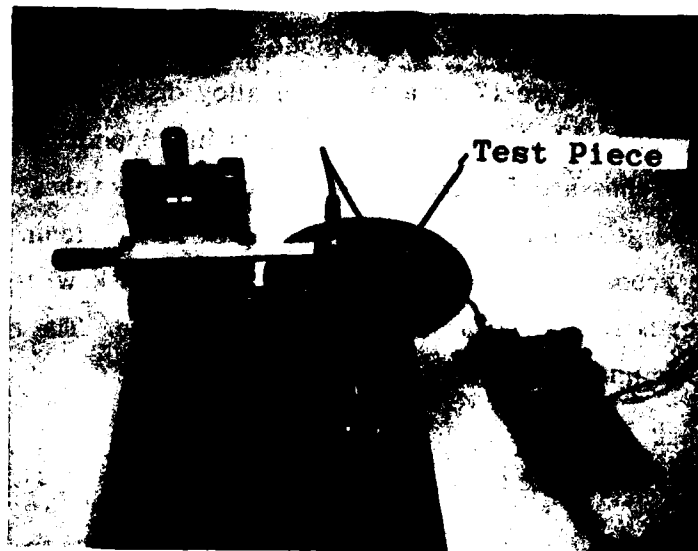
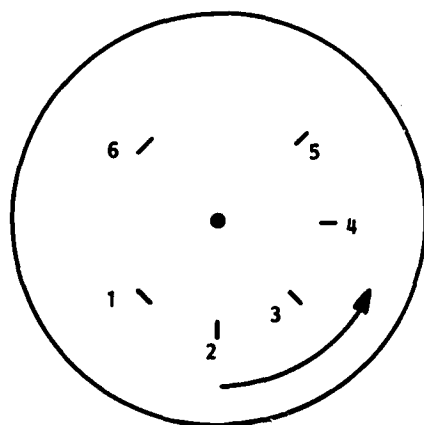


Figure 16. Mechanical Test Apparatus.



TITANIUM DISK

	L	W	D	mm (inch)
6	0.48 (0.019)	0.30 (0.012)	0.25 (0.010)	
5	0.43 (0.017)	0.14 (0.006)	0.25 (0.010)	
4	0.42 (0.017)	0.14 (0.006)	0.13 (0.005)	
3	0.24 (0.010)	0.13 (0.005)	0.25 (0.010)	
2	0.22 (0.009)	0.12 (0.005)	0.13 (0.005)	
1	0.36 (0.014)	0.36 (0.014)	0.25 (0.010)	

EDM NOTCH DIMENSIONS

Figure 17. Titanium Test Piece and Notch Dimensions.

cube sizes. However, the 2.7 mm (0.11 inch) cube apparently did not have adequate field strength and uniformity for resonance to occur in the operating range of the active probes fabricated in this study, which was 800 MHz to 1100 MHz typically. The YIG FMR sphere used in these probes is 0.73 mm (0.029 inch) in diameter which is approximately one-fourth the smallest cube size. It is highly probable that going to a smaller sphere size would allow the use of the smaller PM cube. For instance, a 0.30 mm (0.012 inch) sphere would provide approximately the same relative PM cube to sphere size as several of our successful active probes have with the 6 mm (0.24 inch) cubes. However, this remains to be confirmed experimentally.

The other approach that was evaluated and selected for our demonstration probe design is shown in Figure 18. It consists of a SmCo PM with two pole pieces to create a magnetic field of proper strength, orientation and uniformity throughout

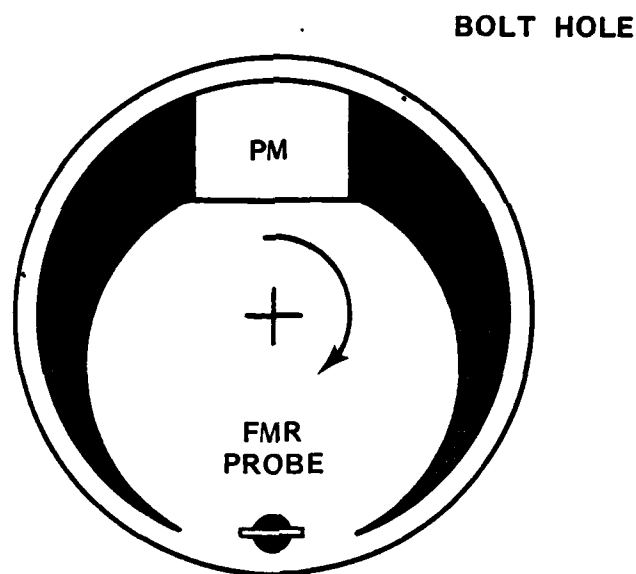


Figure 18. Permanent Magnet (PM)/Pole Piece Arrangement for Bolt Hole Probe.

the volume of the FMR probe. It was found experimentally that the knife edge pole pieces provided a fairly uniform magnetic field in an area much larger than the sphere diameter. The width of the pole pieces at the knife edges is approximately 4.5 mm (0.18 inch). As seen in Figure 18, in order to reduce liftoff, it is necessary to locate the FMR probe outside of the direct line between the pole piece tips due

to the curved inspection surface. This approach can be miniaturized, possibly by actually machining the pole pieces from PM material, to accommodate small active FMR probe configurations.

3.3.4 2 GHz Active Probe Test

The initial active FMR probe evaluation was performed utilizing the active probe furnished to Battelle by Stanford. This probe, shown in Figure 19, consists of an 800-gauss, YIG sphere, loop-coupled to an active negative resistance microwave oscillator circuit. The dc magnetic field is supplied by a single 12.5 mm (0.5 inch) SmCo permanent magnet. Its position and orientation are set to provide the field strength, direction and uniformity at the sphere to allow magnetic precession to occur at 2 GHz. Data were taken with this probe at a liftoff of approximately .1 mm (0.004 inch). The figure identifies which response came from which EDM notch (refer to Figure 17 for notch dimensions). The spikes in the F/V output are notch responses, and the slower moving components are liftoff noise. The largest spike is the result of notch #6 and corresponds to a 2.5-MHz frequency shift in the active probe's output. The slower moving liftoff components also cover approximately 2.5 MHz in frequency shift, which corresponds to approximately 0.013 mm (0.0005 inch) of total wobble in the liftoff. The liftoff components are a result of dimensional inaccuracies in the test apparatus and of the vibration in the drive system. With the use of shim stock, the wobble caused by the dimensional inaccuracies can either be minimized or amplified to evaluate the flaw/ liftoff performance of probe. The HPF output data has had the liftoff noise removed with high pass filtering, which is set to pass the high-speed spikes and remove the slowly moving liftoff components. The HPF output illustrates more clearly the relationship of probe responses to various sizes of EDM notches.

3.3.5 900 MHz Active Probe Development and Test

Several YIG-based microwave oscillators have been designed and fabricated at Battelle during the demonstration probe development. An important design goal, of course, is to design the oscillator circuit to resonate the YIG probe in a specific frequency range. It should be noted at this point that one of the most difficult

cube sizes. However, the 2.7 mm (0.11 inch) cube apparently did not have adequate field strength and uniformity for resonance to occur in the operating range of the active probes fabricated in this study, which was 800 MHz to 1100 MHz typically. The YIG FMR sphere used in these probes is 0.73 mm (0.029 inch) in diameter which is approximately one-fourth the smallest cube size. It is highly probable that going to a smaller sphere size would allow the use of the smaller PM cube. For instance, a 0.30 mm (0.012 inch) sphere would provide approximately the same relative PM cube to sphere size as several of our successful active probes have with the 6 mm (0.24 inch) cubes. However, this remains to be confirmed experimentally.

The other approach that was evaluated and selected for our demonstration probe design is shown in Figure 18. It consists of a SmCo PM with two pole pieces to create a magnetic field of proper strength, orientation and uniformity throughout

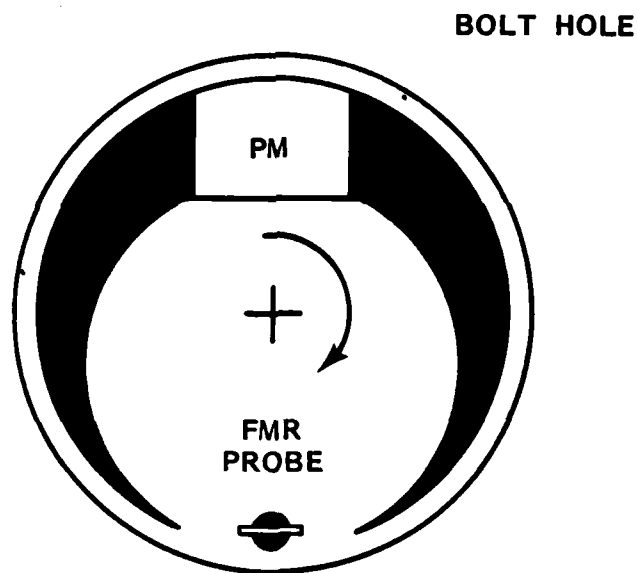


Figure 18. Permanent Magnet (PM)/Pole Piece Arrangement for Bolt Hole Probe.

the volume of the FMR probe. It was found experimentally that the knife edge pole pieces provided a fairly uniform magnetic field in an area much larger than the sphere diameter. The width of the pole pieces at the knife edges is approximately 4.5 mm (0.18 inch). As seen in Figure 18, in order to reduce liftoff, it is necessary to locate the FMR probe outside of the direct line between the pole piece tips due

to the curved inspection surface. This approach can be miniaturized, possibly by actually machining the pole pieces from PM material, to accommodate small active FMR probe configurations.

3.3.4 2 GHz Active Probe Test

The initial active FMR probe evaluation was performed utilizing the active probe furnished to Battelle by Stanford. This probe, shown in Figure 19, consists of an 800-gauss, YIG sphere, loop-coupled to an active negative resistance microwave oscillator circuit. The dc magnetic field is supplied by a single 12.5 mm (0.5 inch) SmCo permanent magnet. Its position and orientation are set to provide the field strength, direction and uniformity at the sphere to allow magnetic precession to occur at 2 GHz. Data were taken with this probe at a liftoff of approximately .1 mm (0.004 inch). The figure identifies which response came from which EDM notch (refer to Figure 17 for notch dimensions). The spikes in the F/V output are notch responses, and the slower moving components are liftoff noise. The largest spike is the result of notch #6 and corresponds to a 2.5-MHz frequency shift in the active probe's output. The slower moving liftoff components also cover approximately 2.5 MHz in frequency shift, which corresponds to approximately 0.013 mm (0.0005 inch) of total wobble in the liftoff. The liftoff components are a result of dimensional inaccuracies in the test apparatus and of the vibration in the drive system. With the use of shim stock, the wobble caused by the dimensional inaccuracies can either be minimized or amplified to evaluate the flaw/ liftoff performance of probe. The HPF output data has had the liftoff noise removed with high pass filtering, which is set to pass the high-speed spikes and remove the slowly moving liftoff components. The HPF output illustrates more clearly the relationship of probe responses to various sizes of EDM notches.

3.3.5 900 MHz Active Probe Development and Test

Several YIG-based microwave oscillators have been designed and fabricated at Battelle during the demonstration probe development. An important design goal, of course, is to design the oscillator circuit to resonate the YIG probe in a specific frequency range. It should be noted at this point that one of the most difficult

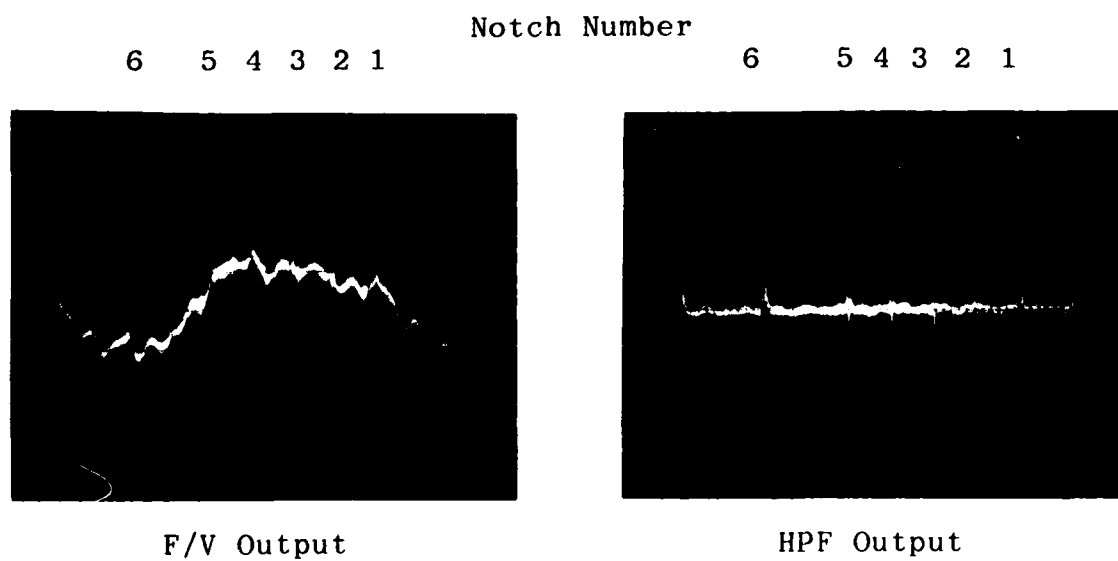
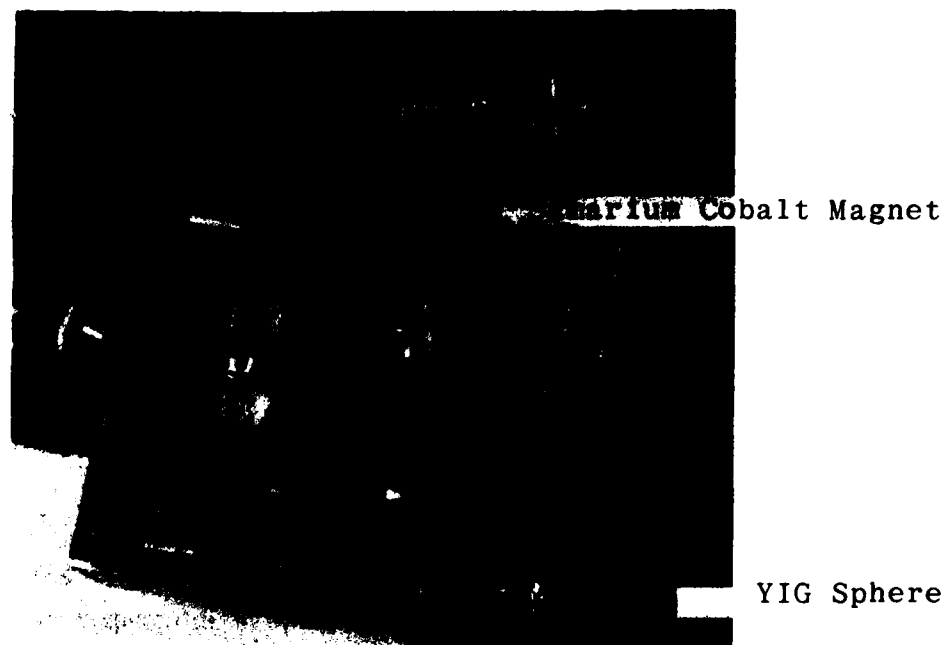


Figure 19. 2 GHz Active Probe with Data Taken on Titanium Test Piece.

steps in probe fabrication is the positioning of the dc magnetic field source. This problem can be made much easier if the YIG-based oscillator is designed with a wide operating bandwidth. A wide operating bandwidth means that the active probe will resonate over a relatively wide range of magnetic field strengths and, therefore, field source positions. To aid in the evaluation of the YIG-oscillator operating bandwidth, the variable flux density source shown in Figure 20 was constructed. This allows the resonant frequency of the YIG sphere to be swept without repositioning the permanent magnet (PM), while monitoring the oscillator output on a sampling oscilloscope and spectrum analyzer. After evaluating several designs, one was chosen, and the active probe circuit shown in Figure 21 was fabricated. The probe shown in Figure 22 consists of a 250-gauss, 0.74 mm (0.029 inch) diameter YIG sphere (Watkins-Johnson 5118-02529) loop-coupled to an active, negative resistance microwave oscillator circuit. The dc magnetic field is supplied by a 6 mm (0.24 inch) SmCo PM cube shown in the lower left of the photograph. The connector is a 50 ohm SMA type connector. This active probe configuration could be made much smaller by utilizing microwave integrated circuit fabrication techniques and a miniaturized PM/pole-piece arrangement as the magnetic field source. The data were taken with this probe operating at 900 MHz and at a 0.05 mm (0.002 inch) liftoff setting. These data were taken using the same test apparatus and titanium disk used with the 2-GHz, Stanford furnished active probe. The large spike in the F/V output, caused by EDM notch #6, represents a 2-MHz shift in probe frequency. The total liftoff component of the waveform also represents approximately 2 MHz which translates to 0.18 mm (0.0007 inch) of liftoff wobble. Similar data were observed with this probe operating as low as 550 MHz, which is approaching the critical frequency (470 MHz) of the 250 gauss YIG sphere. The liftoff characteristics of this probe are plotted in Figure 23, showing F/V output voltage and change in oscillator frequency as a function of liftoff. These data will serve as a baseline for further probe development. The aluminum specimen with a tight fatigue crack, shown in Appendix D, was examined with this probe. A frequency shift of 0.4 MHz was observed as the probe was passed over the tight crack. In comparison, the EDM-notch data taken with this same probe ranged from 2-MHz shift for the largest EDM notch (#6) and 0.3-MHz shift for the smallest EDM notch (#2), both of which are readily detectable. This verifies the FMR probe's capability to detect tight as well as open crack-like flaws.

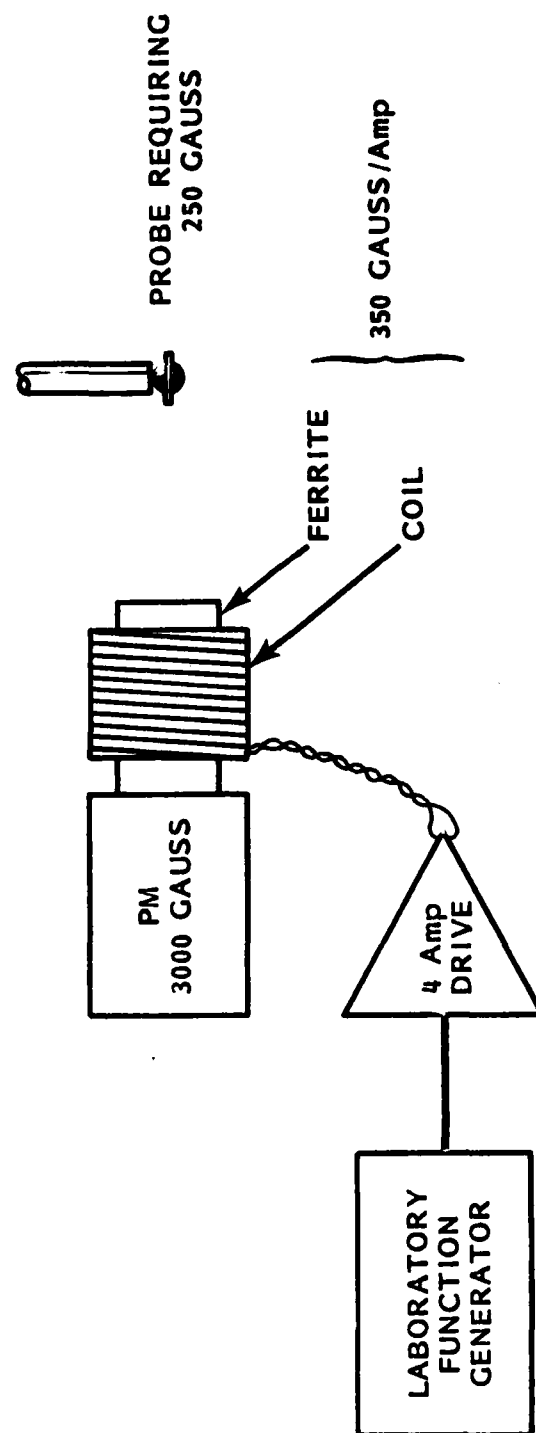


Figure 20. Variable Strength dc Magnetic Field Source.

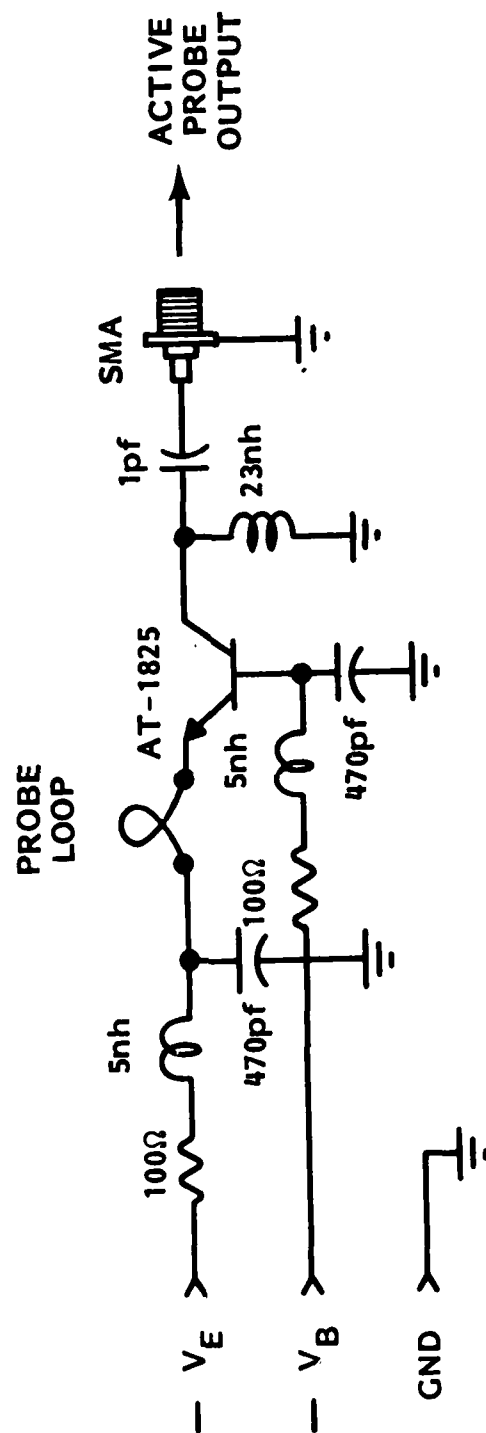


Figure 21. Initial 900 MHz Active Probe Circuit Diagram.

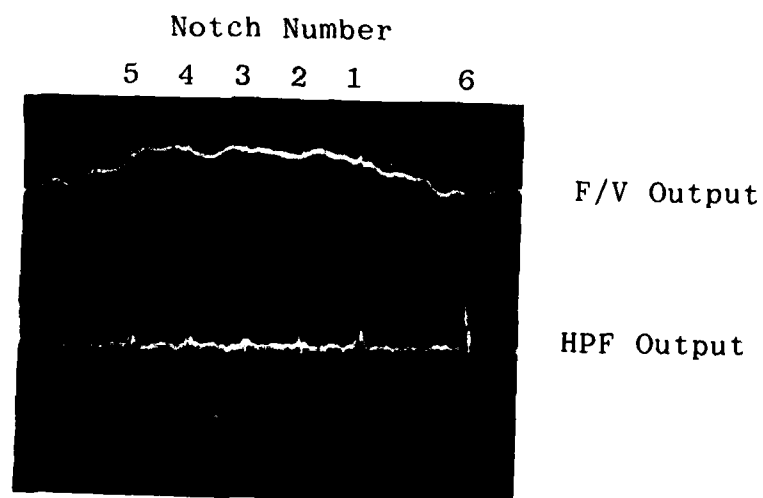
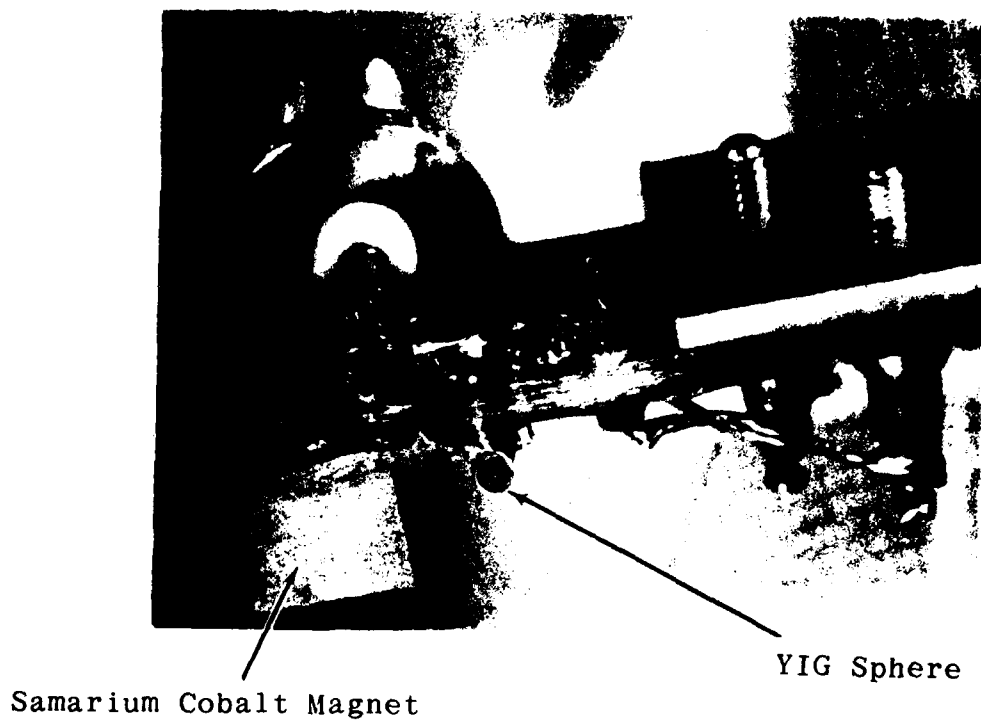


Figure 22. Initial 900 MHz Active Probe with Data Taken on Titanium Test Piece.

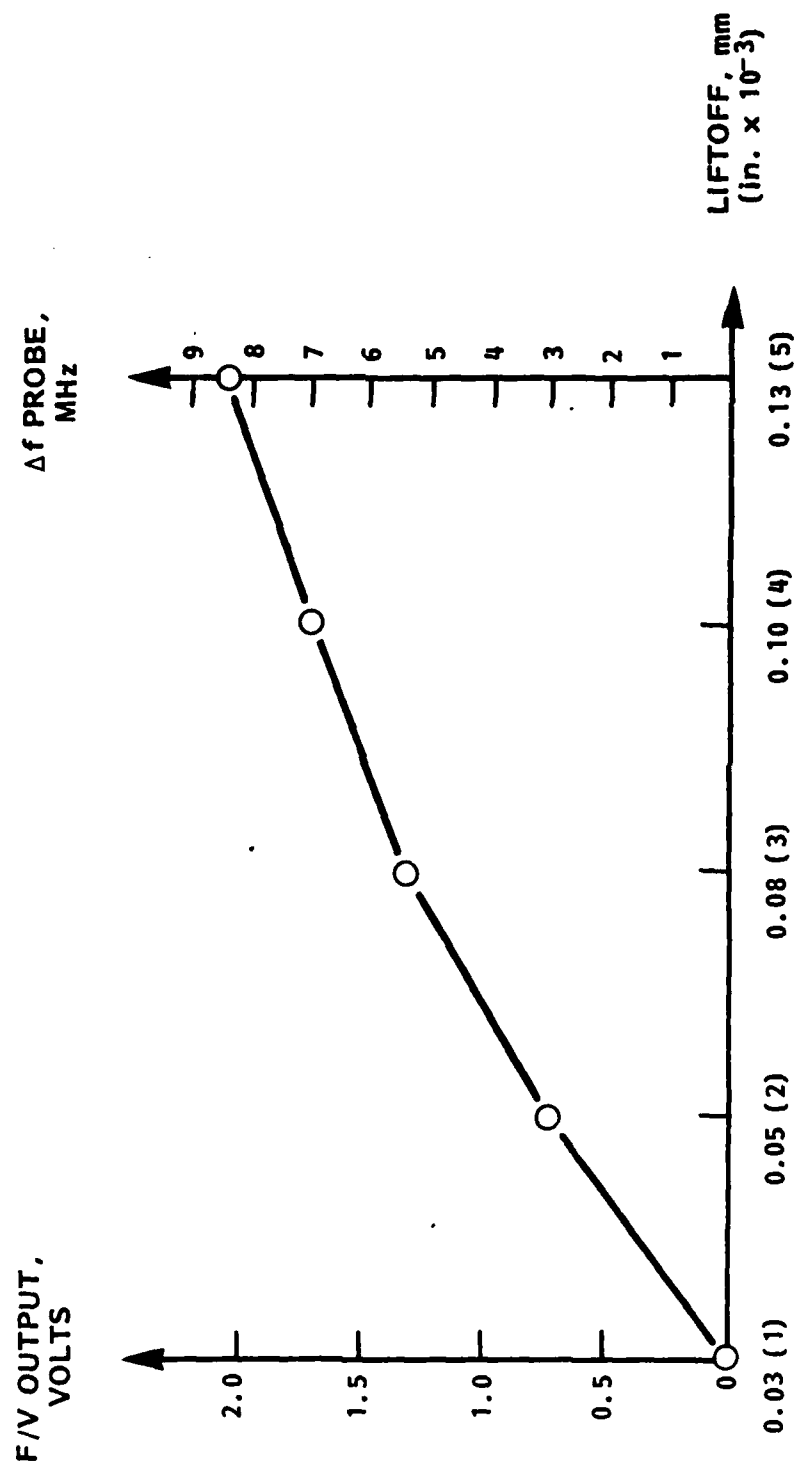


Figure 23. Initial 900 MHz Active Probe Liftoff Characteristics.

Another oscillator design evaluated is shown in Figure 24. This design is more suited for laboratory evaluation with its improved fabrication and setup techniques. The major change is in the output matching circuit which uses a length of 50-ohm

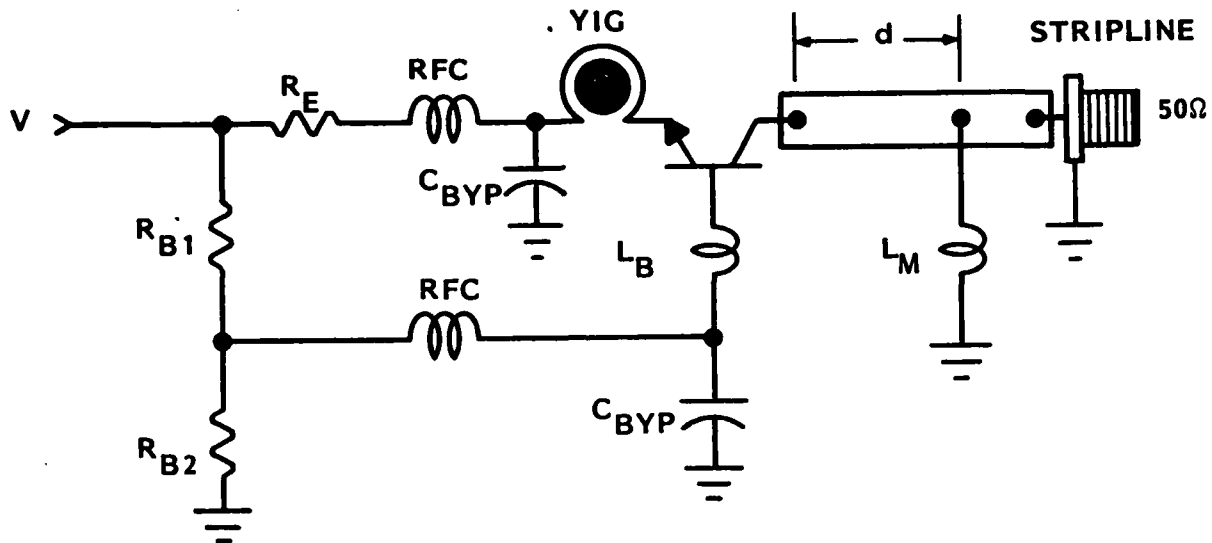


Figure 24. Improved Active Probe Design for Easier Laboratory Evaluation.

transmission line and an inductor (L_m) to set the reflection coefficient into which the transistor collector works. The reflection coefficient can be placed anywhere on the Smith chart ($\Gamma < 1$). The magnitude is determined by L_m and the angle by the distance between the collector and the L_m connection (d). This method allows relatively easy adjustment of the output-load matching circuit without having to deal with chip capacitors, which tend to make adjustments difficult at best. Once an output matching-circuit reflection coefficient has been found that gives the desired performance, such as a wide oscillator operational bandwidth, it can be replaced with a fixed lumped element L_m and C_m combination which will provide the same reflection coefficient but in a physically smaller volume. Utilizing this design the initial bolt hole probe shown in Figure 25 was fabricated to examine the 2.54 cm (1 inch) bolt hole specimen USAF 1 shown with the probe. Data were taken with the probe operating at 900 MHz. The data indicate three distinct flaw signals per revolution of the specimen. The two larger signals are the tight joints where the halves of the specimen fit together, while the third signal is a result of the EDM notch flaw in the specimen. The lower level noise is probably a result of the surface roughness of the specimen hole. Photos of these tight joints and the EDM

Initial Bolt Hole Probe

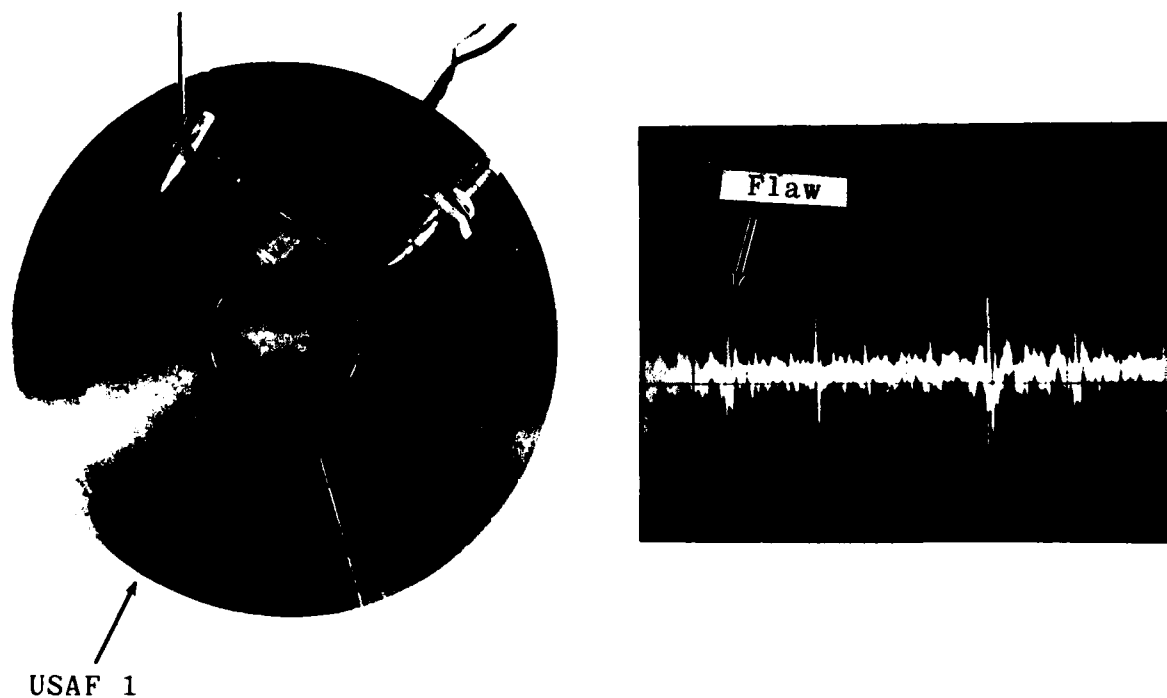
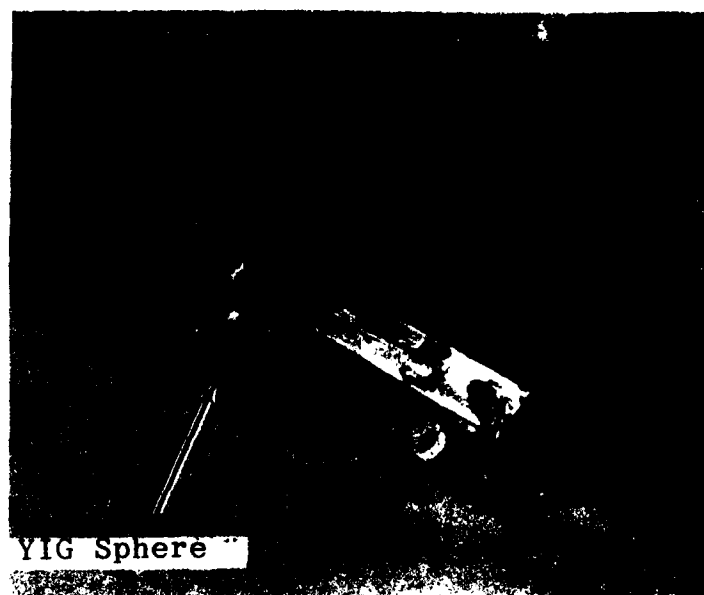


Figure 25. Initial Bolt Hole Probe with Bolt Hole Specimen (USAF 1) and Data.

notch in USAF 1 are shown in Appendix D. The electronic schematic for this probe is the same as that of the demonstration probe, which is detailed in Appendix G.

3.3.6 Demonstration Probe

The demonstration probe, shown in Figure 26, of which five copies were fabricated and evaluated, is designed to demonstrate the microwave design, probe fabrication and magnetic field techniques developed in this project. Details on probe construction are discussed in Appendix G. The multitude of data taken with the five probes are shown in Appendix E. Probably, the most about probe fabrication techniques was learned in this effort since the requirement was for five probes performance characteristics within 10% of each other. For instance, during the process of trying to match the sensitivities of five microwave FMR active probes, it was discovered that for a given operating frequency several YIG sphere

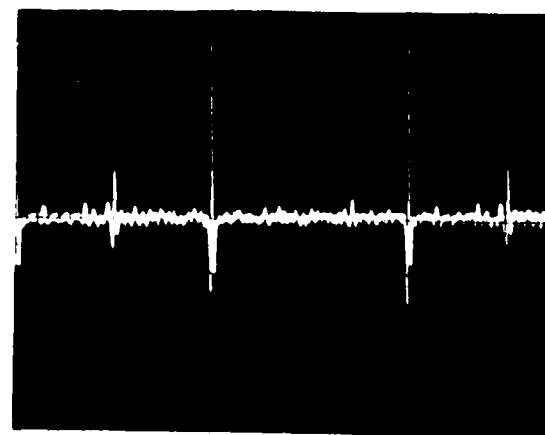


Demonstration Probe

6 5 4 3 2 1 6



Disk Data



Bolt Hole

Figure 26. Demonstration Probe with Typical Titanium Disk and Bolt Hole Responses.

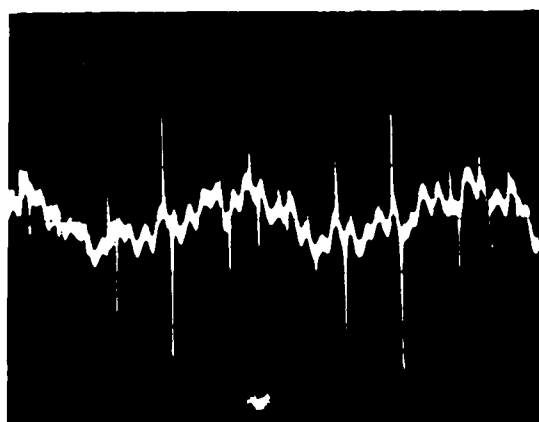
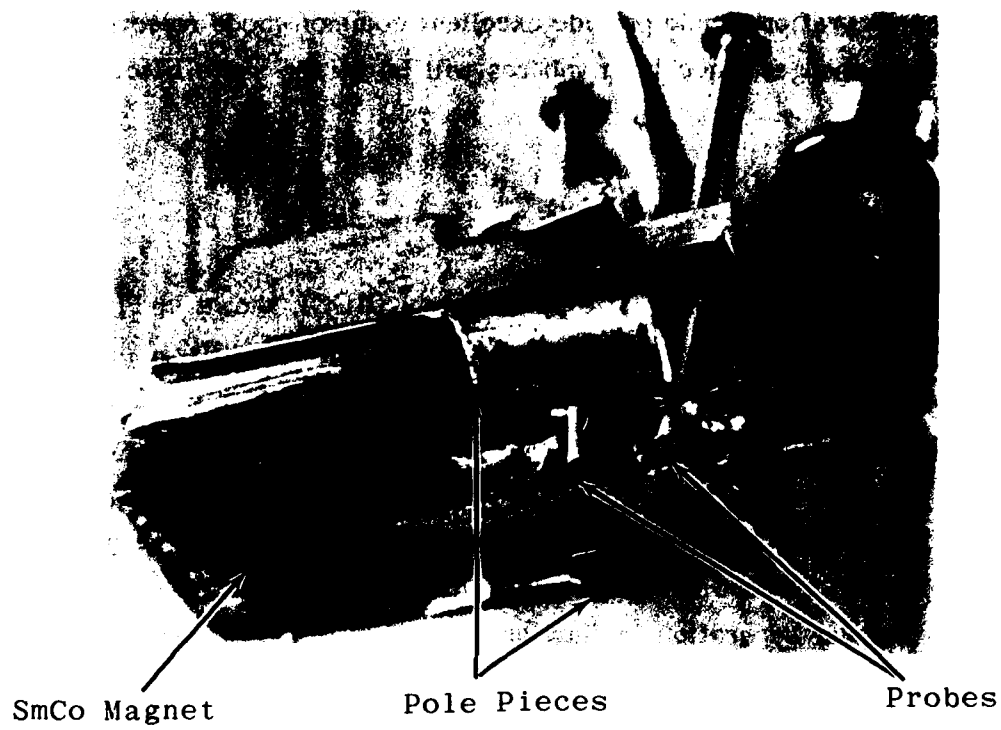
orientations could be found with sensitivity to a given flaw differing as much as six to one. That is, one orientation would give a 1-MHz shift in probe output frequency as a result of passing over EDM notch #6 on the titanium disk, while another would produce a 6-MHz shift. It was discovered that sensitivity was also a function of the distance separating the knife-edged pole pieces. These different sensitivities may be the result of slightly different magnetic field gradients in the sphere's volume in the different orientations. The five probes were setup for responses to notch #6 in the range of 2.0 to 2.8 MHz. Data shown in Figure 26 (as well as in Appendix E) were taken with demonstration probe #5 operating at 870 MHz. The response to #6 EDM notch for this probe is approximately 2.5 MHz. On the bolt hole specimen data the tight junction responses are approximately 1.2 MHz while the EDM notch response is 0.4 MHz. The liftoff response for this probe configuration is approximately 3 MHz per 0.025 mm (0.001 inch) of liftoff change around a typical static setting of 0.125 mm (0.005 inch). The relatively slow moving liftoff component in the probe output was filtered out by the HPF for the data shown.

3.3.7 Dual-Differential Probe

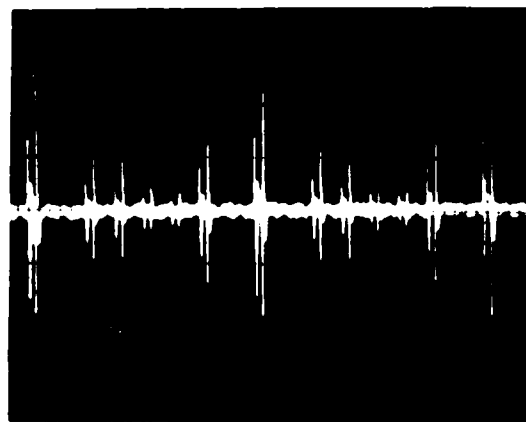
Utilizing our latest fabrication techniques, the dual-differential probe, shown in Figure 27, was fabricated and evaluated. It consists of two independent active FMR probes with the YIG spheres placed 5.5 mm (0.22 inch) apart in a magnetic field supplied by a single source. As in the demonstration probes, the spheres have been mounted on a screw/alumina-rod configuration to allow for easy adjustment of their orientation in the loop and flux field.

The data were taken with this dual probe positioned approximately 0.10 mm (0.004 inch) over our EDM notched titanium disk with the oscillator outputs connected to the R and L inputs of the signal processor mixer. This configuration produces differential data from the dual FMR probe.

The F/V output signal indicates an increase in peak to peak signal to noise ratio of approximately 2 over the single probe configuration. We feel that the lower frequency component of liftoff noise can be cancelled by more closely matching the YIG spheres crystallographic orientation in the loop and flux field along with



F/V Output



HPF Output

Figure 27. Dual-Differential Probe with Titanium Disk Data.

matching the probe liftoffs. The higher frequency component appears to be caused by probe wobble which can be minimized by placing the probes as close as possible together, such as 1.25 mm (0.050 inch) rather than 5.5 mm (0.226 inch) as with this probe. This configuration should provide excellent common-mode rejection of liftoff and temperature changes since both spheres will be at the same liftoff and in the same environment.

3.3.8 Q and F Data from Active Probe

The active probe with automatic gain control (AGC), shown in Figure 28, was designed to evaluate the theory developed by Stanford of flaw/liftoff discrimination from oscillator output frequency and spectral linewidth (Q). In this circuit the amplitude of the collector current is held constant by the AGC system which consequently provides amplitude information in the base bias voltage V_{AGC} . Putting the frequency (F/V output) and amplitude (V_{AGC}) signals into the vertical and horizontal inputs of a scope should provide an excellent means of developing and observing any angular separation in flaw and liftoff information available from the active probe if sufficient data can be detected.

However, while examining the EDM notched rotating disk, the AGC voltage did not produce any detectable fluctuations as long as the active probe was operating at a high Q with no additional spurs or resonant modes occurring. This condition did provide good frequency-based flaw data. When either the oscillator circuit or the YIG sphere were adjusted so that distortion was visible in the microwave output waveform along with spurs in its spectrum, the AGC voltage gave a very strong indication of liftoff. Flaw data were not detectable. However, these spurious oscillations produced an abundance of noise in the frequency data negating the probe's flaw detection ability. Even though this experiment did not produce satisfactory results, it is felt that improvements in the signal processing electronics could conceivably provide Q data with the oscillator operating in a high Q mode, thus providing flaw and liftoff data discrimination with a single active probe.

A brief examination of the actual amplitude of the oscillator output signal was performed with the probe looking at the EDM notches in the titanium disk. A

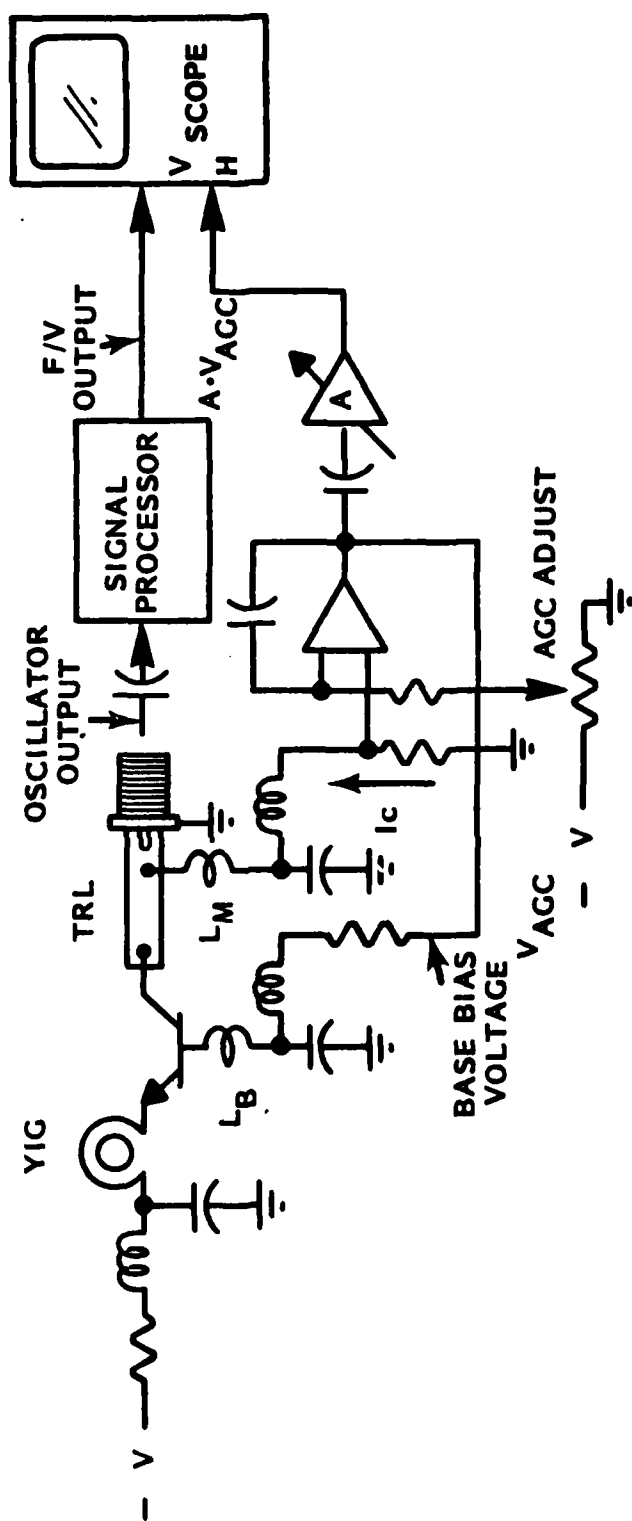


Figure 28. Active Probe with AGC.

microwave amplitude detector was used to provide the amplitude data while the active probe signal processor provided the frequency data. The amplitude and frequency data were observed to have similar responses to both EDM notches and changes in liftoff and therefore did not offer liftoff discrimination. It should be noted that the active probe output amplitude level is probably much more a function of the oscillator circuit component reactances, which change with frequency, than it is a function of the oscillator Q for the oscillator design used in this experiment.

4.0 SUMMARY AND CONCLUSIONS

4.1 Theoretical

In designing an eddy current probe for detecting small fatigue cracks it is important to maximize the ratio of the flaw signal to the liftoff signal. It has long been realized that the liftoff signal is large compared to the flaw signal, and detection systems currently in use maximize liftoff discrimination by detecting the component of the flaw signal in phase quadrature with the liftoff signal. Studies of liftoff in one dimensional probe models, performed by Stanford under the AF/DARPA program for QNDE, have shown that there always exists a residual contribution in the phase quadrature output due to liftoff phase variations proportional to the square of the fluctuations in liftoff distance. This second order liftoff signal varies as $(\text{frequency})^{1/2}$, and therefore has the same frequency dependence as the flaw signal for large ratios of flaw dimension to skin depth. This shows, at least for the one-dimensional model, that flaw-to-liftoff discrimination increases continuously with increasing frequency. Similar liftoff calculations have been presented in this report for a three-dimensional treatment of the FMR probe. Although it has not yet been found possible to analytically evaluate the second-order liftoff signal, the general form of the results suggests the same conclusion, namely, that flaw-to-liftoff discrimination is improved by increasing the operating frequency.

The analysis presented here covers the basic theoretical results needed for parameter optimization of practical FMR probes of both passive and active types. Detailed considerations have been given to one-sphere probes, but are in a form that can be extended to the two-sphere geometry. In the latter case, however, the liftoff effects may have to be evaluated numerically. Detailed optimization of probe parameters has not yet been performed, but general trends are easily noted from the inspection of the equations.

The following conclusions can be drawn:

(1) Equations (13) (or 15) and (B-19) show that the ratio of ΔZ_f to the first order ΔZ_{10} increases with decreasing sphere radius R_{sp} . This is to be expected from dimensional scaling, and although the second order ΔZ_{10} has not yet been completely evaluated, it is expected that this will also lead to improved signal-to-noise ratio with decreasing sphere radius.

(2) The first order ΔZ_{10} Eq. (B-19) has a dependence on the dc bias field angle θ similar to that obtained by numerical analysis of the lossless test sample.⁽¹⁵⁾ It can be seen that liftoff increases with θ , and is minimized with H_{dc} normal to the test piece surface. However, in this orientation electrical coupling to the ferromagnetic resonator, described by the $\sin^2\theta$ factor in Eq. (B-19), goes to zero. This means that ΔZ_f also vanishes at $\theta = 0$. An optimum arrangement would be to tilt the coupling coil as much as possible (Fig. 29) to allow the orientation of H_{dc} normal to the test piece surface. This is, of course, under the hypothesis that the angle dependence of second order ΔZ_{10} is similar to that of the first-order effect.

(3) The resonator quality factor Q appears in the ΔZ_f and ΔZ_{10} formulas through the bandwidth factor ΔH in Eq. (C-9). Reducing the bandwidth increases the magnetic field concentration H_x along the crack, giving a stronger flaw signal. A close examination of Equations (14) and (B-19) shows, however, that $(\Delta H)^{-2}$ appears as a common multiplying factor in both flaw and liftoff signals, leading to the conclusion that the resonator quality factor does not affect the signal-to-noise ratio of the probe. A high enough Q is of course necessary for frequency stability in active probes, and also in order for the flaw signal to be above the circuit noise level.

(4) There is an important restriction on the resonance frequency of the probe due to nonlinear effects in the YIG.⁽¹⁾ These effects limit the resonator response to very low amplitude levels at excitation frequencies below

$$f_{crit} = \gamma \frac{2(4\pi M_s)}{3} ,$$

where, $\gamma = 2.8\text{MHz/Oe}$. At the operating frequency of our probes ($f \approx 900\text{ MHz}$) the maximum usable saturation magnetization is $4\pi M_s \approx 480\text{ Oe}$. This requires gallium doping of the resonator spheres to reduce $4\pi M_s$ below the intrinsic value of 1750 Oe . Examination of Eqs. (14) and (B-19) shows that this does not affect the ratio of flaw and liftoff signals.

4.2 Experimental

Based on the theoretical work performed at Stanford, experiments were performed at Battelle to evaluate the FMR probe in both passive and active operating modes. Several microwave multifrequency techniques were evaluated on the passive probe. Conventional multifrequency-multiparameter techniques were utilized in attempts to generate flaw data independent of liftoff effects (i.e., liftoff discrimination). No combination of parameter mixing and drive frequencies was found that would provide liftoff discrimination with the passive probe acting alone.

A standard 200-kHz eddy current arrangement was then integrated with the passive probe system that provided fairly good suppression of liftoff effects on the passive probe. This arrangement could also be applied to the active probe although it does add bulk and complexity to the inspection system. In any case the experimental work with the passive probe was terminated in favor of developing the active probe, which we concluded offered a much more practical approach. This was based on the passive probe's overwhelming drawback as a field instrument, specifically its inability to provide flaw detection when driven outside of an extremely narrow band of frequencies which must correspond to the FMR probe's resonance. The practical aspect of this characteristic arises in the requirement placed on the microwave driving electronics in that its output frequency must be matched with the FMR probe resonance and held there against all effects tending to change it (liftoff, temperature, etc.), except for surface flaws. The active probe, which utilizes the FMR probe as the resonator in a microwave oscillator, circumvents this drawback since the active probe self-generates its own drive frequency directly at the FMR probe's resonance.

Several active probe designs were evaluated in the efforts to explore FMR probe theory experimentally as well as develop our demonstration probe. This not only involved microwave YIG oscillator design and fabrication but required the design of a magnetic field source to accommodate inspection of a bolt hole geometry. A microwave signal processor was designed and fabricated to perform the microwave frequency to voltage conversion on the active probe's output, and provide data for probe sensitivity evaluation. Most of the experiments performed on the active probes pertained to developing repeatable and simple fabrication techniques for obtaining consistent data.

A couple experiments were performed in attempts to detect Q as well as frequency data from the active probe. Theory generated at Stanford as well as experimental data from passive probes clearly shows that if Q -based information can be detected and processed with the frequency-based data, characterization of the probe response in terms of liftoff and flaw geometry is possible. However, we were unable to obtain a usable signal representative of the FMR probe's Q operated in the active arrangement.

A dual-differential FMR probe arrangement was also evaluated. Data were obtained with this dual probe which shows promise for the differential approach. However, limited time allowed only a cursory examination of its potential.

Five probes of a design that utilized and demonstrated many of the positive aspects of our experimental work were fabricated and evaluated. The evaluation demonstrated their repeatable flaw sensitivity along with the practical advantages of the active probe. The primary advantage lies in the simplicity of the signal processor. Secondly, with microcircuit techniques, it is possible that not only the probe circuitry but much of the signal processor electronics can be miniaturized and located close to the probe, such that the data in its microwave form would be converted to a form more suitable for transfer through conventional slip rings which might be part of a rotary scanning inspection system. The disadvantage of the active probe system relative to a passive-probe system is that the probe itself must contain some electronics (i.e., the microwave oscillator).

In conclusion, we feel that the microwave FMR eddy current probe has an excellent future in NDT especially where extremely small surface-connected flaws must be detected in locations of restricted geometries.

REFERENCES

1. Lax and Button, Microwave Ferrites and Ferrimagnetics, New York: McGraw-Hill, 1962.
2. B.A. Auld, "Theoretical Characterization and Comparison of Resonant Probe Microwave Eddy Current Testing with Low Frequency Eddy Current Methods," in Eddy Current Characterization of Materials and Structures, G. Birnbaum and G. Free, eds. Philadelphia: ASTM STP 722, 1981.
3. B.A. Auld and D.K. Winslow, "Microwave Eddy Current Experiments with Ferromagnetic Resonance Probes," *ibid*, pp. 348-366.
4. C.V. Dodd and W.E. Deeds, "Analytical Solutions to Eddy-Current Probe-Coil Problems," J. Appl. Phys. 39 2829-2838, 1968.
5. B.A. Auld, "Theory of Ferromagnetic Resonance Probes for Surface Cracks in Metals," Ginzton Laboratory Report No. 2839, July 1978.
6. B.A. Auld, F. Muennemann, and D.K. Winslow, "Eddy Current Probe Response to Open and Closed Surface Flaws," J. N.D.E. 2 1-21, 1981.
7. L. Strauss, Wave Generation and Shaping, New York: McGraw-Hill, 1970.
8. P.M. Ollivier, "Microwave YIG Tuned Transistor Amplifier Design: Application to C Band," IEEE J. Solid-State Circuits SC-7 54-60, Feb. 1972.
9. J.C. Papp and Y.Y. Koyano, "An 8-18 GHz Tuned FET Oscillator," IEEE Trans. MTT-28 762-767, 1980.
10. Ramo, Whinnery, and Van Duzer, Fields and Waves in Communication Electronics, New York: John Wiley and Sons Inc. 1965.

11. Alfredo Banos Jr., Dipole Radiation in the Presence of a Conducting Half Space, New York: Pergamon Press, 1966.
12. B.A. Auld and M. Riaziat, "Quantitative Modeling of Flaw Response in Eddy Current Testing," Ginzton Laboratory Report No. 3376, Dec. 1981.
13. J.A. Stratton, Electromagnetic Theory, New York: McGraw-Hill, 1941.
14. R.E. Collin, Foundations of Microwave Engineering, New York: McGraw-Hill, 1966.
15. J.M. Prince and B.A. Auld, "Research to Develop and Evaluate Advanced Eddy Current Sources for Detecting Small Flaws in Metallic Aerospace Components," Battelle Pacific Northwest Laboratories, Third Interim Technical Report, March 1982.
16. G.D. Vendelin, Design of Amplifiers and Oscillators by the S-Parameter Method, New York: John Wiley and Sons Inc., 1982.
17. T.J. Davis and B.A. Auld, "Research to Develop and Evaluate Advanced Eddy Current Sources for Detecting Small Flaws in Metallic Aerospace Components," Battelle, Pacific Northwest Laboratories, Second Interim Report, Sept. 1981.

APPENDIX A

First and Second Order Liftoff Effects

In this section, which reports studies performed under the Air Force / DARPA Program for QNDE, we will see how the ΔZ expression of Eq.(4) can be used to obtain an analytical expression for liftoff, in the form of a Taylor series expansion in powers of the liftoff variation l . To begin, we rewrite Eq.(4) in terms of the incident magnetic field spectrum,

$$\Delta Z_{lo} = \frac{1}{l^2} \int_{-\infty}^{+\infty} \int_{-\infty}^{+\infty} [Z'_s(k) - Z_s(k)][1 - \Gamma(k)][1 - \Gamma'(k)] h_i(k) \cdot h_i^*(-k) dk_x dk_y. \quad (A-1)$$

The fields are, of course, only the tangential components of the total incident fields, and are, therefore, two dimensional vectors. Next, we expand $Z'_s(k)$ and $\Gamma'(k)$ in powers of l ,

$$\begin{aligned} Z'_s(k) &= Z_s(k) + l \frac{\partial Z_s}{\partial l} + l^2 \frac{\partial^2 Z_s}{\partial l^2} + \dots, \\ \Gamma'(k) &= \Gamma(k) + l \frac{\partial \Gamma}{\partial l} + l^2 \frac{\partial^2 \Gamma}{\partial l^2} + \dots, \end{aligned} \quad (A-2)$$

where all the derivatives are evaluated at $l = 0$. Substituting Eq.(A-2) in Eq.(A-1) and keeping terms up to second order in l , we obtain,

$$\Delta Z_{lo} = \frac{1}{l^2} \int \int [1 - \Gamma(k)] \left\{ l \frac{\partial Z}{\partial l} (1 - \Gamma) + l^2 \left[\frac{\partial^2 Z}{\partial l^2} (1 - \Gamma) - \frac{\partial Z_s}{\partial l} \frac{\partial \Gamma}{\partial l} \right] \right\} h_i(k) \cdot h_i^*(-k) dk. \quad (A-3)$$

$\Gamma(k)$, $\frac{\partial \Gamma}{\partial l}$, $\frac{\partial Z_s}{\partial l}$, and $\frac{\partial^2 Z_s}{\partial l^2}$ are probe independent expressions that we proceed to evaluate next. The quantity Z_s is the surface impedance of a conducting half space below an air layer of thickness l (Fig.4). Standard transmission line theory gives the following relation¹⁰ for Z_s ,

$$Z_s(k, l) = \eta_A(k) \left[\frac{Z_s(k) \cos \kappa_A l + i \eta_A(k) \sin \kappa_A l}{\eta_A(k) \cos \kappa_A l + i Z_s(k) \sin \kappa_A l} \right]. \quad (A-4)$$

In this equation $Z_s(k)$ is the metallic surface impedance in the absence of the air layer, and $\eta_A(k)$ is the characteristic impedance of air given by, $\eta_A(k) = \omega \mu_0 / \kappa_A$, and $\kappa_A = \sqrt{\omega^2 \mu_0 \epsilon_0 - k^2}$. Also, since the metallic surface is a conductor, $Z_s(k) \approx i \omega \mu_0 \delta \cdot (2i + k^2 \delta^2)^{-1/2}$.

Let us digress for a moment to mention two simplifying approximations that can be made at this point. First is the quasistatic approximation in air which allows us to let k

become zero in this medium¹¹. This is a well justified approximation for frequencies of operation as high as several gigahertz, due to the fact that the electromagnetic wavelength in air (30 cm. at 1.0 GHz) is much larger than any characteristic dimension of the problem. The second assumption is based on the fact that the YIG sphere may be thought of as a rotating dipole no closer to the surface it is probing than the radius of the sphere. As will be seen later, the spectrum of the dipole field (and most other practical probe fields) has an exponentially decaying factor e^{-kz_0} , where z_0 is the liftoff distance. This leads to a factor e^{-2kz_0} in the liftoff integral, putting an upper limit on the contributing values of k . A reasonable value for this upper limit is obtained by requiring that the exponential factor be larger than e^{-10} or, $kz_0 < 5.0$. Normalizing with respect to the skin depth, $(k\delta)\frac{z_0}{\delta} < 5$. But $z_0 = R_{sp} > 0.25\text{mm.}$, and δ is only a few microns for a good conductor at 1.0 GHz. We see that z_0/δ is much larger than one, and, therefore, throughout our discussion we can assume that $k\delta \ll 1$, and neglect terms including second and higher powers of $k\delta$.

Making use of the above assumptions and explicitly differentiating Eq.(A-4) with respect to l we find,

$$\begin{aligned}\frac{\partial Z_s}{\partial l} \Big|_{l=0} &= \frac{-2\omega\mu_0}{2i + k^2\delta^2} \approx i\omega\mu_0, \\ \frac{\partial^2 Z_s}{\partial l^2} \Big|_{l=0} &= -(1+i)\omega\mu_0 k^2\delta.\end{aligned}\tag{A-5}$$

Similarly, since the reflection coefficient is defined as $\Gamma = \frac{Z_s(k,l) - \eta_A}{Z_s(k,l) + \eta_A}$,

$$\begin{aligned}\Gamma(k) &= -1 + k\delta(1-i), \\ \frac{\partial \Gamma}{\partial l} \Big|_{l=0} &= 2k[-1 + k\delta(1-i)].\end{aligned}\tag{A-6}$$

Now, we see that Eq.(A-3) may be simplified to,

$$\Delta Z_{l_0} = 4i\omega\mu_0 \int_{-\infty}^{+\infty} \int_{-\infty}^{+\infty} [1 + (i-1)k\delta] \left[l - l^2 k + \frac{3}{2} l^2 k(1-i)k\delta \right] \mathbf{h}_i(\mathbf{k}) \cdot \mathbf{h}_i^*(-\mathbf{k}) d\mathbf{k}_x d\mathbf{k}_y.\tag{A-7}$$

Let us take the incident field to have the following simple one dimensional spectrum,

$$h_i(k_x) = \frac{1}{2} e^{-|k_x|z_0},$$

representing a one dimensional probe in the form of a single straight wire¹². The integration can be done analytically in this case, giving

$$\Delta Z_{l_0} = i\omega\mu_0 \left[\frac{l}{z_0} \left(1 - \frac{1-i}{2} \frac{\delta}{z_0} \right) - \frac{l^2}{2z_0^2} \left(1 - 5 \frac{1-i}{2} \frac{\delta}{z_0} \right) \right].\tag{A-8}$$

We see that the second order expression has a different phase angle than the first order liftoff, and, therefore, contributes to liftoff in the perpendicular channel. Even before specifying the incident field spectrum for any particular probe, it is expected from the form of Eq.(B-7) that the second order liftoff will contain a term with a $(1-i)$ factor which will not be in phase with the first order liftoff.

APPENDIX B

Liftoff Calculations for the FMR Probe

As will be shown in Appendix C, the FMR probe operating a short distance from a conducting plane can be represented by vertical and horizontal dipoles whose strengths are given by Equations (C-9) and (C-10). In order to be able to calculate liftoff through the use of Equation (4), we need to find the Fourier transform of the probe field, which, in this case reduces to the determination of field spectra generated by horizontal and vertical dipoles. We will take two approaches to this problem. One is through the quasistatic approximation which allows us to make use of the magnetostatic potential. The other is through the utilization of the magnetic Hertz vector which is more general, but as we will see, reduces to the same results in the proper limit.

(i) Quasistatic Approach

The magnetostatic potential of a magnetic dipole \mathbf{m} , is given by¹³,

$$\Phi = \frac{\mathbf{m} \cdot \mathbf{R}}{4\pi R^3}, \quad (B-1)$$

where, R is the radial distance from the dipole in spherical coordinates (Fig.B-1). On the surface of the metal \mathbf{R} may be written as, $\mathbf{R} = -z_0\hat{z} + \mathbf{r}$. For a vertical dipole, $\mathbf{m} = m_z\hat{z}$, and $\mathbf{m} \cdot \mathbf{R} = -z_0 m_z$. The magnetic potential at the surface is thus found to be,

$$\Phi(r) = -\frac{m_z z_0}{4\pi(r^2 + z_0^2)^{3/2}}. \quad (B-2)$$

The magnetostatic field is the negative gradient of the potential, $\mathbf{H} = -\nabla\Phi$. The incident magnetic field component tangential to the surface is the two-dimensional gradient of the potential, $\mathbf{H}_i = -\nabla_{x,y}(\Phi)$. In the Fourier domain as defined by Equation (3), the same relation is expressed as, $\mathbf{h}_i(\mathbf{k}) = -i\mathbf{k}\phi(k)$, where $\phi(k)$ is the transform of $\Phi(r)$. This transform is easiest to evaluate in polar coordinates using Hankel transforms (inverse of Equations (5)).

$$\begin{aligned} \phi(k) &= -\frac{m_z z_0}{4\pi} \int_0^\infty (r^2 + z_0^2)^{-3/2} J_0(kr) r dr \\ &= -\frac{m_z z_0}{4\pi} \frac{e^{-kz_0}}{z_0}. \end{aligned} \quad (B-3)$$

This yields a simple expression for $h_i(k)$,

$$h_i(k) = ik \frac{m_z}{4\pi} e^{-kz_0}. \quad (B-4)$$

For the horizontal dipole we follow the same procedure. Taking the dipole to point in the x direction, $\mathbf{m} = m_x \hat{x}$,

$$\Phi(r) = \frac{m_x}{4\pi} \frac{r \cos \theta}{(r^2 + z_0^2)^{3/2}}. \quad (B-5)$$

After taking the Fourier transform of the potential and multiplying by $-ik$, an expression for the magnetic field spectrum is obtained,

$$h_i(k) = -k \frac{m_x}{4\pi} e^{-kz_0} \cos \alpha, \quad (B-6)$$

where $\tan \alpha$ is defined as the ratio of k_y to k_x . Expressions (B-4) and (B-6) will be used in the ΔZ integral to evaluate liftoff, but first we will briefly mention a more general method to derive and check these same expressions.

(ii) Polarization Potential Approach

In order to calculate electromagnetic fields whose sources are magnetic polarizations, it is convenient to use the magnetic polarization potential or the magnetic Hertz vector $\mathbf{\Pi}$. The Hertz vector is related to the driving magnetic moment through¹³,

$$\nabla^2 \mathbf{\Pi} - \mu_0 \epsilon \frac{\partial^2 \mathbf{\Pi}}{\partial t^2} = -\mathbf{M}, \quad (B-7)$$

where \mathbf{M} is the magnetic dipole moment density. The magnetic field may be expressed in terms of the Hertz vector as,

$$\mathbf{H} = \nabla \nabla \cdot \mathbf{\Pi} + \omega^2 \mu \epsilon \mathbf{\Pi}. \quad (B-8)$$

We define the two dimensional Fourier transform of $\mathbf{\Pi}(\mathbf{r})$ as $\mathbf{T}(\mathbf{k}, z)$. In the Fourier domain Eq. (B-8) becomes,

$$\mathbf{h}(\mathbf{k}, z) = \mathbf{k}(-\mathbf{k} \cdot \mathbf{T} + i \frac{\partial T_z}{\partial z}) + \hat{z}(i\mathbf{k} \cdot \mathbf{T} + \frac{\partial T_z}{\partial z}) + \omega^2 \mu_0 \epsilon_0 \mathbf{T}. \quad (B-9)$$

An important point that can be seen explicitly in Eq. (B-9) is that in the quasistatic limit, as $\omega^2 \mu_0 \epsilon_0$ approaches zero, the magnetic field of each Fourier component lies entirely in the (\mathbf{k}, \hat{z}) plane, or the plane of incidence of the wave. This means that each plane wave, represented by a value of \mathbf{k} , is polarized with the electric field perpendicular to the plane of

incidence, therefore justifying the perpendicular polarization assumption used in deriving Eq. (4).

The component of $h(\mathbf{k}, z)$ tangential to the conducting plane and evaluated at $z = -z_0$ is what is used in the evaluation of ΔZ_{lo} , and is found from Eq. (B-9) to be,

$$h_t(\mathbf{k}) = \mathbf{k}(-\mathbf{k} \cdot \mathbf{T} + i \frac{\partial T_z}{\partial z}). \quad (B-10)$$

The differential equation (B-7) with proper boundary conditions applicable to the problem at hand has been solved in Reference (11), with the Hertz vector represented in terms of plane wave components \mathbf{T} . For a vertical dipole, \mathbf{T} is given as,

$$\mathbf{T} = \hat{z} \frac{m_z}{\pi} \frac{2}{i\kappa_a + i\kappa_m} e^{-i\kappa_a z_0}, \quad (B-11)$$

κ_a and κ_m being the z direction propagation constants in air and metal respectively. Upon substitution of this in Eq. (B-10), taking the quasistatic limit, and simplifying the results, we obtain,

$$h_t(\mathbf{k}) = i\mathbf{k} \frac{m_z}{4\pi} (1 - \Gamma) e^{-kz_0}. \quad (B-12)$$

In the case of a horizontal dipole, \mathbf{T} has two components, $\mathbf{T} = \hat{x}T_x + \hat{z}T_z$,

$$\begin{aligned} T_x &= \left(\frac{m_x}{4\pi}\right) \frac{-2i\sigma}{-i\sigma\kappa_a + \omega\epsilon_0\kappa_m} e^{-i\kappa_a z_0}, \\ T_z &= \left(\frac{m_x}{4\pi}\right) \left(\frac{ik_x}{\omega\mu_0}\right) \frac{-2(\kappa_m - \kappa_a)}{i\sigma\kappa_a + \omega\mu_0\kappa_m} e^{-i\kappa_a z_0}. \end{aligned} \quad (B-13)$$

These expressions combined with Eq. (B-10) yield the tangential field spectrum for the horizontal dipole,

$$h_t(\mathbf{k}) = -\mathbf{k} \frac{m_x}{4\pi} (1 - \Gamma) e^{-kz_0} k_x. \quad (B-14)$$

Equations (B-12) and (B-14) give the total tangential fields on the surface, and when compared with Eq. (B-4) and Eq. (B-6) confirm the results obtained using the magnetic scalar potential.

(iii) Details of the Liftoff Calculation

Now, we are in a position to calculate the first order liftoff for the FMR probe. For this purpose, we write Eq. (4) in polar coordinates,

$$\Delta Z_{lo} = -\frac{1}{I^2} \int_0^\infty \int_0^{2\pi} \delta Z_s^\perp(k) h_t(\mathbf{k}) \cdot h_t^*(-\mathbf{k}) k dk d\alpha. \quad (B-15)$$

\mathbf{h} and \mathbf{h}' are of course equal to first order in l , and with the expressions derived for vertical and horizontal dipole fields, we can evaluate them for any orientation of the dipole. If the magnetic dipole is represented by, $\mathbf{m} = m_x \hat{x} m_y \hat{y} + m_z \hat{z}$, where in a rotating dipole the components can be out of phase, the resulting spectrum will be,

$$h_t(\mathbf{k}) = \hat{k} \frac{1-\Gamma}{4\pi} e^{-kz_0} [km_z - k_x m_x - k_y m_y]. \quad (B-16)$$

Here, $k_x = k \cos \alpha$, $k_y = k \sin \alpha$, and all other terms are independent of α . Also,

$$h_t(\mathbf{k}) \cdot h_t^*(-\mathbf{k}) = \left(\frac{1-\Gamma}{4\pi} \right)^2 e^{-2kz_0} [km_z - k_x m_x - k_y m_y] [km_z^* + k_x m_x^* + k_y m_y^*]. \quad (B-17)$$

In Eq. (B-15), in the integration over α , all terms not involving square magnitudes will vanish, and the resulting expression from combining Eq. (B-17) with Eq. (B-15) is,

$$\Delta Z_{lo} = l \frac{3i\omega\mu_0}{32z_0^4\pi I^2} [-2|m_z|^2 + |m_x|^2 + |m_y|^2] [1 + 2(i-1)\frac{\delta}{z_0}], \quad (B-18)$$

where, making the same approximations made in Appendix A, we have used,

$$(1-\Gamma)^2 \delta Z_s^\perp(k) = 4i\omega\mu_0 - 8k(1+i)/\sigma\delta$$

. Next, we substitute the magnetization values for the FMR probe into Eq. (B-18). These values have been derived in Appendix C, and presented in Eq. (C-9). The final result for first order liftoff in the FMR probe is,

$$\Delta Z_{lo} = i\omega\mu_0 l \left(\frac{3}{16\pi} \right)^3 \left(\frac{M_s \sin \theta}{\Delta H} \right)^2 \left[\frac{12 + (12 + \chi_s)(1 + \sin^2 \theta)}{24 + \chi_s(1 + \sin^2 \theta)} \right] [1 + 2(i-1)\frac{\delta}{z_0}], \quad (B-19)$$

where, $z_0 = \text{liftoff} = R_{sp}$. Note that the phase angle of this first order liftoff is independent of the dc field orientation θ .

Second order liftoff noise can also be calculated for the FMR probe using Eq.(A-7), with the incident field given by Eq. (B-16), but with the reflected component omitted,

$$h_i(\mathbf{k}) = \hat{k} \frac{1}{4\pi} e^{-kz_0} [km_z - k_x m_x - k_y m_y]. \quad (B-20)$$

The integral obtained with this substitution, however, may have to be evaluated numerically.

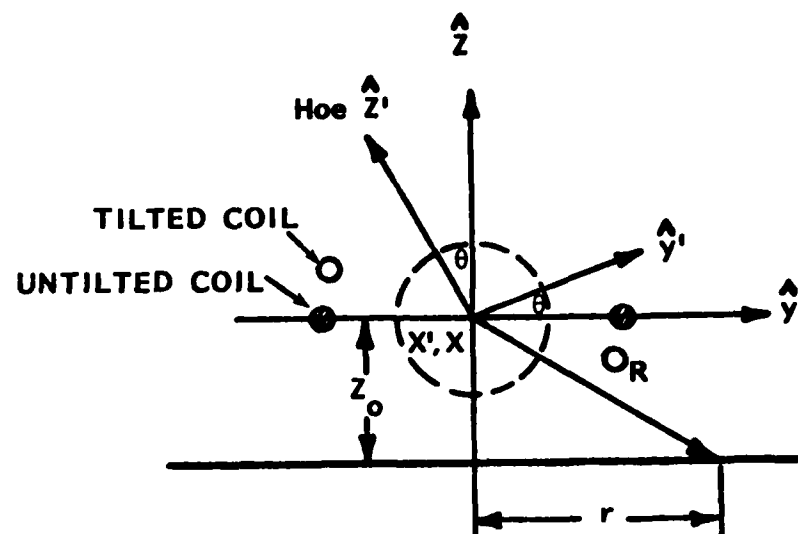


Figure B-1. The rf Field is Perpendicular to the Plane of the Excitation Coil. For the untilted coil the coupling goes to zero when θ is zero, but does not for the tilted coil.

APPENDIX C

The Effect of a Conducting Plane on the Uniform Precession Mode of a Spherical Resonator

In the absence of a conducting plane, the magnetization vector of a saturated YIG sphere, undergoes a circular precession about the dc magnetic field. In this section we will show that the presence of a neighboring conducting plane not only will shift the resonance frequency of the oscillator, but also, the precession of the magnetization about H_{dc} will change from circular to elliptical.

Initially we will take the plane to be a perfect conductor. The results, however, will be modified at the end to incorporate the effects of conductivity losses in the plane. Our approach to this problem is based on finding the rf magnetic field at the source created by an image resonator. This will be added to the driving rf field, and the resulting precession will be calculated.

Let us define the z' direction as that of the dc magnetic field: $\mathbf{H}_{dc} = H_{dc}\hat{z}'$ (Fig. C-1). The rf magnetic field \mathbf{H} , makes an angle θ with the z' direction. The primed axes refer to the resonator, while the unprimed axes are fixed with respect to the conducting plane surface located at $z = -z_0$. We represent the precessing magnetization of the sphere as a rotating magnetic dipole located at the origin,

$$\mathbf{m} = m_{x'}\hat{x}' + m_{y'}\hat{y}' = m_{x'}\hat{x} + m_{y'}\cos\theta\hat{y} + m_{y'}\sin\theta\hat{z}. \quad (C-1)$$

The image of this dipole is located at $z = -2z_0$:

$$\mathbf{m}_i = m_{x'}\hat{x} + m_{y'}\cos\theta\hat{y} - m_{y'}\sin\theta\hat{z}. \quad (C-2)$$

and the magnetostatic potential of a dipole is given by¹³

$$\phi = \frac{\mathbf{m} \cdot \mathbf{r}}{4\pi r^3}, \quad (C-3)$$

from which the magnetic field is calculated: $\mathbf{H} = -\nabla\phi$. Using these relations we then calculate the magnetic field due to the image dipole, at the origin. The total rf magnetic field acting on the resonator is the sum of this field and the driving rf field, $\mathbf{H} = H\hat{z}$.

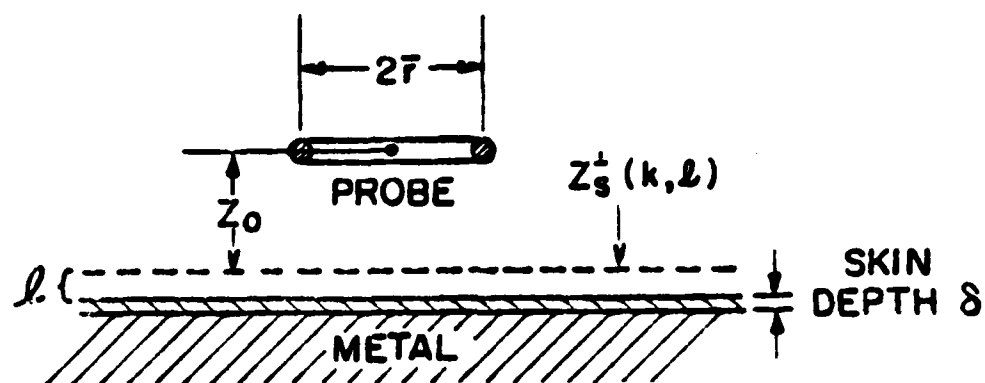


Figure C-1. Formulation of Lift-off in Terms of a Surface Impedance Change.

$$\mathbf{H} = -\frac{m'_x}{32\pi z_0^3}\hat{x} - \frac{m'_y \cos \theta}{32\pi z_0^3}\hat{y} + \left(H - \frac{2m'_y \sin \theta}{32\pi z_0^3}\right)\hat{z}. \quad (C-4)$$

This is the total external rf field applied to the sphere. To calculate the magnetic field inside the resonator, we need to subtract a demagnetizing factor. At the center of the sphere, $\mathbf{H}_{internal} = \mathbf{H}_{external} - \frac{1}{3}\mathbf{M}$, where $\mathbf{M} = \mathbf{m}/V_{sp}$, and V_{sp} is the volume of the sphere, $V_{sp} = \frac{4}{3}\pi R_{sp}^3$. The component of the rf magnetic field parallel to the dc field has no effect on the precession, because the magnetization is already saturated in that direction. The components perpendicular to H_{dc} are $(H'_{x'})_{int}$ and $(H'_{y'})_{int}$, which are found to be,

$$\begin{aligned} (H'_{x'})_{int} &= -\frac{m_{x'}}{4\pi} \left(\frac{1}{8z_0^3} + \frac{1}{R_{sp}^3} \right), \\ (H'_{y'})_{int} &= H \sin \theta - \frac{m_{y'}}{4\pi} \left(\frac{1 + \sin^2 \theta}{8z_0^3} + \frac{1}{R_{sp}^3} \right). \end{aligned} \quad (C-5)$$

So far we have not specified what $m_{x'}$ and $m_{y'}$ are, but we have derived the rf fields in terms of these quantities. Now we need to use the equations of motion of magnetization to find $m_{x'}$ and $m_{y'}$. For given applied magnetic fields, R.E. Collin¹⁴ states these equations as,

$$\begin{aligned} i\omega m_{x'} + \omega_0 m_{y'} &= \gamma m_s \mu_0 (H'_{y'})_{int}, \\ i\omega m_{y'} - \omega_0 m_{x'} &= -\gamma m_s \mu_0 (H'_{x'})_{int}. \end{aligned} \quad (C-6)$$

Here, $\omega_0 = \gamma \mu_0 H_0$ is the unperturbed resonant frequency, and m_s is the total saturation dipole moment of the sphere. Substituting equation 5 in 6 and solving for $m_{x'}$ and $m_{y'}$ we find,

$$\begin{aligned} m_{x'} &= i \frac{\omega \omega_{sp}}{\omega'^2_r - \omega^2} R_{sp}^3 H \sin \theta, \\ m_{y'} &= \frac{\omega_{rx'} \omega_{sp}}{\omega'^2_r - \omega^2} R_{sp}^3 H \sin \theta. \end{aligned} \quad (C-7)$$

In these equations, ω'_r is the new resonant frequency, given by $(\omega'_r)^2 = \omega_{rx'} \omega_{ry'}$. Following is a list of other definitions used,

$$\begin{aligned} \omega_{rx'} &= \omega_0 + K_{x'} \omega_{sp}, \\ \omega_{ry'} &= \omega_0 + K_{y'}(\theta) \omega_{sp}, \\ \omega_{sp} &= \gamma m_s \mu_0 / R_{sp}^3 = (3/4\pi) \gamma \mu_0 M_s, \\ K_{x'} &= [1/(2z_{0n})^3 + 1]/4\pi, \\ K_{y'}(\theta) &= [(1 + \sin^2 \theta)/(2z_{0n})^3 + 1]/4\pi, \\ z_{0n} &= z_0 / R_{sp} = \text{normalized lift-off}. \end{aligned}$$

Note that $m_{x'}$ and $m_{y'}$ are 90 degrees out of phase, but have different magnitudes characterizing the elliptical precession of the magnetization vector, as stated earlier.

Next, in order to account for conductivity losses in the plane and hysteresis losses in the sphere itself, we allow the resonance frequency ω'_r to become complex, and substitute, $\omega'_r + i\Delta\omega$, where $\Delta\omega \ll \omega'_r$. Then, if we also assume that the probe is operating at resonance, $\omega = \omega'_r$, we obtain the simplified results,

$$\begin{aligned} m_{x'} &= \frac{\omega_{sp}}{2\Delta\omega} R_{sp}^3 H \sin \theta, \\ m_{y'} &= \frac{\omega_{rx'} \omega_{sp}}{2i\omega \Delta\omega} R_{sp}^3 H \sin \theta. \end{aligned} \quad (C-8)$$

Defining $\chi_s = M_s/H_{oe}$, and $\Delta\omega = \gamma\mu_0\Delta H$, the same results may be put in the alternate form,

$$\begin{aligned} m_{x'} &= \frac{m_s}{2} \frac{H}{\Delta H} \sin \theta, \\ m_{y'} &= -i \left[\frac{24z_{0n}^3 + \chi_s}{24z_{0n}^3 + \chi_s(1 + \sin^2 \theta)} \right]^{1/2} m_{x'}. \end{aligned} \quad (C-9)$$

Finally, for the practical case of $\sin \theta = 1$ and $z_{0n} = 1$,

$$\begin{aligned} m_{x'} &= \frac{m_s}{2} \frac{H}{\Delta H}, \\ m_{y'} &= -i \left[\frac{24 + \chi_s}{24 + 2\chi_s} \right]^{1/2} m_{x'}. \end{aligned} \quad (C-10)$$

APPENDIX D

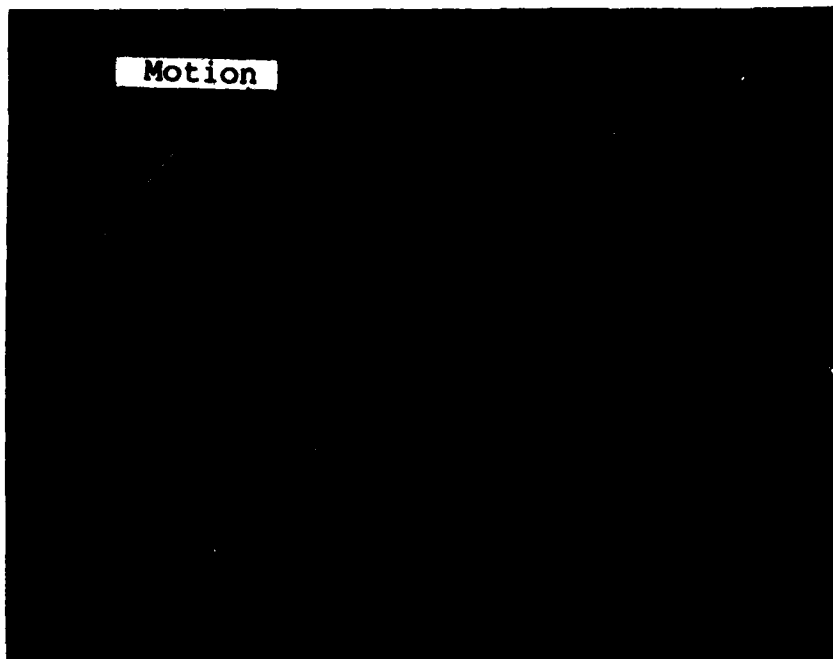
Magnified EDM Notches and Tight Cracks

Three specimens with electrodischarge-machined (EDM) notches of various sizes and tight cracks were examined during the series of probe evaluations.

The first specimen examined was the titanium disk-shaped piece which has six EDM notches in it. Photographs of the six notches magnified 100X are shown in Figure D-1. The notch depths listed in Figure 17 are the depths specified when the notches were made. They are approximate at best. However, we feel that with the depth of penetration in the order of 0.020 mm (0.0008 inch) in titanium at 900 MHz, the probe will not detect depth information in notch depths in the range of 0.13 mm to 0.25 mm (0.005 to 0.010 inch) where these notches were specified.

The aluminum tight fatigue crack is shown in Figure D-2 magnified 250X. This photograph shows a 0.44 mm (0.0176 inch) section of the 5 mm (0.2 inch) long tight crack that was examined with our initial 900 MHz active probe.

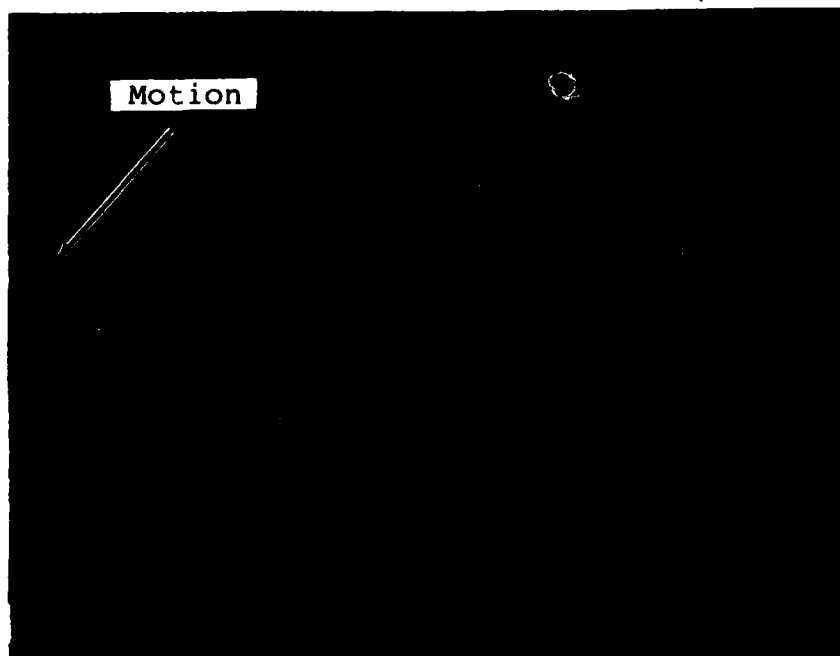
The titanium bolt hole specimen (USAF 1), shown in Figure D-3, was utilized to evaluate our demonstration probe design. It is shown with marks on it to relate the probe's responses with the EDM notch and junction cracks in the specimen. It is also shown on the test apparatus where rotation is in the counter-clockwise direction.



Scale:
0.010mm/div
(.0004 inch)

100X

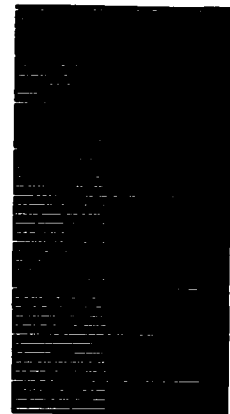
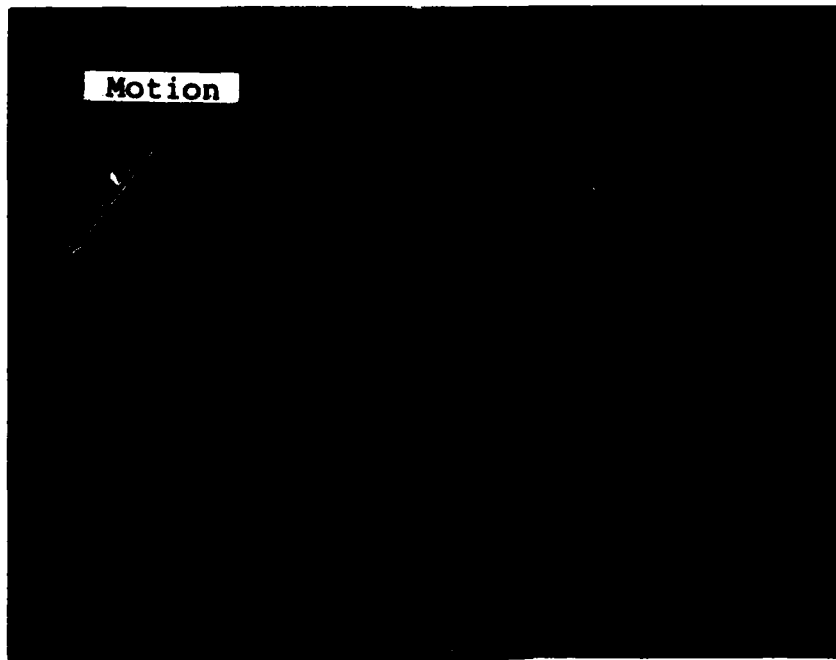
(a) EDM Notch 1: Length = 0.36 mm (.0144 inch)
Width = 0.36 mm (.0144 inch)



100X

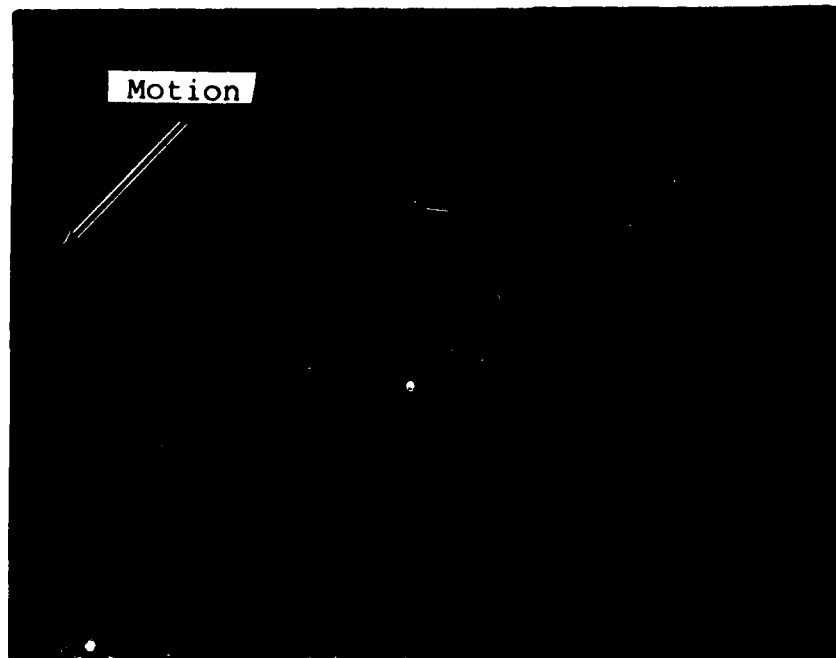
(b) EDM Notch 2: Length = 0.22 mm (0.0088 inch)
Width = 0.115 mm (0.0046 inch)

Figure D-1. EDM Notches in Titanium Disk (100X)



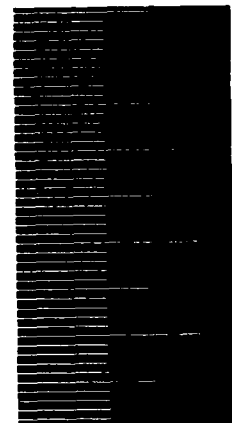
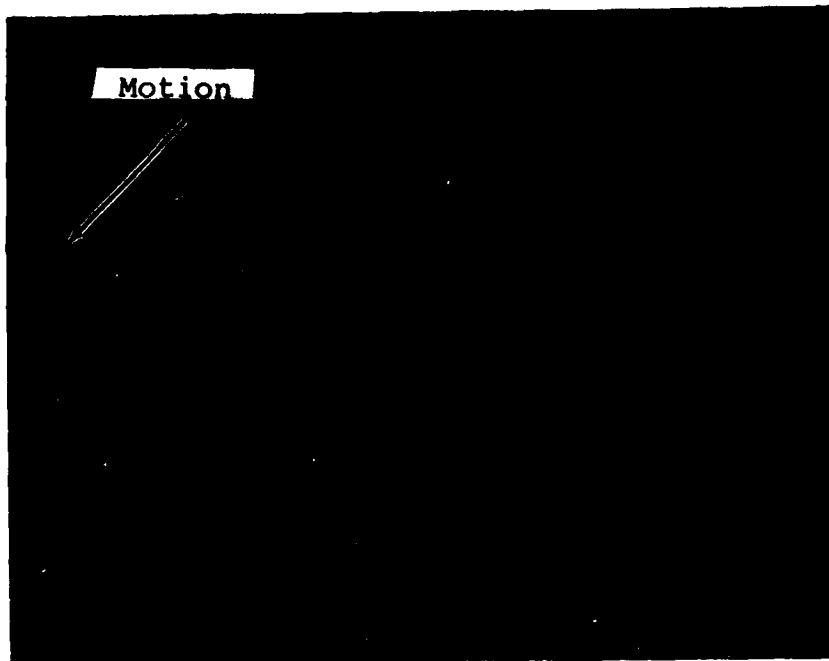
Scale:
0.010mm/div
(.0004 inch)

100X
(c) EDM Notch 3: Length = 0.24 mm (0.0096 inch)
Width = 0.13 mm (0.0052 inch)



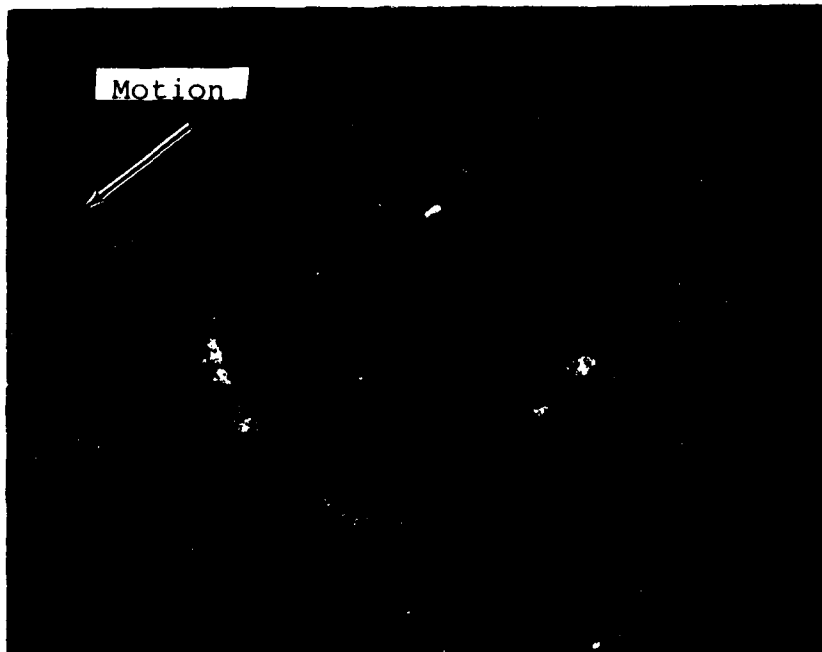
100X
(d) EDM Notch 4: Length = 0.42 mm (0.0168 inch)
Width = 0.14 mm (0.0056 inch)

Figure D-1 (cont'd)



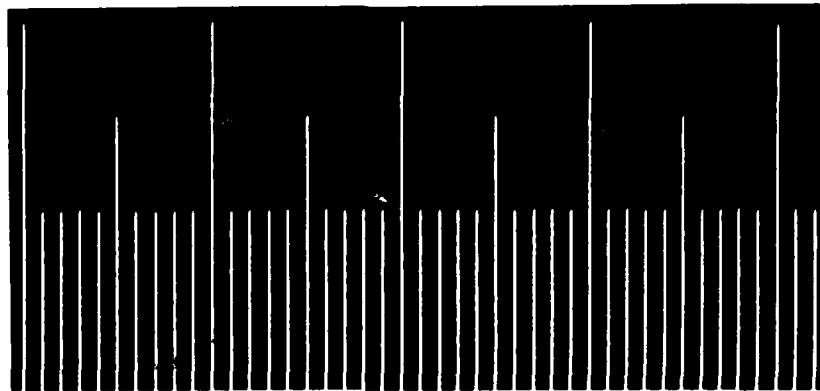
Scale:
0.010mm/div
(.0004 inch)

100X
(e) EDM Notch 5: Length = 0.43 mm (0.0172 inch)
Width = 0.14 mm (0.0056 inch)



100X
(f) EDM Notch 6: Length = 0.48 mm (0.0192 inch)
Width = 0.30 mm (0.012 inch)

Figure D-1 (cont'd)

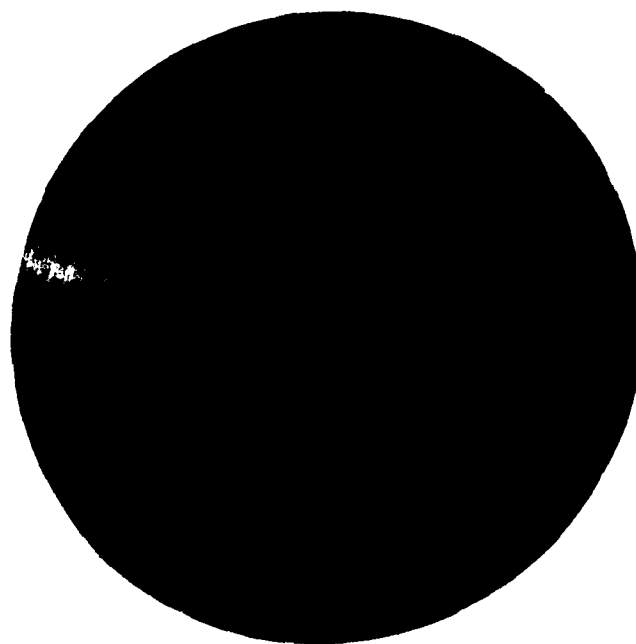


Scale: 0.010 mm/div
(0.0004 inch)



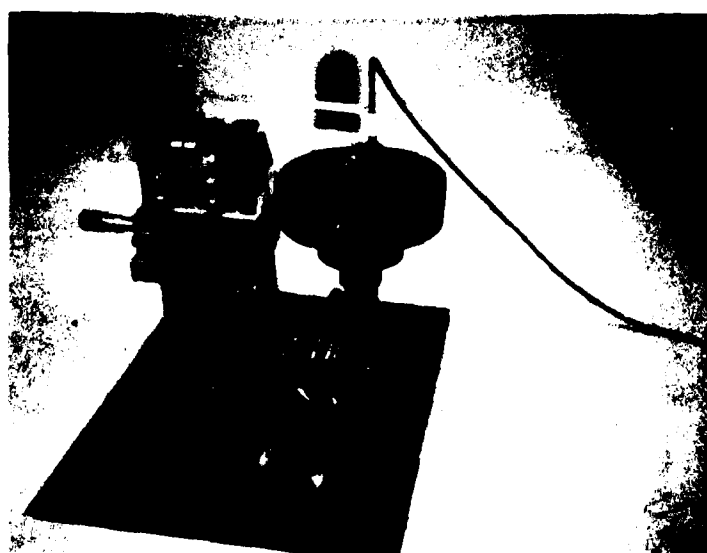
250X
Width = 0.003 mm (0.0001 inch)

Figure D-2. Tight Fatigue Crack in Aluminum (250X)



Motion

a. Top View of Bolt Hole Specimen



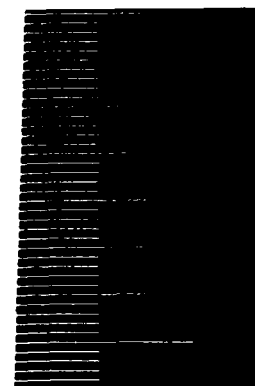
b. Bolt Hole Specimen on Test Apparatus

Figure D-3. Titanium Bolt Hole Specimen (USAF 1)

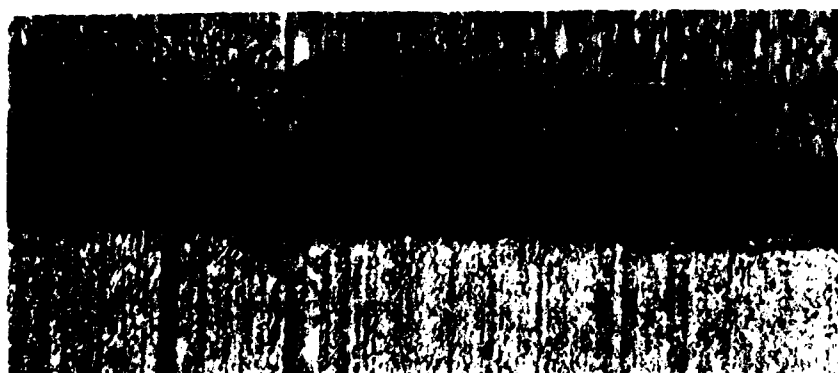


100X

c. EDM Notch: Length = 0.31 mm (0.0124 inch)
Width = 0.12 mm (0.0048 inch)

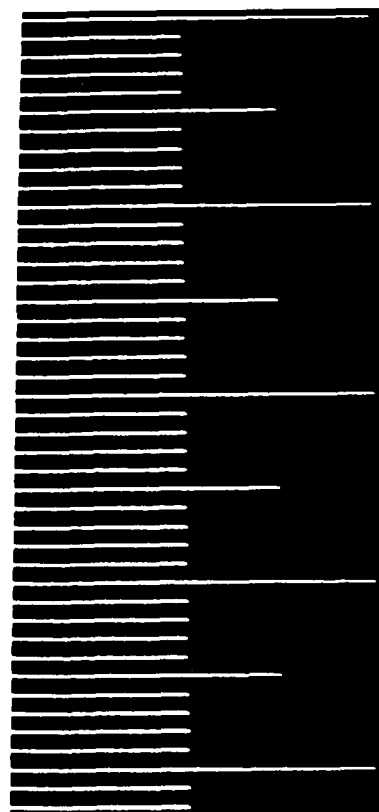


Scale:
0.010mm/div
(0.0004 inch)



250X

d. Junction Crack (-): Width = 0.04 mm
(0.0016 inch)



Scale:
0.010mm/div
(0.0004 inch)



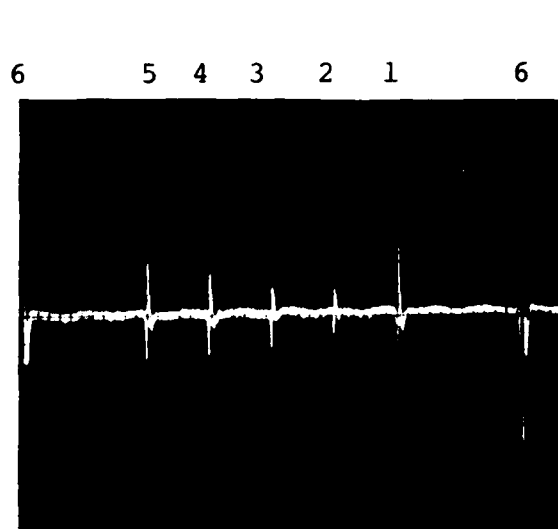
e. Junction Crack (X): Width = 0.020 mm
(0.0008 inch)

Figure D-3 (cont'd)

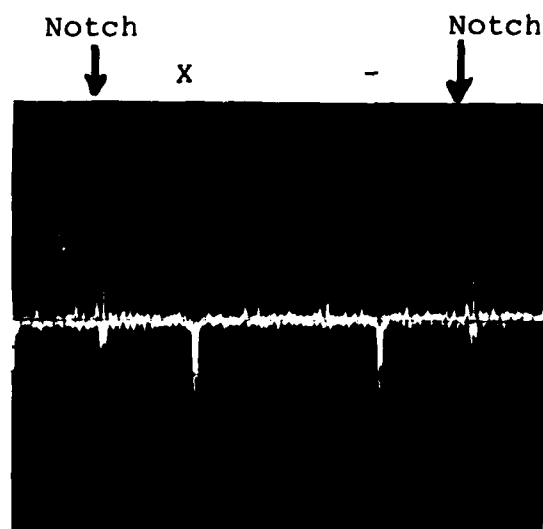
APPENDIX E

Demonstration Probe Data

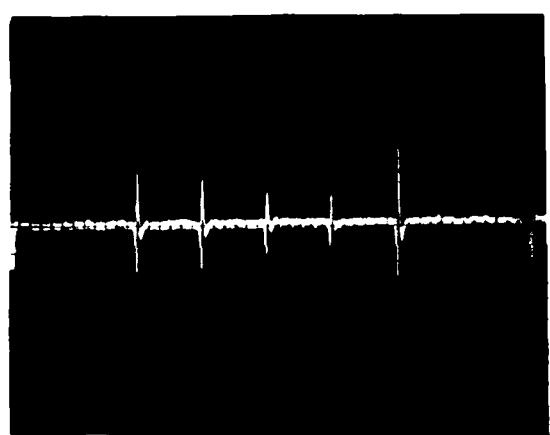
The data shown in Figure E-1 illustrate the repeatability of the demonstration probe's sensitivity. These data were taken with the probes operating at approximately 870 MHz with a liftoff of approximately 0.13 mm (0.005 inch).



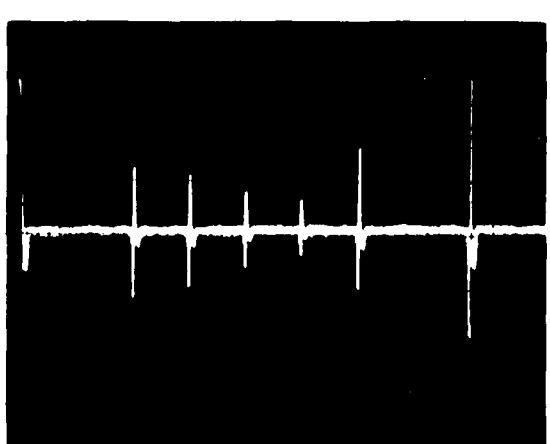
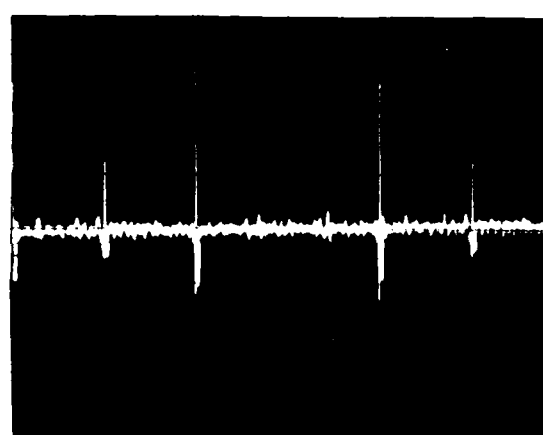
Titanium Disk
(a) Demonstration Probe 1 Data.



Bolt Hole



(b) Demonstration Probe 2 Data.



(c) Demonstration Probe 3 Data.

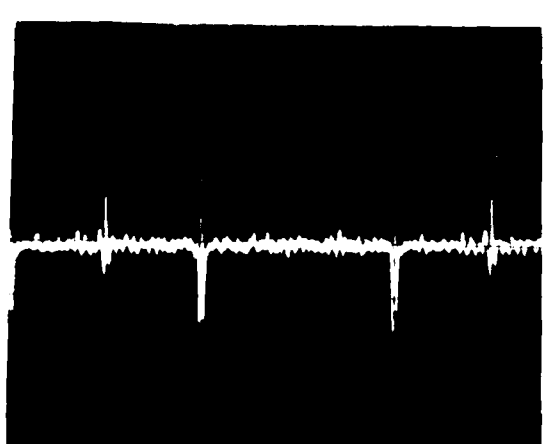
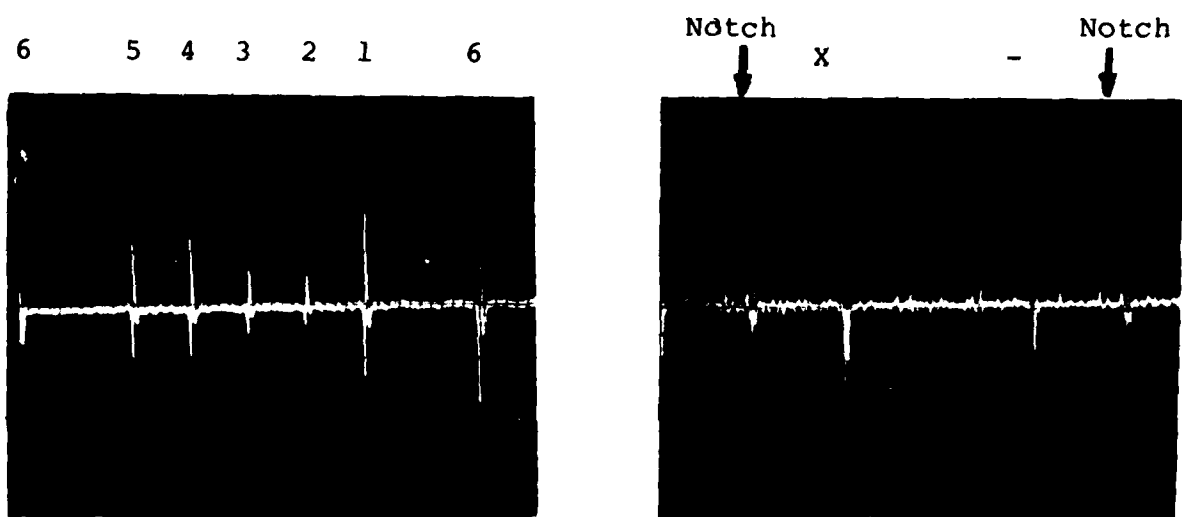
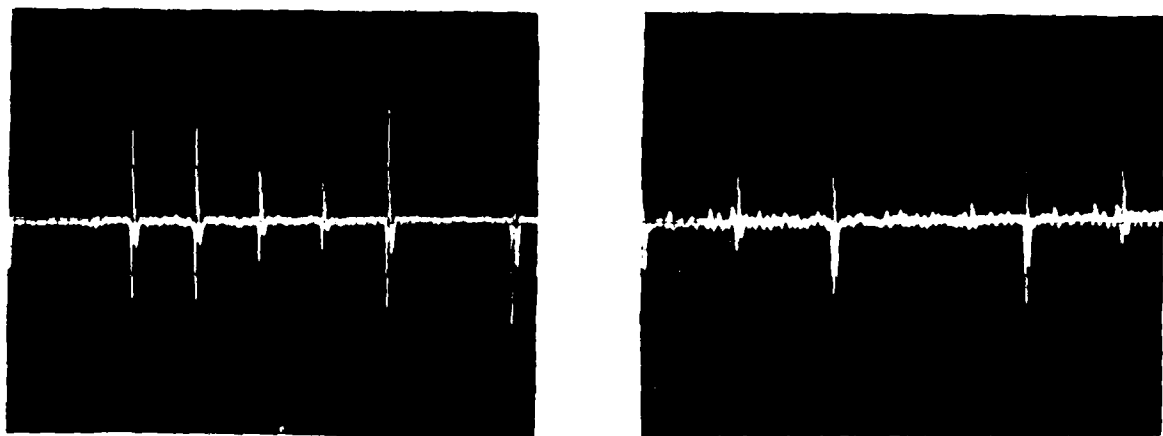


Figure E-1. Demonstration Probe Data on Titanium Disk and Bolt Hole Specimens.



(d) Demonstration Probe 4 Data.



(e) Demonstration Probe 5 Data.

Figure E-1 (cont'd)

APPENDIX F

Electronic Schematics of Processors Used in the Experimental Evaluation

Three of the primary processor circuits are detailed here. The microwave, reflection-coefficient, signal-processor schematic, shown in Figure F-1, details the electronics of the processor used to evaluate the passive YIG probe (refer to Figure 5 in Section 3.0 for block diagram).

The schematic shown in Figure F-2 details the setup and circuitry for implementing the two-coil method of liftoff compensation developed for the passive probe (refer to Figure 10 of Section 3.0 for block diagram).

The active-probe, signal-processor schematic, shown in Figure F-3, details the circuitry used to perform the microwave frequency to voltage conversion and high-pass filtering for the active-probe evaluation (refer to Figure 15 of Section 3.0 for block diagram).

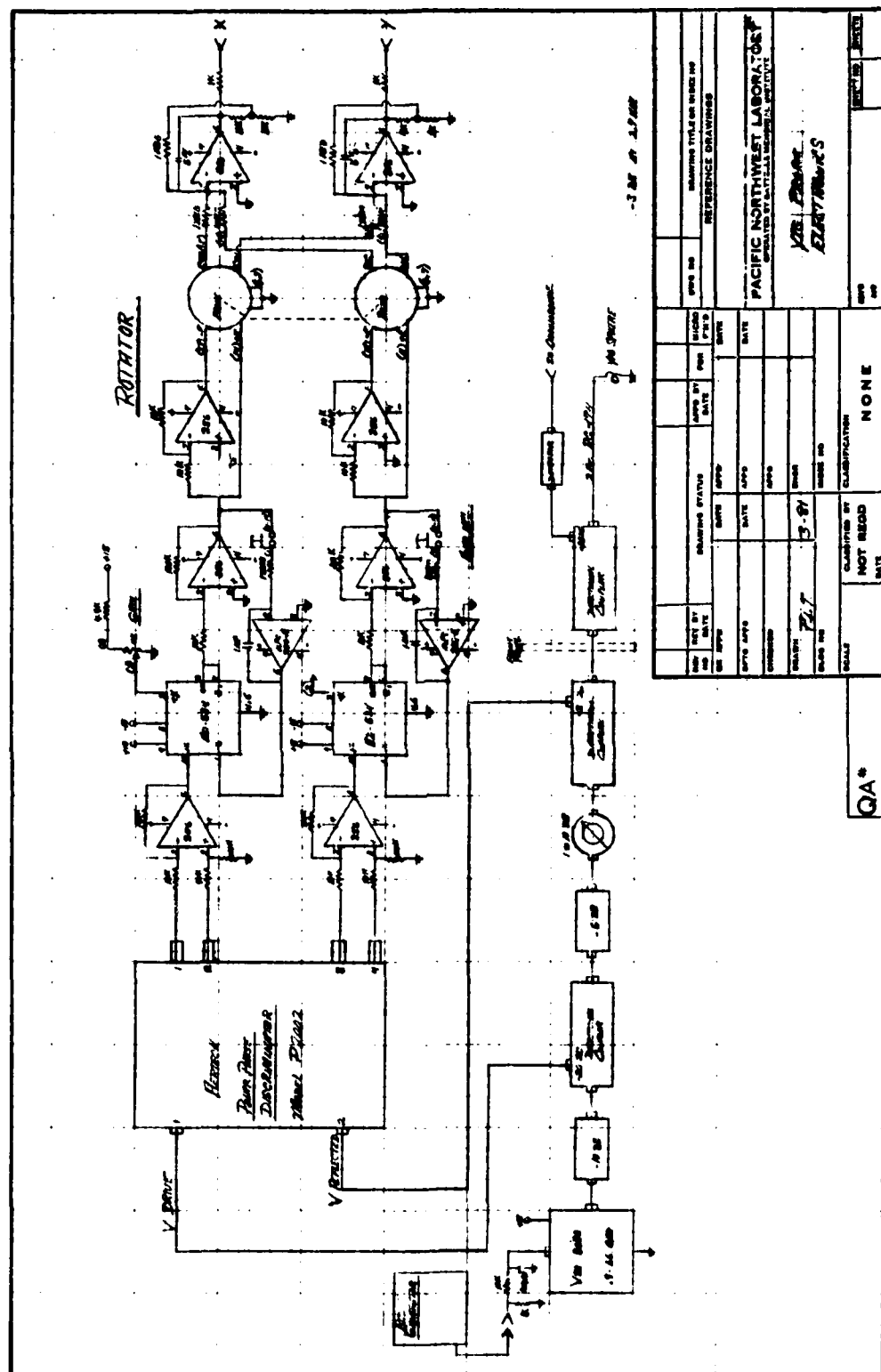


Figure F-1. Microwave Reflection Coefficient Signal Processor Schematic.

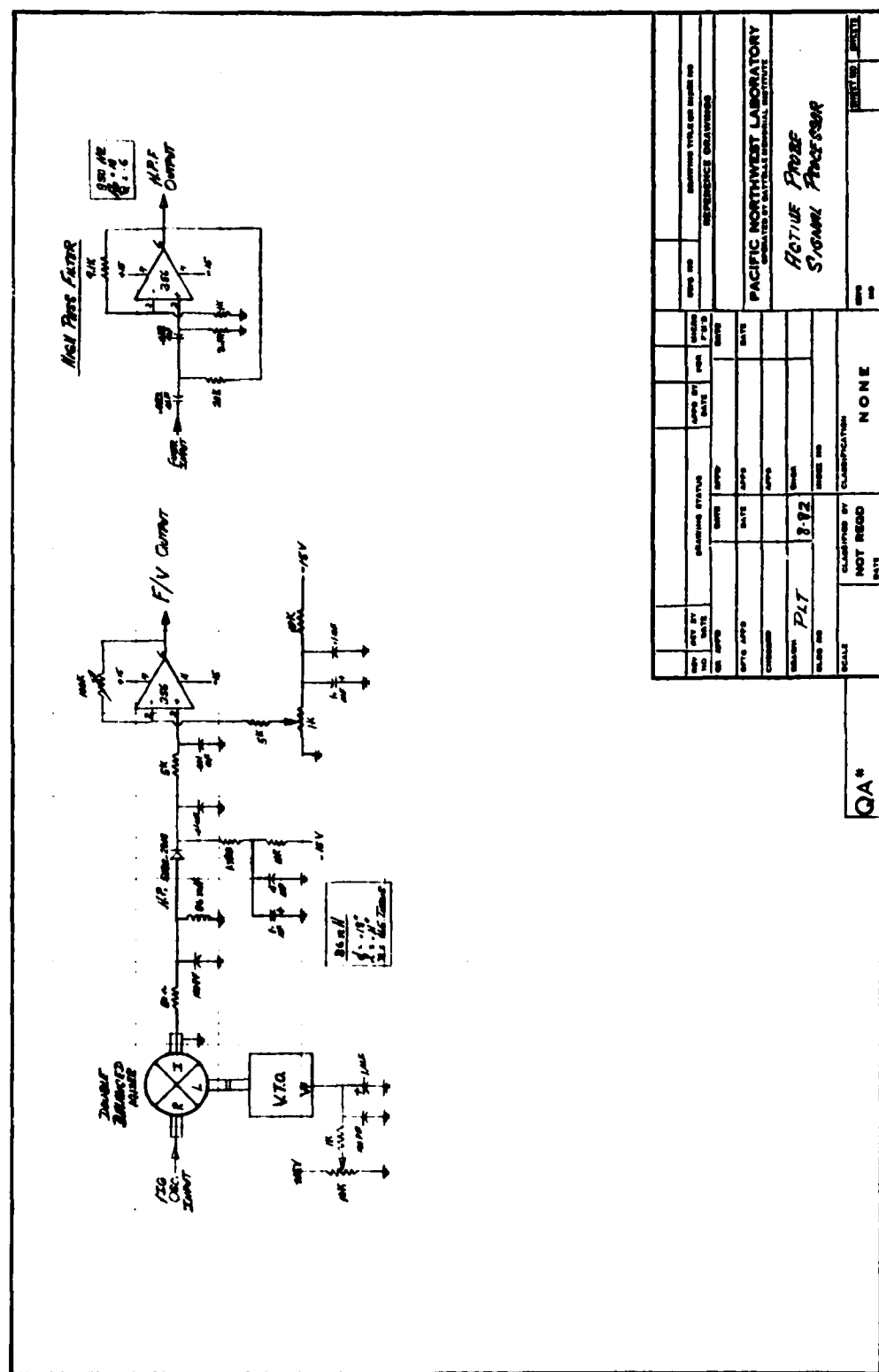


Figure F-3. Microwave Active Probe Signal Processor Schematic.

APPENDIX G

Demonstration Probe Fabrication

The fabrication of a microwave YIG-based active eddy current probe for laboratory evaluation requires basic knowledge in several areas: 1) microwave circuits, 2) YIG probe resonators, and 3) magnetic fields.

The circuit we used for our demonstration active probe is shown in Figure G-1. This circuit is a basic common-base oscillator with a YIG probe utilized as the resonator. The circuit is biased for a transistor collector current of approximately 14 mA with $V_{CE} = 8.3$ V. The rf chokes (RFC) and bypass capacitors are utilized to provide effective rf grounding at their respective points in the circuit. The base inductor (L_B) and the collector matching network (50-ohm stripline and L_M) are adjusted to satisfy, in the desired frequency band, the condition for oscillations to start

$$|\Gamma_R||S_{11}'| > 1,$$

where Γ_R is the YIG probe's reflector coefficient and S_{11}' is the circuit reflection coefficient working into the emitter of the oscillator transistor. If we assume that at resonance $|\Gamma_R| \approx 1$, then all that is necessary to satisfy the condition for oscillation, is for⁽⁹⁾

$$|S_{11}'| > 1.$$

From the equation

$$S_{11}' = S_{11} + \frac{S_{12}S_{22}}{\frac{1}{\Gamma_L} - S_{22}},$$

where Γ_L is the reflection coefficient of the matching network and the S-parameters (S_{11} , S_{12} , S_{21} , and S_{22}) are the common-base scattering parameters

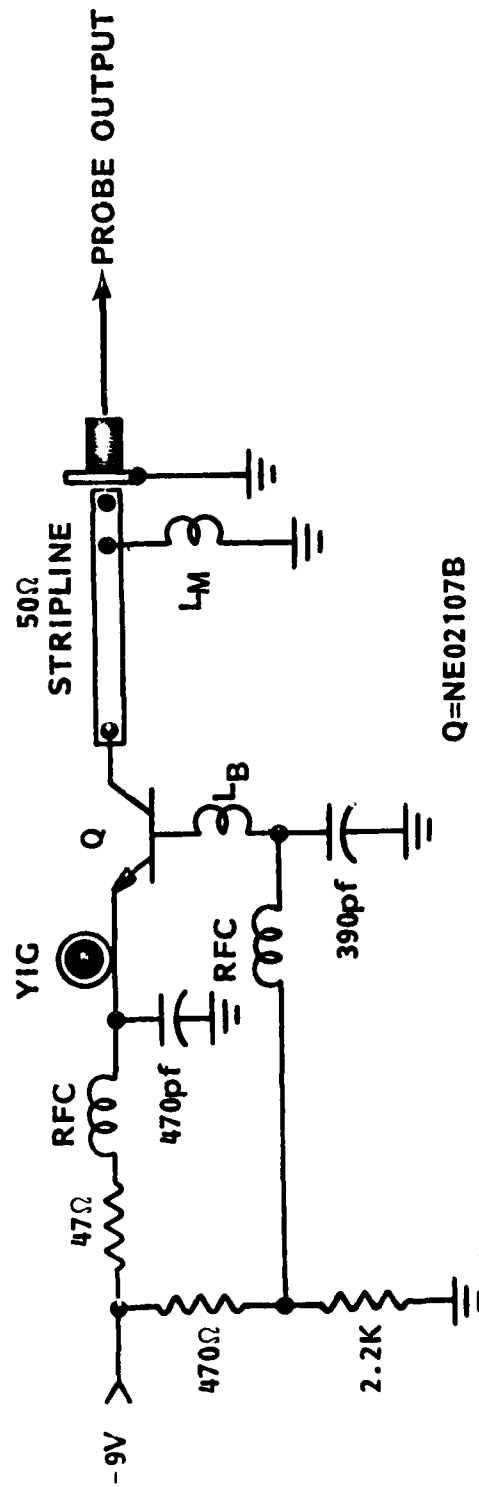


Figure G-1. Demonstration Probe Circuit.

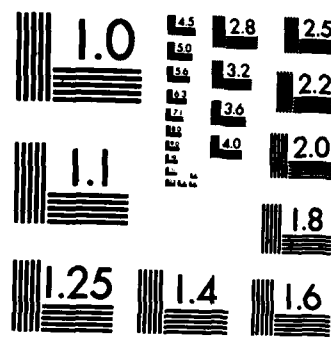
of the transistor with L_B in the base circuit, we see that there are several ways to get $|S_{11}| > 1$. The simplest is to add inductance (L_B) to the base circuit, which will increase S_{11} in the equation to a value greater than one for limited bands of frequencies.⁽¹⁶⁾ To get the widest continuous band of operating frequencies, however, it is necessary to tune both L_B and Γ_L . In the demonstration probe, for best results $L_B = 3.9$ nanohenry (nh) (4.5 mm or 0.180 inch of #36 wire) and $\Gamma_L = 0.78 \angle 77^\circ$ at 870 MHz. The load reflection coefficient Γ_L is set by the inductance of L_M and where it is connected to the 50-ohm stripline as illustrated in Figure G-2. For this probe L_M is connected 18.8 mm (0.175 inch) from the transistor collector and has an inductance of 3.7 nh (5 mm or 0.2 inch of #30 wire). With the YIG probe resonating properly this circuit provides an output of approximately 150 millivolts peak-to-peak at 870 MHz.

The demonstration probe layout is shown in Figure G-3. One of the RFCs can be seen along with the 470 pf chip capacitor. Both RFCs consist of approximately two turns of 1/8 watt carbon-resistor lead on a 2.5 mm (0.1 inch) diameter, which provides 10 nh of inductance. The circuit board itself is single-clad 1.55 mm (0.062 inch) thick glass epoxy with a dielectric constant (ϵ_r) of 3.22. The stripline is approximately 3.58 mm (0.143 inch) wide, 0.075 mm (0.003 inch) thick copper tape, which for this circuit board provides a 50-ohm characteristic impedance.

The YIG sphere can be seen mounted on its adjustment screw and positioned in its 1 mm (0.040 inch) loop of #36 wire. The YIG sphere is a Watkins-Johnson model WJ-5118-02529, which is 0.725 mm (0.029 inch) in diameter and gallium-doped for a saturation magnetization ($4\pi M_s$) of 250 gauss and a typical linewidth of 0.8 oersted. In order to get repeatability of the YIG sphere crystallographic orientation for at least one axis in the probe fabrication, the arrangement shown in Figure G-4 was used. The transparent capsule is placed in the magnetic field between the PMS so that when the YIG sphere is dropped into it, the sphere aligns itself with the field. The sphere is then picked out of the capsule by the glue on the end of the alumina rod. The adjustment screw provides the sphere orientation in the other major axes.

AD-A125 873 RESEARCH TO DEVELOP AND EVALUATE ADVANCED EDDY CURRENT 2/2
SENSORS FOR DETECT. (U) BATTELLE PACIFIC NORTHWEST LABS
RICHLAND WASH J M PRINCE ET AL DEC 82
UNCLASSIFIED AFNL-TR-82-4155 F33615-80-C-5172 F/G 21/5 NL





MICROCOPY RESOLUTION TEST CHART
NATIONAL BUREAU OF STANDARDS-1963-A

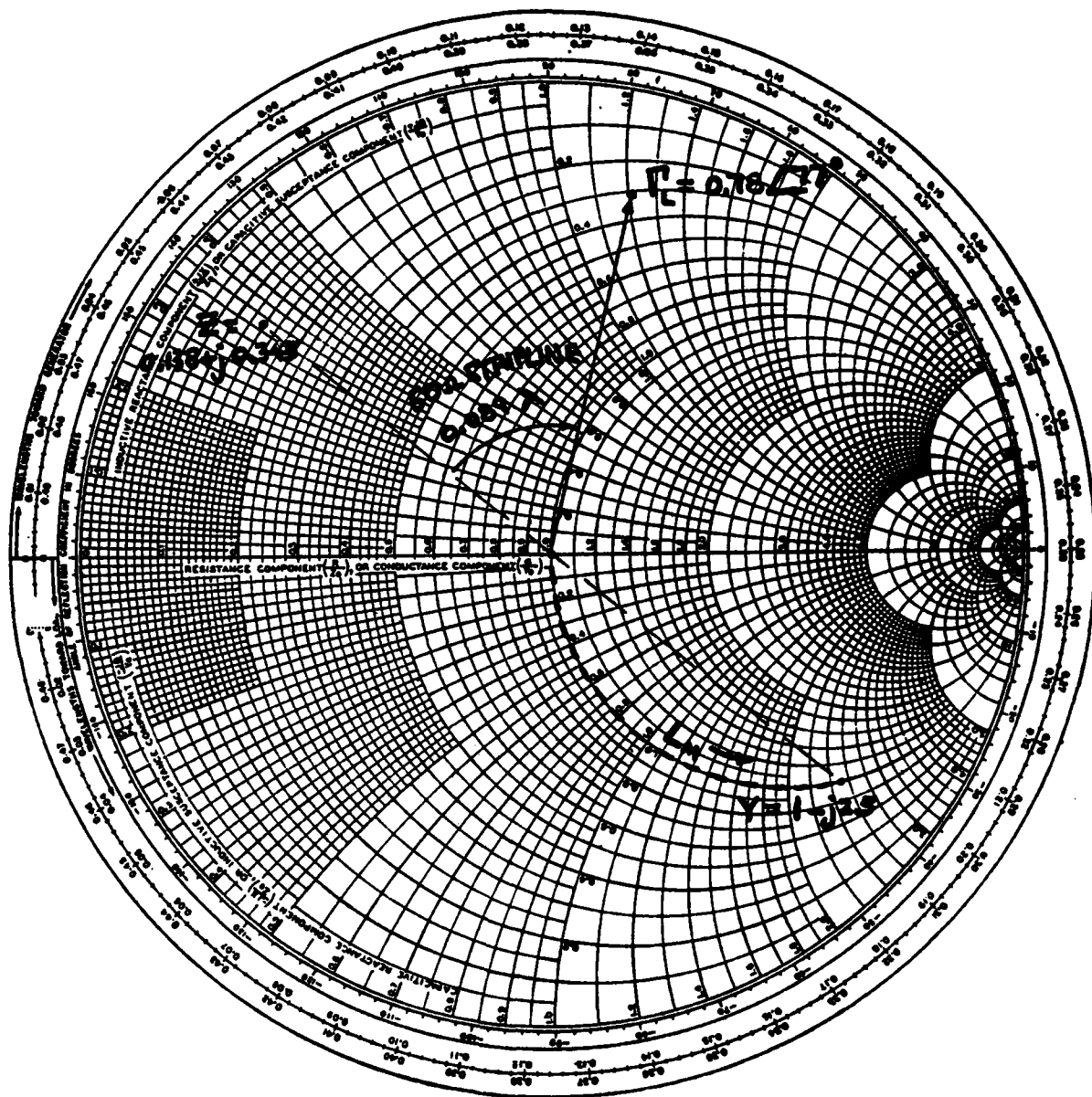


Figure G-2. Demonstration Probe Load Reflection Coefficient, Γ_L .

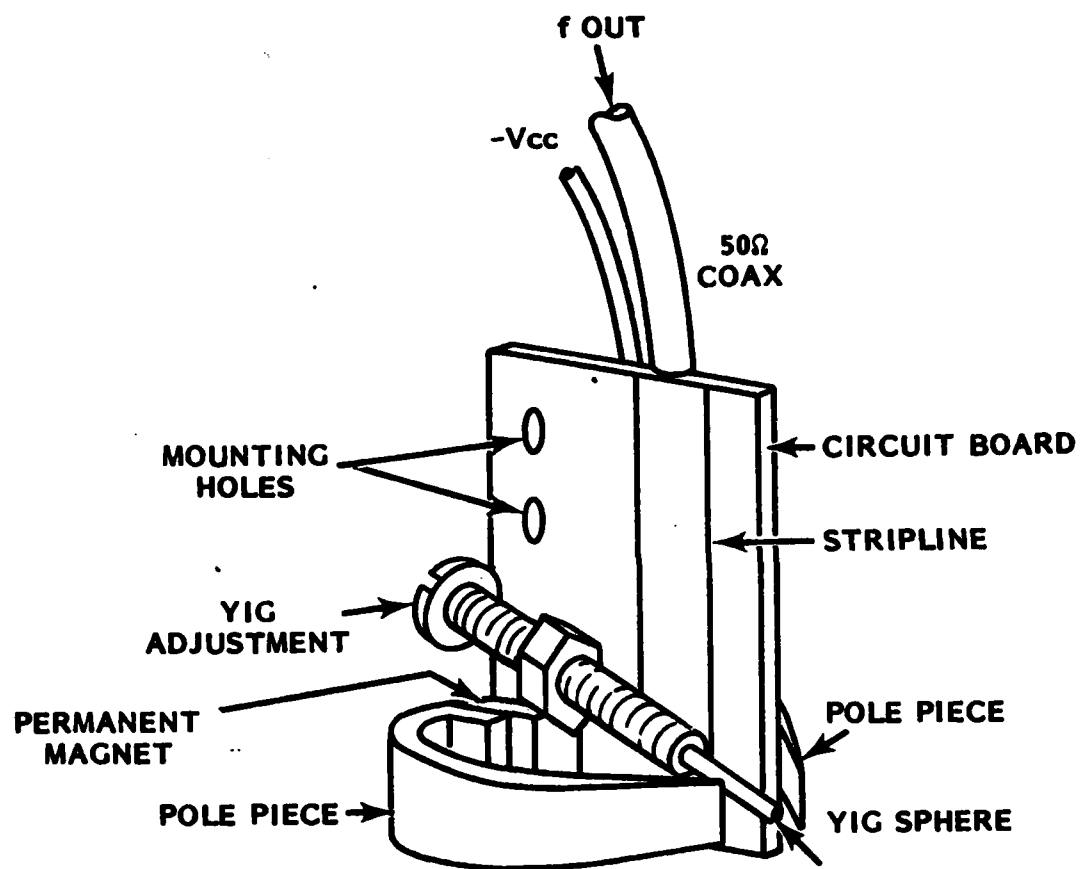


Figure G-3. Demonstration Probe Layout.

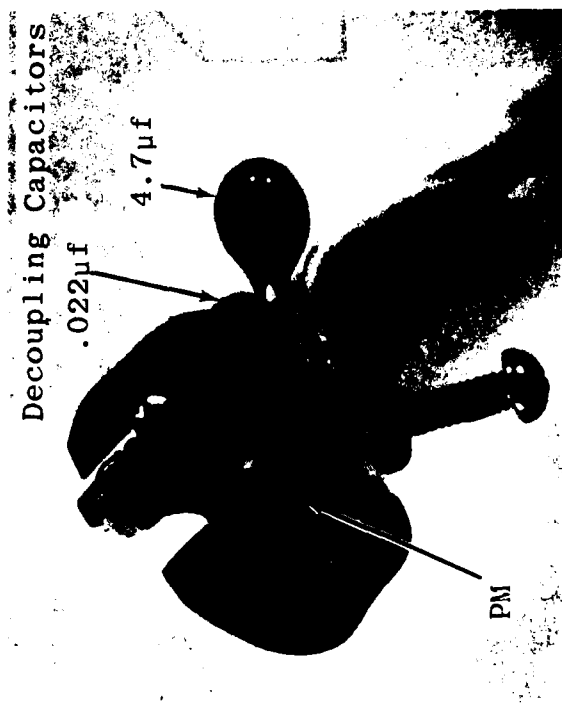
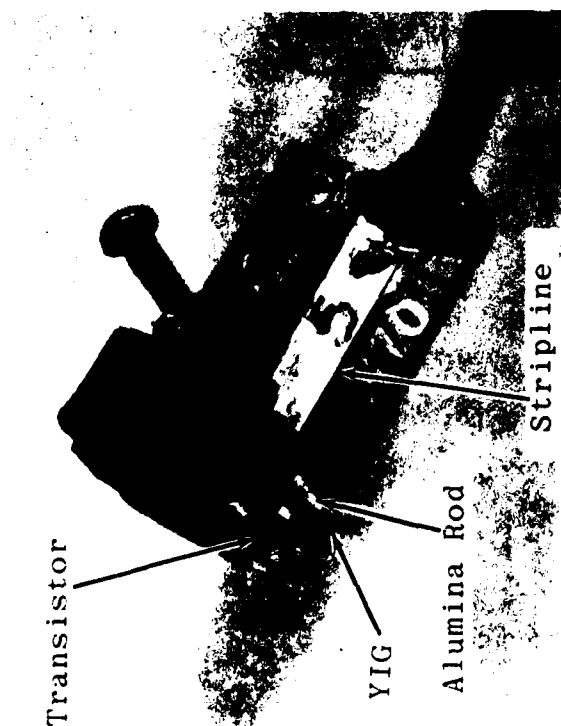
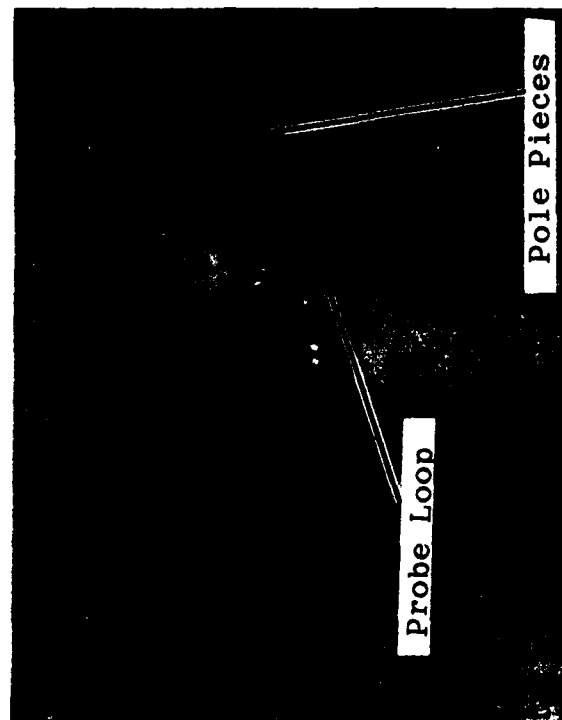


Figure G-3 (cont'd)

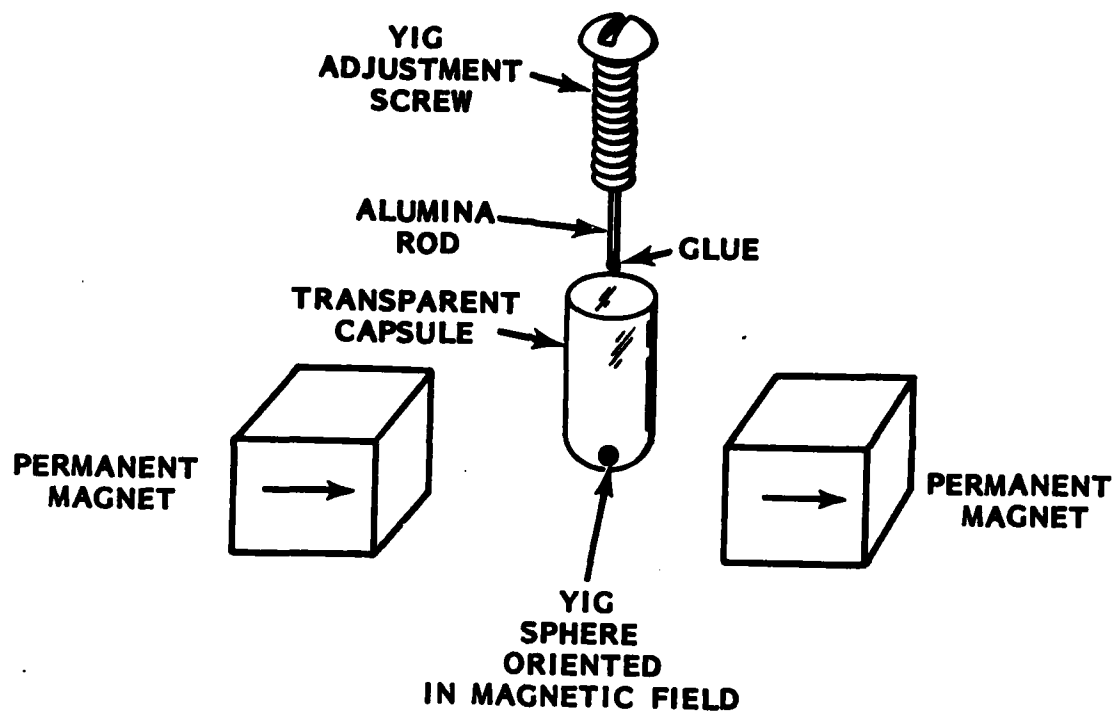


Figure G-4. YIG Sphere Orientation Arrangement.

The magnetic field on the probe is set up by the PM/pole-piece configuration discussed in Section 2.0 on active probes. The PM is a 6 mm (0.24 inch) cube of SmCo 18 material. The pole pieces are 1.56 mm (0.062 inch) thick mild steel with the ends on the PM 6 mm (0.24 inch) wide and the knife-edge ends approximately 4.5 mm (0.18 inch) wide. The knife-edge ends are separated by approximately 7 mm (0.28 inch) to provide the proper magnetic field while allowing clearance for the probe to get into the curved surface of the bolt hole.

The dc power (-9 volt at 17 mA) is brought onto the probe with a single conductor. The shield conductor in the RG-174/U coat provides both the dc and rf returns. The -9 volt line is decoupled on the probe with 4.7 μ F and 0.022 μ F capacitors.

4-
DT